

COMPARISON OF MULTI-PHASE INTERLEAVED BOOST CONVERTERS
WITH VARIOUS COUPLED INDUCTOR TOPOLOGIES

A THESIS SUBMITTED TO
THE GRADUATE SCHOOL OF NATURAL AND APPLIED SCIENCES
OF
MIDDLE EAST TECHNICAL UNIVERSITY

BY

RAŞİT GÖKMEN

IN PARTIAL FULFILLMENT OF THE REQUIREMENTS
FOR
THE DEGREE OF MASTER OF SCIENCE
IN
ELECTRICAL AND ELECTRONICS ENGINEERING

FEBRUARY 2022

Approval of the thesis:

**COMPARISON OF MULTI-PHASE INTERLEAVED BOOST
CONVERTERS WITH VARIOUS COUPLED INDUCTOR TOPOLOGIES**

submitted by **RAŞİT GÖKMEN** in partial fulfillment of the requirements for the degree of **Master of Science in Electrical and Electronics Engineering Department, Middle East Technical University** by,

Prof. Dr. Halil Kalıpçılar
Dean, Graduate School of **Natural and Applied Sciences** _____

Prof. Dr. İlkay Ulusoy
Head of Department, **Electrical and Electronics Engineering** _____

Assist. Prof. Dr. Emine Bostancı Özkan
Supervisor, **Electrical and Electronics Engineering** _____

Examining Committee Members:

Prof. Dr. Işık Çadircı
Electrical and Electronics Engineering, Hacettepe University _____

Assist. Prof. Dr. Emine Bostancı Özkan
Electrical and Electronics Engineering, METU _____

Prof. Dr. Muammer Ermiş
Electrical and Electronics Engineering, METU _____

Assoc. Prof. Dr. Ozan Keysan
Electrical and Electronics Engineering, METU _____

Assist. Prof. Dr. Erhan Demirok
Electrical and Electronics Engineering, Dokuz Eylul University _____

Date: 08.02.2022

I hereby declare that all information in this document has been obtained and presented in accordance with academic rules and ethical conduct. I also declare that, as required by these rules and conduct, I have fully cited and referenced all material and results that are not original to this work.

Name, Surname: Raşit Gökmen

Signature :

ABSTRACT

COMPARISON OF MULTI-PHASE INTERLEAVED BOOST CONVERTERS WITH VARIOUS COUPLED INDUCTOR TOPOLOGIES

Gökmen, Raşit

M.S., Department of Electrical and Electronics Engineering

Supervisor: Assist. Prof. Dr. Emine Bostancı Özkan

February 2022, 157 pages

Multi-phase interleaved boost converters are widely used in high power applications thanks to their high efficiency, high power density, increased output power capability and low input current ripple features. However, increasing the phase number results in an increase in the overall volume of the converter. In order to reduce the volume of the converter, inductors in multi-phase interleaved boost converters can be coupled. For a two-phase interleaved boost converter, loosely-coupled inductor (LCI), close-coupled inductor (CCI) and integrated-winding coupled inductor (IWCI) are the most popular coupled inductor topologies. To clarify the advantages of one coupled inductor topology over the others, 2kW two-phase interleaved boost converters with these coupled inductor topologies are compared under the condition where converters input current ripple and output filter size are kept constant. By this way, changing the inductor type does not have an effect on the rest of converter where the same filter components can be used for all converters with different inductor topologies. For each coupled inductor topology, a systematic design methodology is proposed and all inductors are designed by using these methodologies. A figure of merit (FOM) is developed based

on the total power loss of the converters and inductors total volume and weight to compare overall performances. Designs are experimentally verified and the results show that all topologies with coupled inductors have a better efficiency compared to the converter with discrete inductors and LCI topology is found to have the best FOM among all designs.

Keywords: Multi-phase interleaved boost converter, magnetic coupling, coupled inductor, loosely-coupled inductor (LCI), close-coupled inductor (CCI), integrated winding coupled inductor (IWCI)

ÖZ

ÇEŞİTLİ BAĞLAŞIMLI İNDÜKTÖR TOPOLOJİLERİ İLE ÇOK KATLI DÖNÜŞÜMLÜ YÜKSELTİCİ TİP ÇEVİRİCİLERİN KARŞILAŞTIRILMASI

Gökmen, Raşit

Yüksek Lisans, Elektrik ve Elektronik Mühendisliği Bölümü

Tez Yöneticisi: Dr. Öğr. Üyesi. Emine Bostancı Özkan

Şubat 2022 , 157 sayfa

Çok fazlı dönüşümlü yükseltici tip çeviriciler, yüksek verim, yüksek güç yoğunluğu, artan çıkış gücü kapasitesi ve düşük giriş akım dalgalanması özellikleri sayesinde yüksek güç gerektiren uygulamalarda yaygın bir biçimde kullanılmaktadır. Ancak, faz sayısının artırılması, dönüştürücünün toplam hacminde bir artışa neden olur. Çeviricinin hacmini azaltmak için, çok fazlı dönüşümlü yükseltici tip çeviricilerin fazlarında bulunan indüktörler manyetik olarak bağlaştırılabilir. İki-fazlı bir dönüşümlü boost çevirici için, zayıf bağlaşımlı indüktör, güçlü bağlaşımlı indüktör ve tümleşik sargı bağlaşımlı indüktör topolojileri en popüler bağlaşımlı indüktör topolojileridir. Bu topolojilerin diğerlerine göre avantajlarını açığa kavuşturmak için, giriş akım dalgalanması ve çıkış filtre boyutları tüm topolojiler için aynı olacak koşulda tasarlanan bu topolojiler ile gerçekleştirilmiş 2kW iki-fazlı dönüşümlü yükseltici tip çeviriciler karşılaştırılmıştır. Bu şekilde, indüktör tipi değiştirmenin çeviricinin geri kalanına etkisi olmayacaktır. Farklı indüktör topolojileri ile gerçekleştirilen tüm çeviricilerde aynı filtre elemanları kullanılabilir. Her bir bağlaşımlı indüktör topolojisi için sistematik tasarım metodolojisi önerilmiştir ve tüm indüktörler bu tasarım metodolojisi-

leri kullanılarak tasarlanmıştır. Topolojilerin genel performanslarını kıyaslamak için çevirici güç kayıplarına ve indüktörlerin hacim ve ağırlıklarına dayalı bir değer katsayısı geliştirilmiştir. Tasarımlar deneysel olarak doğrulanmış ve sonuçlar bağlaşımlı indüktör topolojilerine sahip çeviricilerin ayrık indüktörlere sahip çeviriciden daha iyi verime sahip olduklarını ve zayıf bağlaşımlı indüktör topolojisinin tüm indüktör topolojileri arasında en iyi değer katsayısına sahip olduğunu göstermektedir.

Anahtar Kelimeler: Çok fazlı dönüşümlü yükseltici tip çevirici, manyetik bağlaşım, bağlaşımlı indüktör, zayıf bağlaşımlı indüktör, güçlü bağlaşımlı indüktör, tümleşik sargı bağlaşımlı indüktör

To my lovely family...

ACKNOWLEDGMENTS

Firstly, I would like to express my sincere gratitude to Assist. Prof. Dr. Emine Bostancı Özkan for her continuance support, guidance and endless encouragement. I feel really lucky to be one of her graduate students. I am grateful to her for everything I have learned from her and for her attitude to me throughout this study.

I would also like to express my gratitude to my committee members: Prof. Dr. Işık Çadırcı, Prof. Dr. Muammer Ermiş, Assoc. Prof. Dr. Ozan Keysan and Assist. Prof. Dr. Erhan Demirok for their support and suggestions.

I would like to express my heartfelt gratitude to my friend Öztürk Şahin Alemdar for his guidance, support and motivation during not only for this study but also at every aspect of my life.

I would also like to express my gratitude to my colleague Ali Aydın Yamandağ for his motivation and guidance. He always supported me when I felt exhausted and had a problem.

I would like to thank ASELSAN Inc. for its valuable support throughout my graduate studies. Outstanding laboratory and component resources have benefited my work greatly.

I would also like to thank my colleagues Mustafa Tufan Ayhan, Emrah Yüksel, Vedat Yağcı, Yasin Durmaz, Kerim Canlı and Mehmet Akıncı for their enduring support and encouragement.

I would also like to thank my friends from METU PowerLab Yusuf Basri Yılmaz and Hakan Saraç for their enduring support and encouragement.

There is no word can express my gratitude to my family. I am very thankful for their endless support and love during my whole life.

TABLE OF CONTENTS

ABSTRACT	v
ÖZ	vii
ACKNOWLEDGMENTS	x
TABLE OF CONTENTS	xi
LIST OF TABLES	xvi
LIST OF FIGURES	xix
LIST OF ABBREVIATIONS	xxvi
LIST OF VARIABLES	xxvii
CHAPTERS	
1 INTRODUCTION	1
1.1 Motivation and Outline of the Thesis	2
2 MULTI-PHASE INTERLEAVED BOOST CONVERTERS STATE OF ART	5
2.1 Multi-phase Interleaved Boost Converter	5
2.2 Usage Areas of Multi-phase Boost Converters	8
2.3 Selection of Phase Number in Multi-phase Boost Converters	9
2.4 Effect of Input Current Ripple	10
2.5 Coupled Inductor Interleaved Boost Converters	11

2.6	Chapter Summary	15
3	SELECTION OF NUMBER OF PHASES	17
3.1	Discussion on Comparison Conditions	17
3.2	Comparisons under the Same Input Current Ripple Condition	18
3.2.1	Comparision under the 15% Input Current Ripple	18
3.2.2	Comparision under the 5% Input Current Ripple	29
3.3	Comparisons Using the Same Inductance	33
3.4	Chapter Summary	37
4	MATHEMATICAL ANALYSIS OF TWO-PHASE INTERLEAVED BOOST CONVERTERS WITH VARIOUS INDUCTOR TOPOLOGIES	39
4.1	Discrete Inductors (DI)	40
4.1.1	Magnetic Analysis	41
4.1.2	Electrical Analysis of the Interleaved Boost Converter with Discrete Inductors	43
4.2	Loosely-Coupled Inductor (LCI)	44
4.2.1	Magnetic Analysis	45
4.2.2	Electrical Analysis of the Interleaved Boost Converter with LCI	48
4.3	Integrated Winding Coupled Inductor (IWCI)	51
4.3.1	Magnetic Analysis	52
4.3.2	Electrical Analysis of the Interleaved Boost Converter with IWCI	56
4.4	Close-Coupled Inductor (CCI)	57
4.4.1	Magnetic Analysis	58
4.4.2	Electrical Analysis of the Interleaved Boost Converter with CCI	62

4.5	Chapter Summary	64
5	DESIGN OF INDUCTORS	65
5.1	Design Considerations	65
5.2	Discrete Inductors	66
5.2.1	Design Methodology	67
5.2.2	Finite Element Analysis (FEA) Simulations	70
5.3	Loosely-Coupled Inductor	72
5.3.1	Design Methodology	72
5.3.2	Finite Element Analysis (FEA) Simulations	79
5.3.3	Effect of Coupling Coefficient on Inductor Parameters	80
5.4	Integrated Winding Coupled Inductor	84
5.4.1	Design Methodology	84
5.4.2	Finite Element Analysis (FEA) Simulations	90
5.5	Close-Coupled Inductor	92
5.5.1	Boost Inductor	92
5.5.1.1	Design Methodology	92
5.5.1.2	Finite Element Analysis (FEA) Simulations	95
5.5.2	Close-Coupled Inductor	96
5.5.2.1	Design Methodology	96
5.6	Chapter Summary	100
6	CONVERTER IMPLEMENTATION	101
6.1	Measurement Procedure for the Coupled Inductors	101
6.1.1	LCI	101

6.1.2	IWCI	103
6.1.3	CCI	104
6.2	Validation of FEA Results	105
6.2.1	Sensitivity Analysis for DI	108
6.2.2	Sensitivity Analysis for LCI	109
6.2.3	Sensitivity Analysis for IWCI	111
6.2.4	Sensitivity Analysis for BI	113
6.3	Implementation of Inductors	114
6.4	Other Components of the Converter	114
6.5	Power Loss Analysis	115
6.6	Control Loop Design	121
6.6.1	Small-signal Modeling of the Converter	121
6.6.2	Averaged Switch Modelling of the Boost Converter with IWCI	121
6.6.3	Validation of Averaged Model	124
6.6.4	Control Loop Parameters Calculation	124
7	EXPERIMENTAL RESULTS	127
7.1	Test Results of Converters	127
7.2	Transient Test Results	132
7.3	Volume Comparison	136
7.4	Efficiency Comparison	136
7.4.1	Measurement Uncertainty	137
7.5	Discussions	139
8	CONCLUSIONS	143

8.1	Future Work	145
	REFERENCES	147
	APPENDICES	
A	SUPPLEMENTARY DOCUMENTS	153
	A.1 Input Current Ripple Equations	153
	A.2 Controller Design	153

LIST OF TABLES

TABLES

Table 3.1 Converter Parameters	20
Table 3.2 Required Minimum Inductance Values for 15% ΔI_{in} @ 2kW Output Power Level	22
Table 3.3 Inductor Parameters for Different Designs with Various Number of Phase for 15% ΔI_{in} @2kW Output Power Level	23
Table 3.4 Converter Parameters for Different Designs with Various Number of Phases for 15% ΔI_{in} @ 2kW Output Power Level	24
Table 3.5 Performance Comparison of Converters with Different Number of Phases for the Same ΔI_{in} and 2kW Output Power	28
Table 3.6 Required Minimum Inductance Values for 5% ΔI_{in} @ 2kW Output Power Level	30
Table 3.7 Inductor Parameters for Different Designs with Various Number of Phase for 5% ΔI_{in} @2kW Output Power Level	31
Table 3.8 Converter Parameters for Different Designs with Various Number of Phases for 5% ΔI_{in} @ 2kW Output Power Level	31
Table 3.9 Performance Comparison of Converters with Different Number of Phases for the Same 5% ΔI_{in} and 2kW Output Power	33
Table 3.10 Inductor Parameters for Different Designs with Various Number of Phase for the Same ΔI_L @2kW Output Power Level	34

Table 3.11 Converter Parameters for Different Designs with Various Number of Phases for the Same ΔI_L @ 2kW Output Power Level	35
Table 3.12 Performance Comparison of Converters with Different Number of Phases for the Same % ΔI_L and 2kW Output Power	36
Table 4.1 Current Ripple Equations of the Converter with DI in Different Converter Operating Modes	44
Table 4.2 Current Ripple Equations of the Converter with LCI in Different Converter Operating Modes	51
Table 4.3 Current Ripple Equations of the Converter with IWCI in Different Converter Operating Modes	57
Table 4.4 Current Ripple Equations of the Converter with CCI in Different Converter Operating Modes	63
Table 5.1 Converter Parameters	66
Table 6.1 Comparison of Fringing Effect Calculation Methods with FEA and Experimental Results	108
Table 6.2 Sensitivity Analysis of the DI Accuracy Error with Respect to Design Inputs	109
Table 6.3 Comparison of Fringing Effect Calculation Methods with FEA and Experimental Results	110
Table 6.4 Sensitivity Analysis of LCI Accuracy Error with Respect to Design Inputs	110
Table 6.5 Comparison of Fringing Effect Calculation Methods with FEA and Experimental Results	112
Table 6.6 Sensitivity Analysis of the IWCI Accuracy Error with Respect to Design Inputs	112

Table 6.7 Comparison of Fringing Effect Calculation Methods with FEA and Experimental Results	113
Table 6.8 Sensitivity Analysis of the CCI-BI Accuracy Error with Respect to Design Inputs	113
Table 6.9 Inductor Parameters	114
Table 6.10 Other Components of the Converter	115
Table 6.11 Parameters of the Converters with Designed Inductors	115
Table 6.12 Core Loss Results for LCI	118
Table 6.13 Core Loss Results for Inductors	119
Table 6.14 G[s] Matrix, Transfer Functions of State-space Model	123
Table 7.1 Performance Comparison for the Boost Converter Equipped with DI, LCI, IWCI and CCI	139
Table 7.2 Comparison of the Two Different Discrete Inductor Desings	140
Table 7.3 Power Loss Comparison of the Two Different Discrete Inductor Desings	141

LIST OF FIGURES

FIGURES

Figure 2.1	Two-phase boost converter with discrete inductors	5
Figure 2.2	Current waveforms of two-phase interleaved boost converter with discrete inductors	6
Figure 2.3	Electric vehicle drive system [17]	9
Figure 2.4	Two different ways of the coupling between inductor a) direct coupling b) inverse coupling [27]	11
Figure 2.5	Circuit models of the coupled inductor topologies. (a) LCI (b) CCI (c) IWCI [5]	12
Figure 2.6	Current waveforms of two-phase interleaved Boost converter with coupled inductor	13
Figure 2.7	Inductor volume vs. inductor losses of the study of [9]	15
Figure 3.1	Current waveforms of a 4-phase interleaved boost converter with uncoupled inductors	21
Figure 3.2	Required inductance vs duty cycle for input current ripple equals to %15 of maximum input current @2kW output power	22
Figure 3.3	Volume comparison for converters at 150V input voltage, 2kW output power and 15% input current ripple	25
Figure 3.4	Power losses comparisons for converters at 150V input voltage, 2kW output power and 15% input current ripple	29

Figure 3.5	Required inductance vs duty cycle for input current ripple equals to %5 of maximum input current @2kW output power	30
Figure 3.6	Volume comparison for converters at 150V input voltage, 2kW output power and 5% input current ripple	32
Figure 3.7	Power losses comparisons for converters at 150V input voltage, 2kW output power and 5% input current ripple	33
Figure 3.8	Volume comparison for converters at 150V input voltage, 2kW output power and the same inductor current ripple	35
Figure 3.9	Power losses comparisons for converters at 150V input voltage, 2kW output power and 5% input current ripple	36
Figure 4.1	Two-phase interleaved boost converter with various inductor topologies	40
Figure 4.2	Two-phase boost converter with discrete inductors	40
Figure 4.3	Magnetic core structure and magnetic circuit model of a DI	41
Figure 4.4	Waveforms of the magnetic fluxes in the DI core	42
Figure 4.5	Magnetic core structure and magnetic circuit model a LCI	45
Figure 4.6	Waveforms of the magnetic fluxes in the LCI core	48
Figure 4.7	Operating modes of an interleaved two-phase boost converter with LCI	49
Figure 4.8	Two-phase interleaved boost converter with IWCI	52
Figure 4.9	Magnetic core structure and magnetic circuit model of the IWCI	53
Figure 4.10	Waveforms of the magnetic fluxes in the IWCI core	55
Figure 4.11	Two-phase boost converter with CCI	58
Figure 4.12	Magnetic core structure and magnetic circuit model of a CCI	58

Figure 4.13	Magnetic core structure and magnetic circuit model of the CCI-BI	59
Figure 4.14	Waveforms of the magnetic fluxes in the CCI and BI core	62
Figure 5.1	DI design flowchart	67
Figure 5.2	FEA result of the magnitude of the magnetic flux density along the line shown in b) on the center leg of DI	71
Figure 5.3	3D model of DI in FEA and magnitude of magnetic flux density of the core along the cross-section of x-z plane	71
Figure 5.4	Magnetic flux density of the outer leg and center leg of the LCI vs duty cycle for a selected core and coupling coefficient, $\alpha : 0.8$	72
Figure 5.5	LCI design flowchart	73
Figure 5.6	Definitions of the air-gaps	75
Figure 5.7	Coupling coefficient as a function of the extra air-gap distance, $l_{gap,x}$ of LCI	78
Figure 5.8	FEA result of the magnitude of the magnetic flux density along the line shown in b) on the outer leg legs of the LCI	79
Figure 5.9	3D model of the LCI in FEA and magnitude of the magnetic flux density of the core along the cross-section of x-z plane	80
Figure 5.10	Magnetic flux density ratio of the center leg to the outer leg of the LCI vs duty cycle as a function of coupling coefficient, α	81
Figure 5.11	For constant ΔI_{in} , AC magnetic flux density, DC magnetic flux density and number of turns of LCI vs coupling factor, α	82
Figure 5.12	For constant ΔI_{in} , peak magnetic flux density and number of turns of LCI vs coupling factor, α	83
Figure 5.13	Power loss of LCI as a function coupling factor, α	83

Figure 5.14	Magnetic flux density ratio of the center leg to the outer leg of the IWCI vs duty cycle as a function of coupling coefficient, α	84
Figure 5.15	IWCI design flowchart	85
Figure 5.16	Coupling coefficient vs air-gap distance of FEA solution of the IWCI	89
Figure 5.17	FEA result of the magnitude of the magnetic flux density along the line shown in b) on the outer leg legs of the IWCI	91
Figure 5.18	3D model of IWCI in FEA and magnitude of magnetic flux density of the core along the cross-section of x-z plane	91
Figure 5.19	FEA result of the magnitude of the magnetic flux density along the line shown in b) on the center leg legs of the BI	95
Figure 5.20	3D model of CCI-BI in FEA and magnitude of magnetic flux density of the core along the cross-section of x-z plane	96
Figure 5.21	Ratio of peak magnetic flux of the CCI normalized to the peak magnetic flux at $D=0.5$	97
Figure 5.22	CCI design flowchart	97
Figure 5.23	FEA result of the magnitude of magnetic flux density along the center leg of the CCI	100
Figure 6.1	Electrical connections and terminals of the LCI	102
Figure 6.2	Electrical connections and terminals of IWCI	104
Figure 6.3	Electrical connection and terminals of CCI	105
Figure 6.4	Method 1 dimensions definitions	106
Figure 6.5	Method 2 dimensions definitions	107
Figure 6.6	Coupling coefficient vs air-gap length calculated with different methods and FEA simulations	109

Figure 6.7	Coupling coefficient vs air-gap length calculated with different methods	111
Figure 6.8	Implemented inductor prototypes	114
Figure 6.9	Clamped Inductive Switching Energy vs. Drain Current (VDD = 400V) [43]	116
Figure 6.10	Core loss per volume as a function of frequency and magnetic flux density [53]	118
Figure 6.11	Theoretical calculated power losses of converters with various inductor topologies	119
Figure 6.12	Breakdown of power losses of converters with different inductors-1	120
Figure 6.13	Breakdown of power losses of converters with different inductors-2	120
Figure 6.14	DC and small-signal averaged model of a two-phase interleaved boost converter with IWCI	122
Figure 6.15	Steady-state and transient response of switched and averaged IWCI boost converter	124
Figure 6.16	Control block diagram of the circuit	125
Figure 6.17	Bode plots of closed loop two-phase interleaved boost converter with IWCI	125
Figure 7.1	Two-phase interleaved boost converter board	127
Figure 7.2	Experimental Setup	128
Figure 7.3	Output voltage start-up of the converter with IWCI	129

Figure 7.4	Critical waveforms through the module at critical load and minimum input voltage (D=0.625): CH1 (orange) = $I_{LP_{h1}}$, CH2 (blue) = V_{gs} of PH1 Mosfet, CH3 (purple) = V_{DS} of PH1 mosfet, CH4 (green) = V_{DS} of PH2 mosfet	130
Figure 7.5	Current waveforms of the converter for minimum input voltage and full load operating point (D=0.625) : CH1 (orange) = I_{in} , CH2 (blue) = $I_{LP_{h1}}$, CH3 (purple) = $I_{LP_{h2}}$	131
Figure 7.6	Output voltage ripple at minimum input voltage and full load, CH4 (green) = V_{out} (AC Coupled)	132
Figure 7.7	Load transient of the converter with LCI, CH1 (orange) = I_{in} , CH2 (blue) = $I_{LP_{h1}}$, CH3 (purple) = $I_{LP_{h2}}$, CH4 (green) = V_{out}	133
Figure 7.8	Timings of control algorithm, CH1 (orange) = ADC EOC, CH2 (blue) = V_{GS} of Ph1 mosfet, CH3 (purple) = End of calculations in the ISR.	134
Figure 7.9	Load current step from 50% to 100%, CH1 (orange) = I_{in} , CH2 (blue) = $I_{LP_{h1}}$, CH3 (purple) = $I_{LP_{h2}}$, CH4 (green) = V_{out}	134
Figure 7.10	Load current step from 100% to 50%, CH1 (orange) = I_{in} , CH2 (blue) = $I_{LP_{h1}}$, CH3 (purple) = $I_{LP_{h2}}$, CH4 (green) = V_{out}	135
Figure 7.11	Load current step from 100% to 20%, CH1 (orange) = I_{in} , CH2 (blue) = $I_{LP_{h1}}$, CH3 (purple) = $I_{LP_{h2}}$, CH4 (green) = V_{out}	135
Figure 7.12	Volume measurement of IWCI	136
Figure 7.13	Efficiency results for $V_{in} = 150V$	138
Figure 7.14	Efficiency results for $V_{in} = 200V$	138
Figure 7.15	Efficiency results for $V_{in} = 250V$	139

Figure A.1 (a) Single-phase boost converter switch network. (b) Switch network waveforms. (c) Equivalent dc and ac small-signal averaged switch network model. [54] 154

LIST OF ABBREVIATIONS

2D	Two-Dimensional
3D	Three-Dimensional
AC	Alternating Current
ADC	Analog to Digital Converter
BEV	Battery Electric Vehicle
CCI	Close-Coupled Inductor
CCI-BI	Boost Inductor of the Close-Coupled Inductor
DC	Direct Current
DCM	Discontinuous Conduction Mode
DI	Discrete Inductor
DSP	Digital Signal Processor
EOC	End of Conversion
ESR	Equivalent Series Resistance
FCHEV	Fuel-cell Hybrid Electric Vehicle
FEA	Finite Element Analysis
FOM	Figure of Merit
IWCI	Integrated Winding Coupled Inductor
KVL	Kirchhoff's Voltage Law
LCI	Loosely-Coupled Inductor
MLT	Mean Length Turn
MOSFET	Metal Oxide Semiconductor Field Effect Transistor
PHEV	Plug-in Hybrid Electric Vehicle
PWM	Pulse Width Modulation
RMS	Root Mean Square

LIST OF VARIABLES

A_e	Effective cross-sectional area of a magnetic core
A_L	Inductance Factor item[ϕ] Magnetic flux
B	Magnetic flux density
λ	Magnetic flux linkage
B_{peak}	Peak magnetic flux density
V_{in}	Input voltage
V_o	Output voltage
I_{in}	Input current
D	Duty cycle
f_{sw}	Switching frequency
T_s	Switching period
$I_{ph,av}$	Average phase current
$I_{ph,rms}$	RMS phase current
$I_{ph,pp}$	Peak to peak ripple of phase current
I_L	Inductor current
L	Self inductance
M	Mutual inductance
α	Coupling coefficient
\mathcal{R}_{mo}	Reluctance of the outer leg of the core
\mathcal{R}_{mc}	Reluctance of the center leg of the core
μ_0	Permeability of free space
l_{gap}	Air gap length
$A_{winding}$	Winding area of the core

V_e	Effective volume of the core
k_{cu}	Fill factor
A_{wire}	Wire area
J	Current density
V_{DS}	Drain-to-source voltage
V_{GS}	Gate-to-source voltage
$R_{ds_{on}}$	On state resistance
E_{on}	Turn-on switching energy
E_{off}	Turn-off switching energy
E_{oss}	Stored energy on output capacitance
$P_{switching}$	Switching loss
$P_{conduction}$	Conduction loss
P_{drive}	Gate drive loss
Q_{gate}	Gate charge
$P_{loss,supply}$	Gate drive supply loss
P_{diode}	Diode loss
$V_{forward}$	Forward voltage drop of diode
E_c	Stored energy on the junction capacitance of diode
P_{core}	Core loss of inductor
$P_{winding,DC}$	DC winding loss of inductor
$P_{winding,AC}$	AC winding loss of inductor
$R_{winding,dc}$	DC winding resistance of the inductor
$R_{winding,ac}$	AC winding resistance of the inductor

CHAPTER 1

INTRODUCTION

Multi-phase boost converters are widely used in several applications that demand increase in the voltage level and higher power level. The most common applications can be listed as power factor correction circuits, photo-voltaic applications and electric vehicle applications. In battery electric vehicles, DC-DC converters can be optionally implemented between the source and the traction inverter to be able to control the DC-link voltage. A controlled DC-link voltage ensures that the performance of the traction system does not get affected from the voltage changes of the source and it gives the flexibility of controlling the DC-link voltage to increase system efficiency [1]. On the other hand, a step-up DC-DC converter is generally required for fuel cell hybrid electric vehicle (FCHEV) power-trains to solve the voltage mismatch between the voltage of the fuel cell and the battery storage system [2]. Moreover, power converters employed in the power train should be light-weight, highly-efficient, small-sized and have low input current ripple. Input current ripple of step-up DC-DC converter may reduce the lifetime of fuel cell stack [3], [4].

Multi-phase interleaved boost converters are known to be good candidates in applications where high efficiency, high power density, increased output power capability, and low input current ripple features are important. Instead of traditional discrete inductor (DI) solution, coupled inductors can be employed in these converters to achieve low loss, low volume and light weight passive component solutions [5]. In case of a two-phase interleaved converter or converters with even phase numbers, loosely-coupled inductor (LCI) proposed in [6], closely-coupled inductor (CCI) proposed in [7] and integrated-winding coupled inductor (IWCI) topologies as proposed in [8] can be employed. Several studies are conducted in order to evaluate the advan-

tages of boost converters with these coupled inductor topologies. In [5, 8], detailed magnetic and electrical analysis of IWCI are provided, where the topologies are compared by considering the same inductor current ripple and the same peak magnetic core flux density for all designs. Input current ripples of converter are not considered. In [9], designs with IWCI, LCI and DI are compared under two different conditions. Firstly, turn numbers in all designs are kept the same and volume of the heatsink, semiconductor ratings, output capacitor and inductors are compared. Secondly, inductors are designed to achieve minimum inductor losses. In this case, other components in the converters are redesigned. In these studies, the design methodologies start from the core selection. Moreover, fringing effects were not mentioned or considered in these studies. As authors states that fringing effects are very effective in inductors large air-gap such as coupled inductors and affect the inductor design parameters. Therefore, designing a coupled inductor by ignoring the fringing effect may result in unexpected results.

1.1 Motivation and Outline of the Thesis

In this study, two-phase interleaved boost converters with LCI, CCI and IWCI topologies are designed to operate under the same converter operating conditions and their performance characteristics are compared. Unlike the studies in the literature where comparisons are carried by keeping the inductor's current ripple the same which does not include all components volume in the converter, in order to compare the volumes of the converters by considering effects of inductors only, the design condition was chosen as constant input current ripple and constant output voltage ripple. By this way, volume of the rest of the converters kept constant. By this way, the same circuit components are employed in the boost converter power stage to test the topologies. Thanks to this approach, overall of performances of the converters that are their efficiencies and size of inductors are compared. A discrete inductor solution is also designed and experimentally tested by using the same converter board. Design procedure of coupled inductors is another topic that is not studied in the literature.

The outline of this thesis can be summarized as follows:

- **Chapter 2:** This chapter explains multi-phase interleaved boost converter operation briefly. It includes a literature review of multi-phase interleaved boost converters and coupled inductors. In the literature review following subjects will be discussed: advantages, disadvantages and usage areas of multi-phase boost converters, selection of number of phase in multi-phase boost converters, introduction of coupled inductor topologies in two-phase interleaved boost converter and their advantages and disadvantages.
- **Chapter 3:** This chapter presents a comparative study between multi-phase boost converters to find the optimum value of the number of phases. The comparison condition will be discussed.
- **Chapter 4:** This chapter presents mathematical analysis of coupled and discrete inductor topologies. It includes electrical analysis in order to obtain current ripple equations and magnetic analysis in order to obtain magnetic flux equations.
- **Chapter 5:** This chapter presents novel design methodologies for each coupled inductor and discrete inductor topologies. The simulation and validation of proposed designs using finite element analysis are presented. The effect of coupling coefficient on the inductor parameter is investigated for the loosely-coupled inductor.
- **Chapter 6:** In this chapter, measurement procedure for each coupled inductor topology is proposed. The effect of fringing fluxes on the air-gap reluctances is calculated analytically by using the proposed formulas in the literature. These analytical solutions are compared with the results found in finite element analysis simulations and measurements. Parameters of implemented inductors and selected other components of the converter are presented in this chapter. Moreover, a methodology to obtain a small-signal, averaged model of the two-interleaved boost converter with integrated winding coupled inductor (IWCI) is presented. The validation of this methodology is done by comparing simulation results. After that, designed control loop parameters and other converter components are presented in this chapter.
- **Chapter 7:** This chapter presents experimental results of a 2kW, two-phase

interleaved boost converter having 150-250Vdc input and 400Vdc output voltage equipped with different coupled inductor topologies and discrete inductor topologies. The validation of designed inductors is presented. Moreover, a comparison of performances of inductor topologies is presented.

- **Chapter 8:** This chapter is the conclusion chapter and some possible future works are suggested in this chapter.

CHAPTER 2

MULTI-PHASE INTERLEAVED BOOST CONVERTERS STATE OF ART

2.1 Multi-phase Interleaved Boost Converter

The circuit schematic of two-phase interleaved boost converter with discrete inductors is shown in Fig. 2.1.

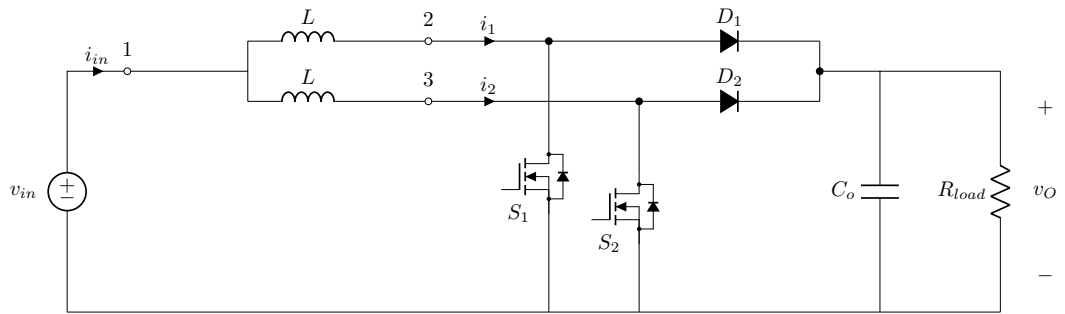


Figure 2.1: Two-phase boost converter with discrete inductors

The switches of the two-phase interleaved boost converter are controlled by 180° phase-shifted PWM signals. According to the switching states, there are four different operating modes in a two-phase interleaved boost converter. These can be classified as mode1 ($S_1 : ON, S_2 : OFF$), mode2 ($S_1 : OFF, S_2 : ON$), mode3 ($S_1 : OFF, S_2 : OFF$) and mode4 ($S_1 : ON, S_2 : ON$). When, switches are conducting their inductors are charged through the input voltage. When switches are turned off the stored energy on the inductors and input voltage source feeds the output capacitor and load. With the help of interleaved operation, the frequency of input current ripple and output voltage ripple equals two times the switching frequency. This allows the

use of smaller filter elements without increasing the switching frequency. The input and inductors current waveforms of a two-phase interleaved boost converter are given in Fig. 2.2.

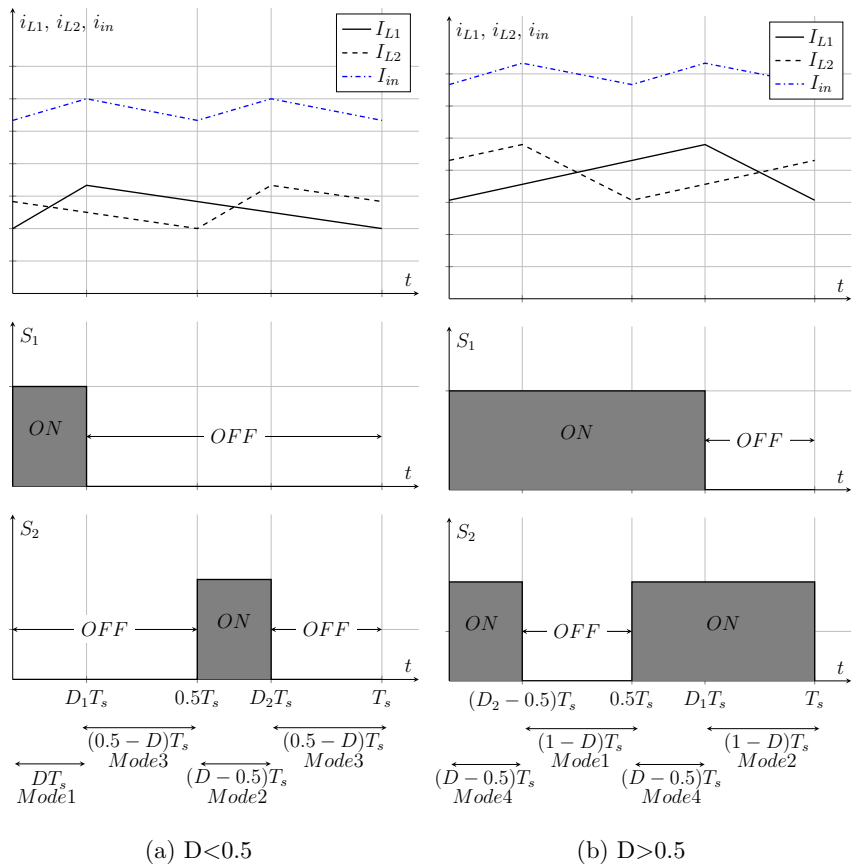


Figure 2.2: Current waveforms of two-phase interleaved boost converter with discrete inductors

Well-known advantages of multi-phase converters can be listed as:

- Increased output power capacity of the converter:** By increasing the number of phases, as the load current is shared between phases the output capacity of the converter can be increased by using the same cooling and semiconductors with the same ratings [10].

- **Increased efficiency thanks to the current sharing between phases:** As the current per phase decreases, the conduction losses on power semiconductors and inductors reduce. Losses at higher power levels are dominated by conduction losses. Therefore, increasing the number of phases helps significantly to improve the efficiency at high power levels [11].
- **Higher frequency of input current ripple and output voltage ripple than the switching frequency:** By interleaving operation and application of phase-shifted PWM signals, the frequency of the current and voltage ripples seen on the converter input and output is increased with the number of phases times the switching frequency. This comes with the advantage of using smaller filter components without increasing the switching frequency of the converter which increases power losses [12].
- **Lower input current ripple:** As the number of phases increases, the magnitude of the input current ripple reduces with the same inductor employed in phases. Input current ripple is an important parameter, especially in the fuel cell electric vehicle applications, as it affects the lifetime of the fuel cell stack [13, 14].
- **Improved transient response y the use of smaller filter components:** The main limiting factor in improving transient responses is the poles brought by large filter components. As mentioned before, multi-phase converters have ripple characteristics with lower magnitude and higher frequency that can be filtered by using smaller filter components. As a result, using smaller filter components gives the opportunity of increasing the bandwidth of the control loop of the converter. Another advantage of multi-phase converters for load transient is that they can overlap all phases during load demand or turn off all phases during load release to quickly charge or discharge the output capacitor [15].

However, besides these advantages, multi-phase converters also have some disadvantages. These disadvantages can be listed as:

- **Increased size and volume of the converter:** Multi-phase converters have

more inductors which is the most dominant component in converter's size and volume. This makes them have a higher size and volume than the single-phase converters. Coupling the discrete inductors of the multi-phase converter can be a good solution for this drawback [16].

- **Complex control technique needed for multi-phase converters:** Unequal sharing of the load current between phases may result in thermal unbalance between the components of the converter, thus their control is more complex.
- **Increased cost:** Increased phase number requires more semiconductors, gate drive circuits, more sensors for control circuits, etc. These will increase cost of converter.

Therefore, it can not be always advantageous to increase the number of phases. Selection of phase number for a multi-phase converter is an important design question.

2.2 Usage Areas of Multi-phase Boost Converters

The main usage area of a multi-phase boost converter is power-train of electric vehicles. Fig. 2.3 shows the power-train on an electric vehicle where energy sources can be fuel-cells, batteries and super-capacitors [17]. The voltage rating of these energy sources can be different. Therefore, as an interface between the energy sources and DC-link of the powertrain one or more DC-DC converters are generally used. The output voltage of the battery/fuel-cell and super-capacitors are stepped up and regulated by these DC-DC converters. A conventional boost converter is the most popular candidate in BEV, PHEV powertrain due to its simple and low-cost power stages and ease of control of the converter [18]. In electric vehicle applications, this DC-DC converter should be capable of a high power rating. However, for high power applications boost converter might not be used because of its low current handling capability and thermal management issues [19]. To overcome these problems multi-phase and multi-switch boost converters are used [20]. Other usage areas of multi-phase interleaved boost converters are power factor correction (PFC) [21] and photo-voltaic applications [22].

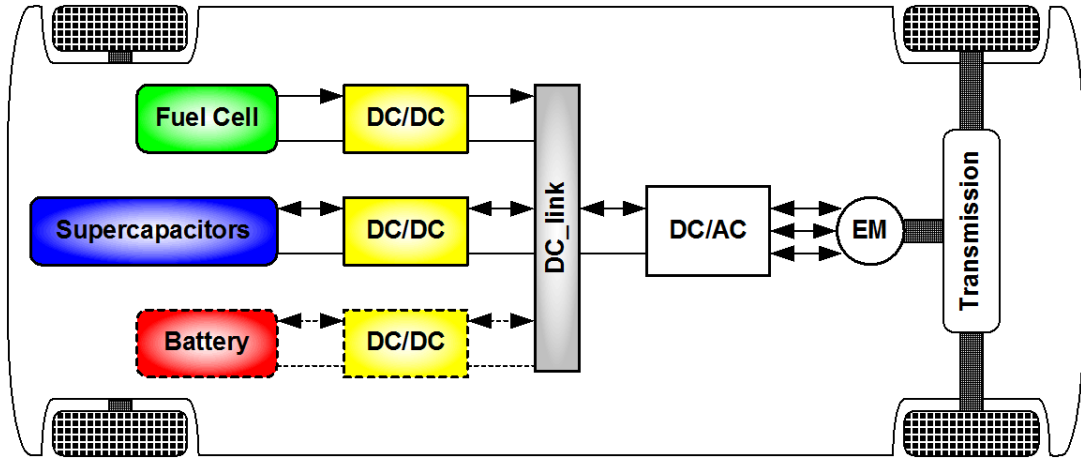


Figure 2.3: Electric vehicle drive system [17]

2.3 Selection of Phase Number in Multi-phase Boost Converters

The selection of the number of phases in multi-phase interleaved converters plays an important role. As stated above, an increase in the phase number comes with some advantages but at the same, it has some drawbacks. Therefore, the effect of the phase number on converter performance should be considered. In [23], the impact of number of phases of an interleaved boost converter is investigated. The number of phases changes from 1 to 6 in that study. Two different design conditions are considered. Firstly, the authors consider that all phases have the same inductance. But for this operating condition, as the number of phases increases, converters with a higher number of phases enter the DCM operating mode due to the lower phase currents. Thus, as a second design condition, phase inductances are adjusted so that the inductor current ripple level is kept constant for all designs. After that inductor volume index is calculated as a function of inductance and inductor current. The results show that for the first condition 2-phase has the minimum inductor volume index and for the second condition inductor volume index decreases with increasing phase number. The proposed inductor volume index is a good approach however, some practical limits are not considered. For example, the fact that an increased number of turns for a higher phases number may result in a design that has a fill factor exceeding production limits. Also, the availability of commercial cores is limited. In other words, the small difference in inductances of 5-phase design and 6-phase design may result in

the same magnetic core for both designs. Therefore, inductor volume for the 6-phase may become higher than expected. Moreover, input current ripple values are different for all designs, where a 6-phase design will have a smaller input current ripple and hence a smaller input filter size. When comparing volumes of all designs, input and output filter size should be considered. Also, for power loss analysis inductor power losses including conduction and core losses should be included. In [24], the effect of the number of phases is investigated by only considering the efficiencies of the converters.

In this study, the same inductance values are used for all phases as mentioned before this results in a constant increase in the volume of the converter as the number of phases increases. Moreover, volume comparisons are not included. In the following chapter of this thesis, the impact of number of phases in interleaved boost converter is investigated by considering these mentioned drawbacks.

2.4 Effect of Input Current Ripple

Input current ripple of a converter is an important parameter in several applications. Several studies are investigating the effect of input current ripple on fuel cells. In [14], it is mentioned that high-frequency current ripple harmonics are filtered by a double-layer capacitor of the fuel cell stack. However, the authors emphasize that the maximum RMS current value that can be tolerated by the double-layer capacitor and the effect of current ripple on the lifetime of the fuel cell stack should be considered. The negative effects of the fuel cell output current ripple's on fuel cell lifetime and efficiency are addressed in several papers. In [25], it is mentioned that it is important to keep the ripple value of the fuel cell output current low to avoid undesired hysteresis energy losses inside the fuel cell stack. Besides fuel-cell applications, in PFC applications input current ripple affects electromagnetic interference noise of the system. Lower input current ripple results in smaller input differential mode filters [26].

2.5 Coupled Inductor Interleaved Boost Converters

Magnetic coupling of inductors can be done in two different ways. One is direct coupling and the other one is inverse coupling. Fig. 2.4 shows two different coupling types of circuit schematics. The inverse coupling has smaller current ripples and slower transient response whereas direct coupling has larger current ripples and faster transient responses [27]. Moreover, if the inductors are inversely coupled, the DC flux created by the windings is canceled out which makes the inverse coupling a better choice in high current applications.

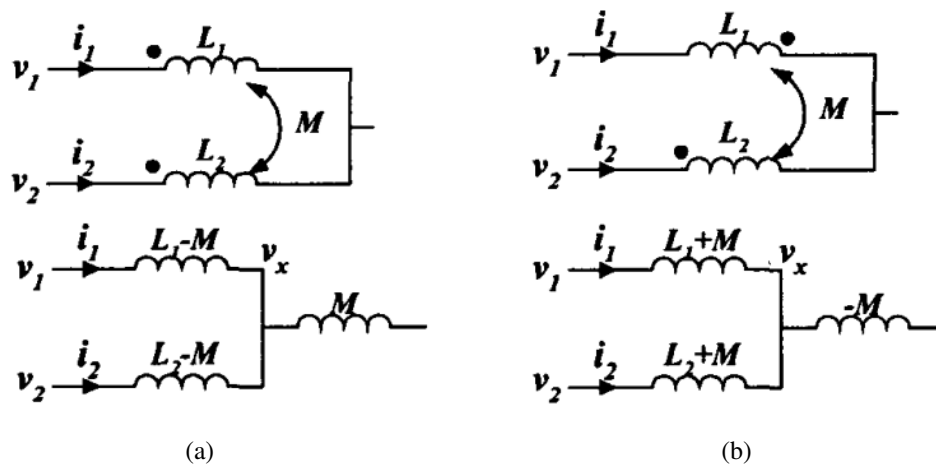


Figure 2.4: Two different ways of the coupling between inductor a) direct coupling b) inverse coupling [27]

Magnetic integration techniques or coupling inductors in interleaved multi-phase converters are widely used in the literature [28, 29, 30, 31]. The main advantages of the coupled inductors can be listed as [32]:

- DC flux generated by the DC current flowing through the inductor can be canceled by the help of inverse magnetic coupling. This results in lower magnetic flux density in the magnetic core and hence smaller magnetic core can be used compared with discrete inductors.
- AC flux can be shared between the windings, which results in lower peak to peak magnetic flux density.

- The inductor current ripple is affected by another phase current due to the magnetic coupling. In a one switching period inductor current sees different inductances and hence ripple magnitude is lower than the traditional discrete inductors and frequency is higher than the conventional discrete inductors.

In the case of a two-phase interleaved boost converter, there are different types of coupled inductor topologies. Loosely-coupled inductor (LCI) proposed in [6], closely-coupled inductor (CCI) proposed in [7] and integrated-winding coupled inductor (IWCI) topology proposed in [8] can be employed. The circuit schematics of these coupled inductor topologies are shown in Fig. 2.5.

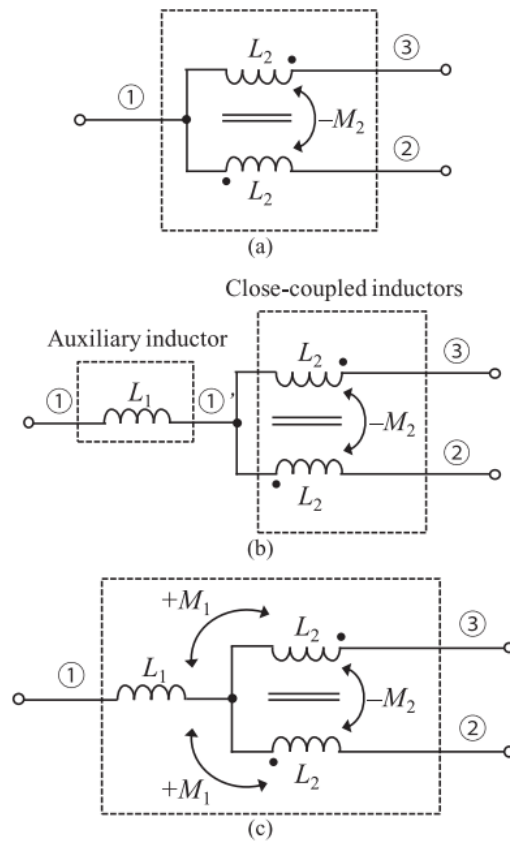


Figure 2.5: Circuit models of the coupled inductor topologies. (a) LCI (b) CCI (c) IWCI [5]

A two-phase interleaved boost converter shown in Fig. 2.1 can be configured with an inversely coupled inductor instead of discrete inductors. The current waveforms and operating modes of a converter with an inversely coupled inductor are given in

Fig. 2.6. As can be seen, the current of phases is affected by the other phases switching state. The inductance seen by the inductor current is different at these operating modes.

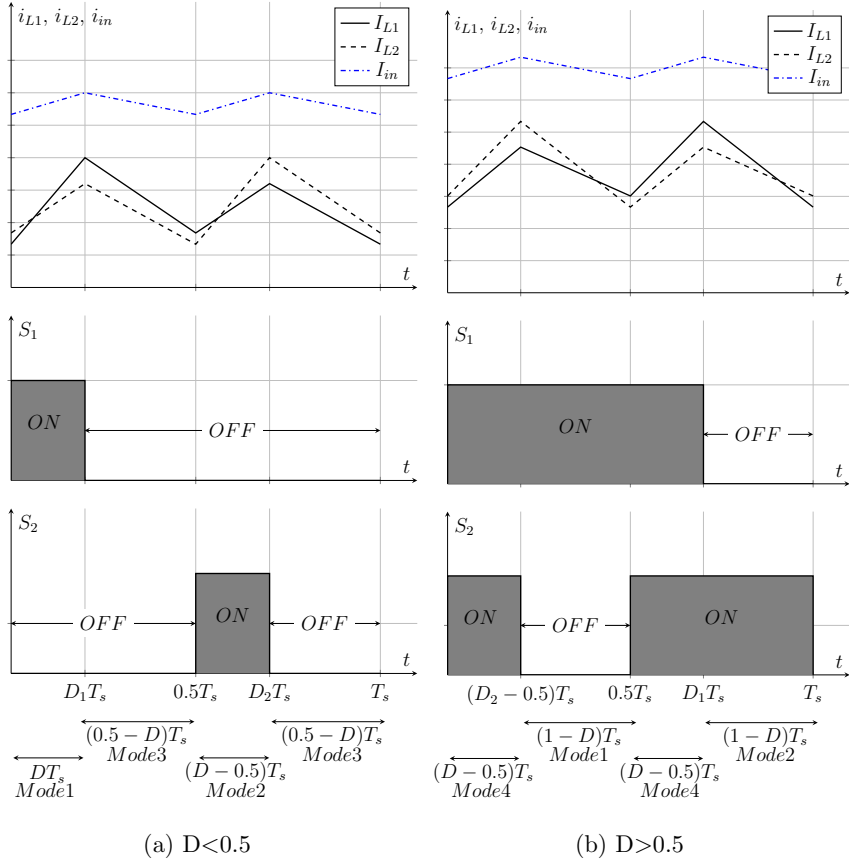


Figure 2.6: Current waveforms of two-phase interleaved Boost converter with coupled inductor

The first topology named LCI is known as an integrated inductor and transformer [33]. In this method, most of the time EE or EI cores are used. Two windings connected to converter phases are wound on the outer legs of the core. There exist a large air gap on the center leg of the core; therefore, fringing flux is relatively high. By adjusting the length of the air gap, mutual inductance between the windings can be controlled. In this topology, leakage inductance limits the input current ripple

whereas inductor current ripple is limited by the sum of self and mutual inductances. Closely-coupled inductor design consists of one boost (auxiliary) inductor connected in series with the input source and one inversely coupled transformer which is connected to phases of a interleaved converter. The advantages of the CCI topology are the flexibility to use different cores for two inductors and easy implementation due to simple design procedures [5, 34]. Thanks to the high coupling coefficient and inverse coupled windings, a core with low saturation can be used for CCI, while a higher saturation core can be selected for the boost inductor where high DC current flows through. A new topology constructed by integrating boost inductor with the transformer of CCI is called as IWCI. This topology has 3 windings where the winding wound on the center leg of EE core is connected to the input source while the other windings are connected to converter phases. Center winding is directly coupled to the other windings while outer windings are inversely coupled among themselves. The main advantage when compared to CCI method is downsizing of the magnetic component size by integrating the boost inductor and the transformer [8].

Several studies are conducted in order to evaluate the advantages of boost converters with these coupled inductor topologies. In [5, 8], detailed magnetic and electrical analyses of IWCI are provided, where the topologies are compared by considering the same inductor current ripple and the same peak magnetic core flux density for all designs. In this design condition, the volume of the LCI is found 10% smaller than the other coupled inductor topologies. LCI also has the best efficiency among the other inductors. This study is conducted by neglecting the fringing effect presented in the air gap. The author states that it is important to consider the fringing effect especially, in high power applications because this effect can produce considerable losses and can affect characteristics of inductors. Moreover, input current ripples of converters are not considered. In [9], designs with IWCI, LCI and DI are compared under two different conditions. Firstly, turn numbers in all designs are kept the same and volume of the heatsink, semiconductor ratings, output capacitor and inductors are compared. For this condition, IWCI and LCI have less volume than the other designs. IWCI is found to have the highest power losses while LCI has the lowest power losses. Fig. 2.7 shows the results under this condition. Secondly, inductors are designed to achieve minimum inductor losses. In this case, the volume results are

not changed. For this condition, other components in the converters are redesigned. Similarly, the fringing effect is not considered.

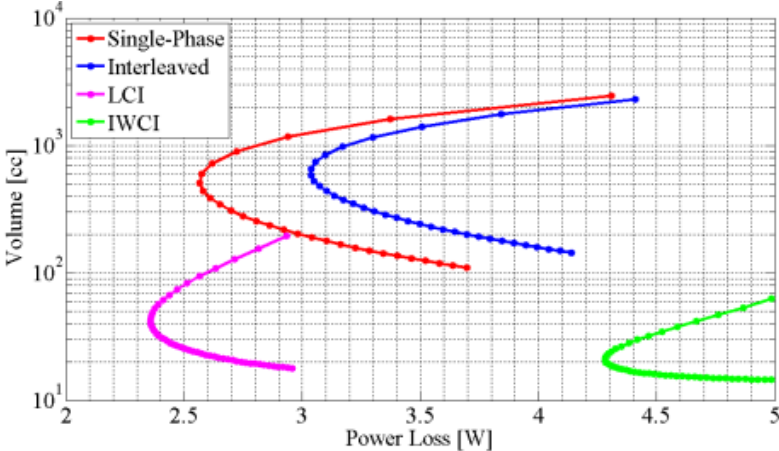


Figure 2.7: Inductor volume vs. inductor losses of the study of [9]

2.6 Chapter Summary

In this chapter, the operation of a two-phase interleaved boost converter with discrete inductors is briefly explained by presenting current and switching waveforms of the converter. The advantages, disadvantages and usage areas of multi-phase boost converters are presented. The studies covering the impact of the number of phases on interleaved converters in the literature are discussed. Since, input current ripple is considered as a design input in this thesis, several studies in the literature considering the effect of input current ripple of the multi-phase converter are reviewed. Magnetic coupling types are introduced and the reason why inverse coupling is widely used in high power interleaved boost converters is explained.

The operation of a two-phase coupled inductor interleaved boost converter is briefly explained. Well-known coupled inductor topologies in the literature for a two-phase interleaved boost converter are presented. Several studies about a comparison of these coupled inductor topologies in the literature are reviewed. The design conditions are investigated and possible contributions to the literature are discussed.

CHAPTER 3

SELECTION OF NUMBER OF PHASES

In this section, the effect of the number of phases on the efficiency and volume of multi-phase boost converters is investigated. Only the converters with discrete (uncoupled) inductors are considered due to the easy analytical calculations. However, the results are expected to be similar for coupled inductor topologies.

4 different multi-phase boost converters with number of phases of 1, 2, 4 and 6 are designed for 2kW output power level. Numerical calculations for inductances for different number of phases are conducted under the same design condition that they have the same input current ripple or the same inductor current ripple. After the calculation of inductances, discrete inductors are designed for all converters. Finally, designed converters are compared by considering their volume and efficiency.

3.1 Discussion on Comparison Conditions

The comparison of converters with the different number of phases should be done under the same condition. The different comparison conditions are possible. The first condition is that all converters have the same inductance for their phases. In this way, all converters have the same inductor current ripple. However, the input current ripple will be different. When it comes to efficiency, after some power level where the effect of fixed losses of the converter such as gate drive loss, switching loss, etc. are become less dominant, efficiency tends to increase as the number of phases increases. This is a result of less current per phase for the higher number of phases, which gives less conduction losses which is the most dominant part of power losses at higher power levels. The other comparison condition is that all converters

with the different number of phases can be designed to have the same converter input current ripple. As stated in Chapter 2, input current ripple of a boost converter can be an important parameter for some applications such as a fuel-cell stack. For this condition, all converters can be used with the same input filter. Also, as the number of phases increases phase inductance value reduces for the same input current ripple. Thus, this condition is fairer regarding volume comparison. In the rest of this chapter, the first comparisons are carried out for 2kW converters at 15% and 5% constant input current ripple condition. Then, 2kW multi-phase converters that have the same phase inductance regardless of the phase number are compared.

3.2 Comparisons under the Same Input Current Ripple Condition

Converters are designed for two different input current ripple conditions. Firstly, the input current ripple selected is as 15%. For this current ripple value, converters with 4-phase and 6-phase have large inductor current ripple where the currents go to negative which is allowed in synchronous operation of the boost converter. Therefore, converters with 4-phase and 6-phase have higher power losses due to the increased RMS current value when compared to converters with 1-phase and 2-phase. Therefore, 4-phase and 6-phase designs are excluded for this condition. The other current ripple condition is selected as 5%. For this input current ripple value, converters with 6-phase do not enter to DCM or inductor current does not go negative. It is expected that for this ripple condition the power loss differences between converters with 1-phase and 2-phase and converters with 4-phase and 6-phase will be reduced.

3.2.1 Comparison under the 15% Input Current Ripple

First of all, inductance values that result in the same input current ripple for each design are calculated. Then, inductors are designed by selecting their magnetic cores. Other circuit components of the boost converter are selected for each design. Electrical analysis of single-phase, 2-phase, 4-phase and 6-phase interleaved boost converters can be done according to the different switching states. The input current ripple can be calculated for each operating point, separately. For a single-phase boost

converter, the input current and inductor current are the same. Ripple value of input current of single-phase boost converter can be written as in Eq. 3.1. For a 2-phase interleaved boost converter there are 4 different operating modes. These can be classified as mode1 ($S_1 : ON, S_2 : OFF$), mode2 ($S_1 : OFF, S_2 : ON$), mode3 ($S_1 : OFF, S_2 : OFF$) and mode4 ($S_1 : ON, S_2 : ON$). Switching and current ripple waveforms and operating modes of 2-phase interleaved boost converter are shown in Fig. 2.2. For $D < 0.5$ input current ripple can be calculated in mode1. During mode1, phase1's inductor is charged through the input voltage while phase2's inductor is discharging through the output capacitor. The current ripple equations for this mode can be written as in Eq. 3.1 and Eq. 3.2.

$$\Delta I_{in,1phase} = \Delta I_{L,1phase} = \frac{V_{in}DT_s}{L} \quad (3.1)$$

$$\begin{aligned} \Delta I_{L1,2phase} &= \frac{V_{in}DT_s}{L} \\ \Delta I_{L2,2phase} &= \frac{(V_{in} - V_o)DT_s}{L} \\ \Delta I_{in,2phase} &= \frac{V_o(1 - 2D)DT_s}{L} \end{aligned} \quad (3.2)$$

Similarly, for $D > 0.5$ the input current ripple can be written during mode4. As given in below.

$$\begin{aligned} \Delta I_{L1,2phase} = \Delta I_{L2,2phase} &= \frac{V_{in}(D - 0.5)T_s}{L} \\ \Delta I_{in,2phase} &= \frac{2V_o(1 - D)(D - 0.5)T_s}{L} \end{aligned} \quad (3.3)$$

The converter with 4-phase has 4 different input current ripple equations as a function of the duty cycle. Switching and current ripple waveforms and operating modes of a 4-phase interleaved boost converter are shown in Fig. 3.1. Input current ripple equations for 4-phase interleaved boost converter are given in Eq. 3.4. Input current

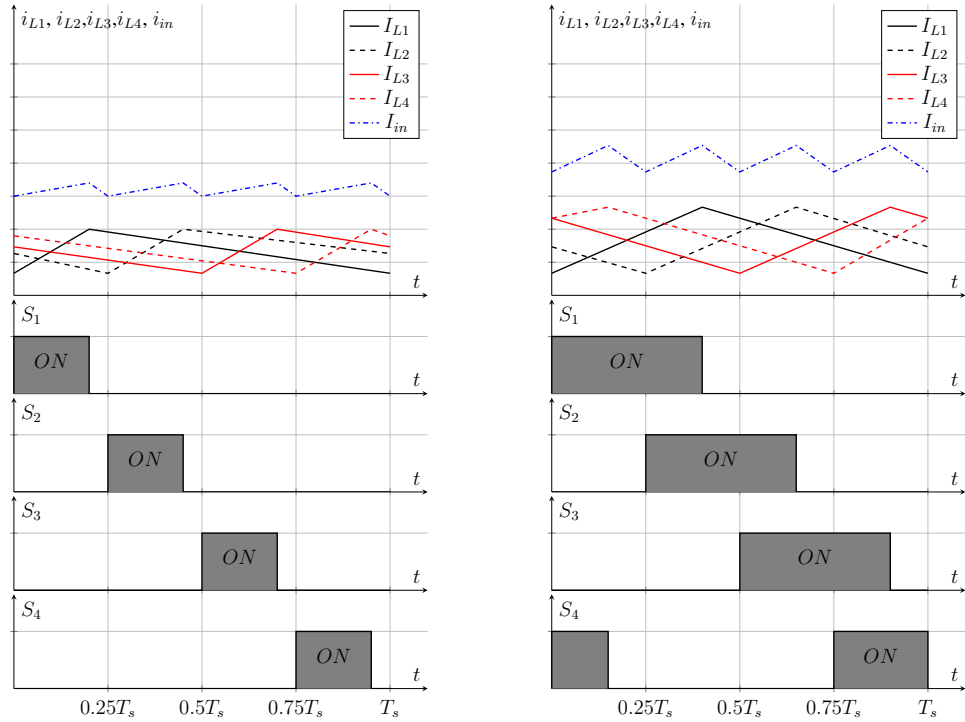
ripple equation of a 6-phase interleaved boost converter is given in Appendix A.1.

$$\Delta I_{in,4phase} = \begin{cases} \frac{V_o(1-4D)DT_s}{L}; & 0 \leq D \leq 0.25 \\ \frac{V_o(2-4D)(D-0.25)T_s}{L}; & 0.25 \leq D \leq 0.5 \\ \frac{V_o(3-4D)(D-0.5)T_s}{L}; & 0.5 \leq D \leq 0.75 \\ \frac{4V_o(D-0.75)(1-D)T_s}{L}; & 0.75 \leq D \leq 1 \end{cases} \quad (3.4)$$

Design parameters of the converter are summarized in Table 3.1. Required minimum inductance values as a function of the duty cycle for 2kW output power level is given in Fig. 3.2. For operating region $0.375 \leq D \leq 0.625$, the minimum required inductance values to satisfy desired maximum input current ripple are given in Table 3.2. For 4-phase and 6-phase converters, small phase inductance results in large inductor current ripple. Therefore, their inductor currents become negative or enter DCM. Also, high-frequency power losses and core loss of the inductors are significantly higher than the converters with 1-phase and 2-phase. In conclusion, for 15% input current ripple condition, designs with 4-phase and 6-phase are not considered.

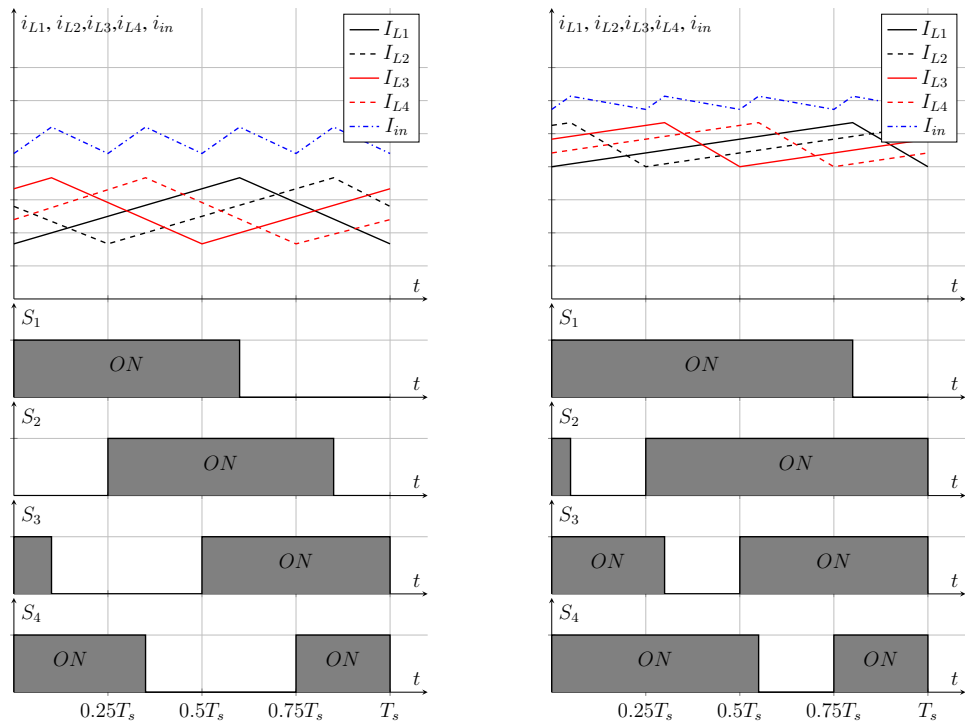
Table 3.1: Converter Parameters

	Input Voltage	Output Voltage	Output Power	Switching Frequency	Input Current Ripple
Value	150V-250V	400V	2kW	50kHz	15%



(a) $D < 0.25$

(b) $0.25 < D < 0.5$



(c) $0.5 < D < 0.75$

(d) $0.75 < D < 1$

Figure 3.1: Current waveforms of a 4-phase interleaved boost converter with uncoupled inductors

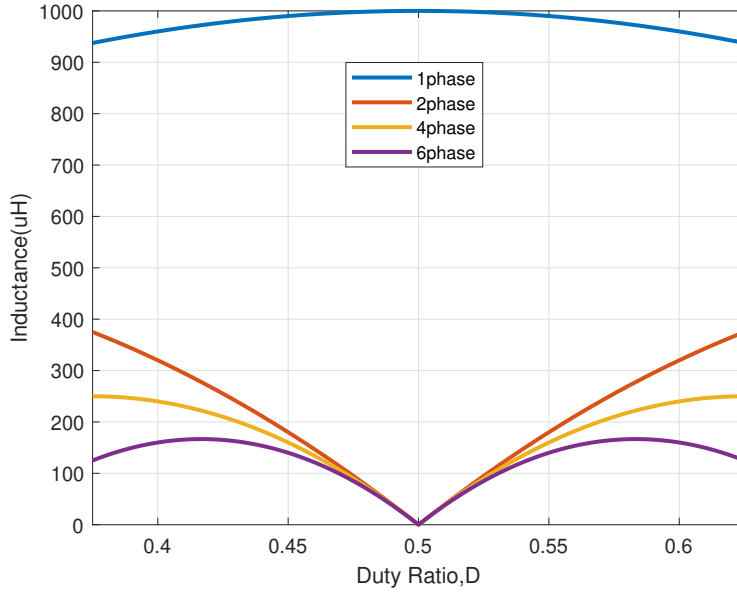


Figure 3.2: Required inductance vs duty cycle for input current ripple equals to %15 of maximum input current @2kW output power

Table 3.2: Required Minimum Inductance Values for 15% ΔI_{in} @ 2kW Output Power Level

	1-Phase	2-Phase	4-phase	6-Phase
Inductance(μH)	1000	375	250	166.6

For each converter, required energies in $mH.A^2$ which is given in Eq. 3.5 are calculated. Then, the cores with Kool Mu material from Magnetics Inc. are searched. Magnetic cores having stored energy parameters greater than the calculated one are considered. Starting from the core with minimum size among the considered cores, the number of turns is calculated according to the inductance factor specified in the cores datasheet, A_L and inductance value. Then, by using the calculated number of turns and limiting B_{peak} to $0.3T$, minimum cross-section area, A_e is calculated by using Eq. 3.7. If the core meets that minimum cross-section area, it is selected otherwise the same design procedure is applied to the consecutive cores. Designed inductors parameters for all designs are given in Tab. 3.3.

$$Energy = \frac{1}{2} L I_{phx,peak}^2 \quad (3.5)$$

$$N = \sqrt{\frac{L}{A_L}} \quad (3.6)$$

$$B_{peak} = \frac{LI_{ph_x,av}}{NA_e} + \frac{0.5V_{in}DT_s}{NA_e} \quad (3.7)$$

In these equations, $I_{ph_x,peak}$ is the peak phase current, N number of turns, V_{in} input voltage of converters, T_s switching period, A_L inductance factor, A_e cross-section area of a magnetic core, μ_0 magnetic permeability of the free-space.

Table 3.3: Inductor Parameters for Different Designs with Various Number of Phase for 15% ΔI_{in} @2kW Output Power Level

	1-Phase	2-Phase
Inductance	1000 μH	375 μH
B_{dc}	0.32T	0.21T
ΔB_{pp}	0.04T	0.16T
B_{peak}	0.34T	0.29T
Number of Turns	71	34
$R_{winding,dc}$	56m Ω	35m Ω
Cross Section Area, A_e	600mm ²	350mm ²
Core Type	00K8024E026	00K5528E090
number of parallel layer, p	6	3
$\sigma = R_{winding,ac}/R_{winding,dc}$	17.23	4.95

The converter parameters such as RMS current and average current of phases are calculated to select the other components such as semiconductors and output capacitors. The average, $I_{ph_x,av}$, peak to peak ripple, $I_{ph_x,pp}$, and RMS value, $I_{ph_x,rms}$ of each phase's currents can be calculated by using the following equations, where, x index represents the number of phases, L_x is the inductance of each phase as given in Table 3.2. Finally, the parameters of the converters are summarized in Table 3.4.

$$I_{ph_x,av} = \frac{P_{o,max}}{V_{in,min}} \quad (3.8)$$

$$I_{ph_x,pp} = \frac{V_{in}DT_s}{L_x} \quad (3.9)$$

$$I_{ph_x,rms} = I_{ph_x,av} \sqrt{1 + \frac{(I_{ph_x,pp}/I_{ph_x,av})^2}{12}} \quad (3.10)$$

In these equations, $P_{o,max}$ is the maximum output power, $V_{in,min}$ is the minimum input voltage.

Table 3.4: Converter Parameters for Different Designs with Various Number of Phases for 15% ΔI_{in} @ 2kW Output Power Level

	1-Phase	2-Phase
Average Current(A)	13.33	6.66
Peak to Peak Ripple(A)	2	5
RMS Current(A)	13.34	6.81
Output Capacitor RMS Current(A)	6.40	3.11

The volume comparison of multi-phase boost converters with the various phases for 15% ΔI_{in} @ 2kW output power level is given in Fig. 3.3. Even though, 1-phase design has higher inductor stored energy in $mH.A^2$ it has smaller inductor volume compared to the 2-phase converter. Since commercial magnetic cores are searched and converters are designed by using these cores. Due to the limited available commercial cores, 2-phase design has a higher inductor volume in total than the converter with 1-phase. Another important component affecting the converter volume is the output capacitor of the converters. With the help of interleaved operation, the converter with 2-phase has an output capacitor RMS current value that is nearly half of the output capacitor RMS current value of the converter with 1-phase. In total as can be seen from Fig. 3.3, the 2-phase converter has a smaller volume than the converter with a single phase. However, volume comparison alone is not sufficient to determine the optimal phase number. Because one design may have higher power losses due to the increased number of phases even it has a lower volume. One design can not be considered as the best one by only considering the volume of the converter. The efficiency of the converter is also important. For this reason, power losses of the

converters are calculated.

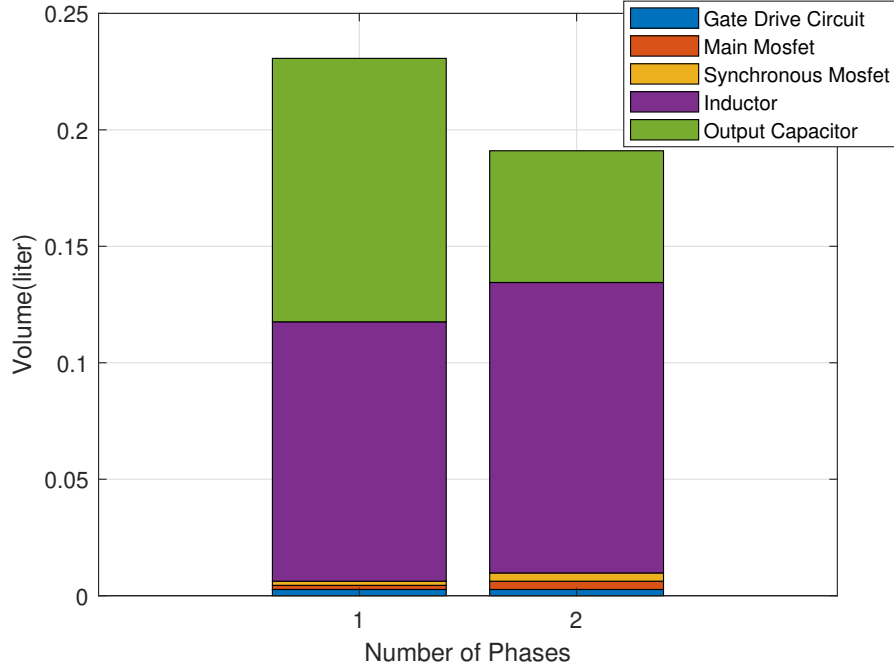


Figure 3.3: Volume comparison for converters at 150V input voltage, 2kW output power and 15% input current ripple

The losses are calculated at maximum load and minimum input voltage operating point. The converter losses include switching losses and conduction losses, $P_{switching}$ and $P_{conduction}$ of main MOSFETs, diode losses P_{diode} , DC and AC winding losses, $P_{winding,dc}$ and $P_{winding,ac}$, core losses, P_{core} of inductors and lastly gate drive losses, P_{drive} . The losses can be calculated by using the following equations.

$$P_{switching} = n \left[(E_{on} + E_{off} + E_{oss}) f_{sw} \right] \quad (3.11)$$

E_{on} is the turn-on switching energy, E_{off} is the turn-off switching energy and E_{oss} is the C_{oss} stored energy these constants are provided in the datasheets of MOSFETs. f_{sw} is the switching frequency and n number of phases.

$$P_{conduction} = n \left[I_{phx,rms}^2 R_{ds_{on}} \right] \quad (3.12)$$

$R_{ds_{on}}$ is the on-state resistance of MOSFET.

$$P_{diode} = n \left[V_{forward} I_{phx,av} (1 - D_{max}) + E_c f_{sw} \right] \quad (3.13)$$

$V_{forward}$ is the forward voltage drop of diode, D_{max} maximum value of duty cycle defined in operating conditions, E_c capacitance stored energy taken from manufacturer datasheet.

$$P_{drive} = n \left[P_{loss,supply} + V_{gs} Q_{gate} f_{sw} \right] \quad (3.14)$$

$P_{loss,supply}$ is the power loss of supply of gate driver, V_{gs} gate-source drive voltage, Q_{gate} total gate charge of the MOSFET.

The winding losses of an inductor consist of two-components. These are DC winding loss, $P_{winding,DC}$ and AC winding loss $P_{winding,AC}$. $P_{winding,AC}$ represents the high-frequency losses of the inductor. At high frequencies, skin effect and proximity effect give rise to an increase in winding losses. If the AC component of the inductors current is considerably high, placement of windings and selection of wire diameter should be done carefully.

$$P_{winding,DC} = n \left[I_{phx,av}^2 R_{winding,DC} \right] \quad (3.15)$$

$R_{winding,DC}$ is the DC resistance of inductor windings.

$$P_{winding,AC} = n \left[\left(\sqrt{I_{phx,rms}^2 - I_{phx,av}^2} \right)^2 R_{winding,ac} \right] \quad (3.16)$$

$R_{winding,DC}$ is the AC resistance of inductor windings. where, $R_{winding,DC}$ is calculated from the following formula.

$$R_{winding,DC} = \frac{R_{wire} \cdot M.L.T. \cdot N}{p} \quad (3.17)$$

R_{wire} is the resistance of wire generally given in Ω/km , $M.L.T.$ is the mean length of one turn calculated from core geometry. The ratio of $R_{winding,ac}$ to $R_{winding,dc}$ defined as σ is assumed considering number of parallel layer p for each design. p is calculated considering current density of wire by using the following formula, where J is the current density of the winding that is taken as $7 A/mm^2$.

$$p = \frac{J}{I_{phx,av}} \quad (3.18)$$

In order to take into account the proximity effect, Dowell's curve can be used [35], where it gives the ratio of AC resistance to DC resistance of winding, σ , as 10. As the ripple of the inductor current is smaller when compared to the DC value, in this case, the margin of error by assuming σ roughly in the loss account will not be significant.

However, for more accurate calculation of winding losses or for transformers where current only has AC component the proximity effect should be considered by using FEA simulations.

Calculation from Dowell's curve gives the ratio σ as 1.85 for 1 layer winding, as 4.95 for 2 layer winding, as 10 for 3 layer winding and as 17.23 for 4 layer winding. The σ and p values for all designs are also summarized in Table 3.3.

The core loss of the inductors can be calculated by using the Steinmetz equation given in Eq. 3.19. This equation considers that magnetic flux density consists of only AC component. In the literature, there are several studies on the effect of DC bias on core loss. In [36], an experimental setup is used to investigate the core loss effect. AC magnetic field density is kept constant by using an H-bridge converter by varying frequency and voltage. A boost converter with varying load is used to simulate DC magnetic field. In this way, in that study effect of DC bias on core loss is investigated. In conclusion, it is stated that DC bias results in an increase in the core losses. Some empirically obtained constants are used to make the Steinmetz equation more accurate for the DC bias condition. However, these constants are depended on the magnetic core material. Therefore, they should be derived empirically for each material. In this chapter, the effect of DC bias can not be considered analytically. Therefore, it is ignored. In Chapter 6, the DC bias effect will be considered with the help of FEA simulations.

$$P_{core} = n \left[a \frac{B_{ac}^b}{2} f_{sw}^c V_{core} \times 10^{-3} \right] \quad (3.19)$$

a is the constant for core material, B_{ac} peak to peak magnetic flux density of the inductor, b exponent of flux density in the Steinmetz equation, c exponent of the frequency, V_{core} core volume in cm^3 . Power losses at the 2kW output power level of all designs are given in Fig. 3.4. As can be seen from Table 3.3 and Table 3.4, converter with 1-phase has higher RMS current through the semiconductors and higher phase current than the converter with 2-phase. It also has a higher number of turns and hence higher winding resistance of the inductor. Therefore, converter with 1-phase has higher winding losses and conduction losses of main and synchronous MOSFET than the converter with 2-phase. Converter with 1-phase has also higher turn-off current of MOSFETs than the converter with 2-phase therefore it has higher switching losses per MOSFET. However, since the converter with 2-phase has more semicon-

ductor, total switching losses of the converter with 2-phase are higher than the converter with 1-phase. Moreover, due to the lower phase inductance than the converter with 1-phase, 2-phase converter has a higher magnetic flux density ripple which results in higher core losses. In total, as seen from Fig. 3.4, a 2-phase interleaved converter has lower power losses. In order to evaluate the overall performances of all designs, a figure of merit (FOM) is derived based on power loss, volume and cost of converters. The proposed FOM is given in below. Three parameters of converter that are affected by the number of phases are used in the FOM. These are power losses and the volume of the converters. Design with the highest FOM is considered the optimum design for specified operating conditions of the converters.

$$FOM = \frac{1}{PowerLoss(W) \cdot Volume(m^3)} \quad (3.20)$$

The performance outcomes of all designs are summarized in Table 3.5. As can be seen, a 2-phase design has a better FOM.

Table 3.5: Performance Comparison of Converters with Different Number of Phases for the Same ΔI_{in} and 2kW Output Power

	1-Phase	2-Phase
Power loss (W)	28.14	26.96
Volume (cm ³)	230	190
FOM	154.51	195.22

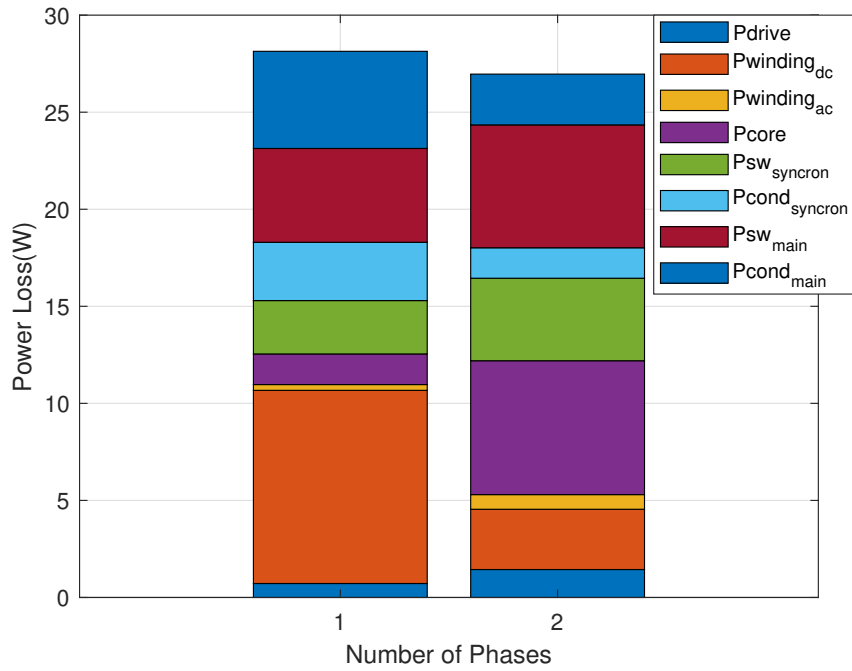


Figure 3.4: Power losses comparisons for converters at 150V input voltage, 2kW output power and 15% input current ripple

3.2.2 Comparison under the 5% Input Current Ripple

Required minimum inductance values as a function of the duty cycle for 2kW output power level are given in Fig. 3.5. For operating region $0.375 \leq D \leq 0.625$, the minimum required inductance values to satisfy desired maximum input current ripple are given in Table 3.6.

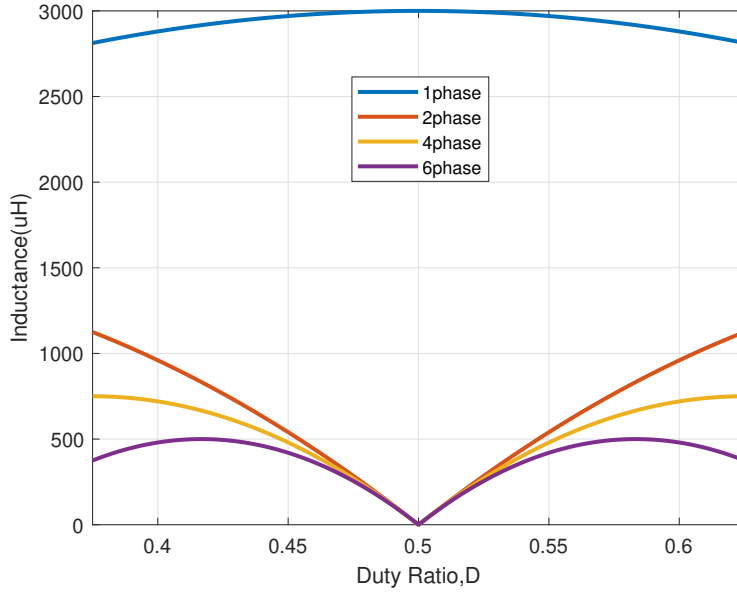


Figure 3.5: Required inductance vs duty cycle for input current ripple equals to %5 of maximum input current @2kW output power

Table 3.6: Required Minimum Inductance Values for 5% ΔI_{in} @ 2kW Output Power Level

	1-Phase	2-Phase	4-phase	6-Phase
Inductance(μH)	3000	1125	750	500

The required energy in $mH.A^2$ which is given in Eq. 3.5 is calculated. Then, the cores having that parameter greater than the calculated one are considered. Starting from the core with minimum size among the considered cores, the number of turns is calculated according to the inductance factor specified in the datasheet, A_L and inductance value. Then, by using the calculated number of turns and limiting B_{peak} to $0.3T$, minimum cross-section area, A_e is calculated by using Eq. 3.7. If the core meets that minimum cross-section area, it is selected otherwise the same design procedure is applied to the consecutive cores. Parameters of the designed inductors are given in Tab. 3.7.

Table 3.7: Inductor Parameters for Different Designs with Various Number of Phase for 5% ΔI_{in} @2kW Output Power Level

	1-Phase	2-Phase	4-phase	6-Phase
Inductance	3000 μH	1125 μH	750 μH	500 μH
B_{dc}	0.342T	0.28T	0.2T	0.15T
ΔB_{pp}	0.016T	0.03T	0.14T	0.25T
B_{peak}	0.35T	0.31T	0.27T	0.28T
Number of Turns	109	66	71	58
$R_{winding,dc}$	160m Ω	69m Ω	170m Ω	127m Ω
Cross Section Area, A_e	1080mm ²	417mm ²	183mm ²	128mm ²
Core Type	00K130LE026	00K5530E060	00K4020E060	00K4017E090
number of parallel layer, p	6	3	2	1
$\sigma = R_{winding,ac}/R_{winding,dc}$	17.23	4.95	4.95	1.85

The parameters of the converters are summarized in Table 3.8.

Table 3.8: Converter Parameters for Different Designs with Various Number of Phases for 5% ΔI_{in} @ 2kW Output Power Level

	1-Phase	2-Phase	4-phase	6-Phase
Average Current(A)	13.33	6.66	3.33	2.22
Peak to Peak Ripple(A)	0.625	1.66	2.5	3.75
RMS Current(A)	13.34	6.68	3.41	2.47
Output Capacitor Rms Current(A)	6.39	2.90	1.08	1.16

The volume comparison of multi-phase boost converters with a various phases for 5% ΔI_{in} @2kW output power level is given in Fig. 3.6. With the help of interleaved operation, output capacitor volume reduces as the number of phases increases. Moreover, in order to satisfy the 5% ΔI_{in} condition, a converter with 1-phase requires higher phase inductance. It also has a higher phase current therefore it's inductor volume is much higher than the others. As can be seen, the 4-phase converter has a minimum volume than the others. However, volume comparison alone is not sufficient to determine the optimal phase number. For this reason, another performance criteria, power

losses of designs are calculated.

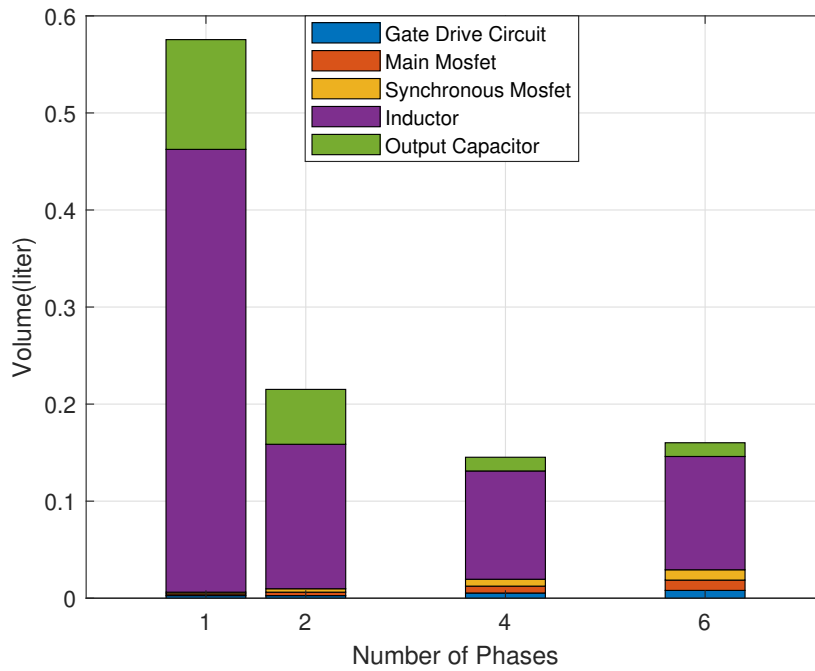


Figure 3.6: Volume comparison for converters at 150V input voltage, 2kW output power and 5% input current ripple

Power losses at the 2kW output power level of all designs are given in Fig. 3.7. Due to the higher winding resistance and higher core volume, converter with 1-phase has a higher winding losses and core loss. Converter with 6-phase has higher peak to peak magnetic flux density and higher number of magnetic cores therefore it has also higher core losses. As seen, the 2-phase interleaved converter has the minimum power losses.

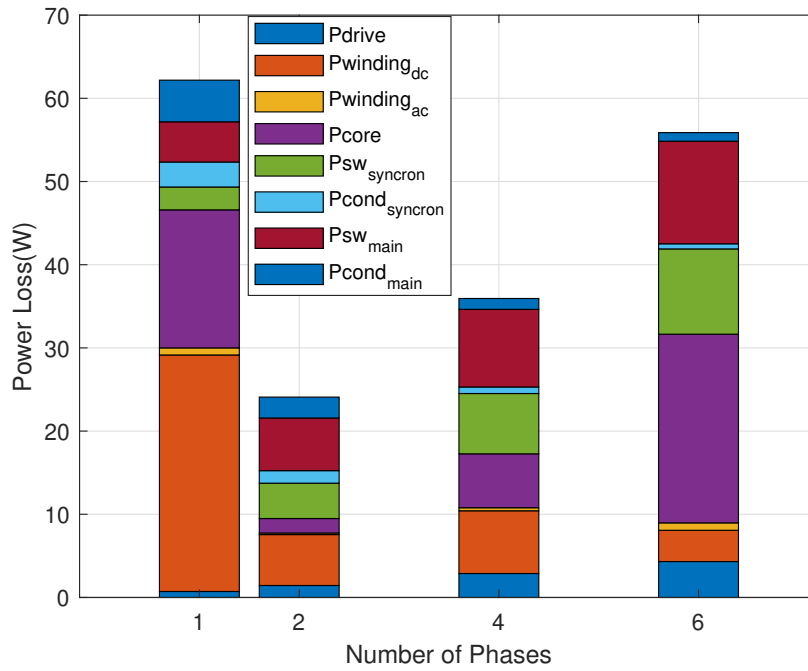


Figure 3.7: Power losses comparisons for converters at 150V input voltage, 2kW output power and 5% input current ripple

The performance outcomes of all designs are summarized in Table 3.9. As can be seen, the 2-phase design has the best FOM among all.

Table 3.9: Performance Comparison of Converters with Different Number of Phases for the Same 5% ΔI_{in} and 2kW Output Power

	1-Phase	2-Phase	4-phase	6-Phase
Power loss (W)	62.18	24.09	35.94	55.88
Volume (cm ³)	575.5	215.2	145.2	160.2
FOM	61.75	192.89	191.62	111.70

3.3 Comparisons Using the Same Inductance

In this condition, all multi-phase converters with a different phases have the same phase inductance of $500\mu H$. Therefore, inductor current ripples are the same for all

designs while input current ripple varies. As a result, input filter sizes are different since input current ripples are different. Volumes of converters are given in Fig. 3.8. When it comes to efficiency comparisons, higher power level converters become more efficient as their phase number increases. Because the most dominant part of power losses is the conduction loss which reduces with the increasing number of phases. Since the same inductor is used in all designs, the inductor current ripple and hence AC component of current is the same which results in the similar AC winding loss. In conclusion, under this comparison condition and 2kW output power level, a number of phase of 2 is the optimum regarding efficiency. Even, its volume is close to a single-phase design.

Parameters of the designed inductors is given in Tab. 3.10.

Table 3.10: Inductor Parameters for Different Designs with Various Number of Phase for the Same ΔI_L @2kW Output Power Level

	1-Phase	2-Phase	4-phase	6-Phase
Inductance	$500\mu H$	$500\mu H$	$500\mu H$	$500\mu H$
B_{dc}	$0.31T$	$0.27T$	$0.225T$	$0.19T$
ΔB_{pp}	$0.08T$	$0.16T$	$0.25T$	$0.32T$
B_{peak}	$0.35T$	$0.35T$	$0.35T$	$0.35T$
Number of Turns	52	51	58	70
$R_{winding,dc}$	$27m\Omega$	$41m\Omega$	$126m\Omega$	$127m\Omega$
Cross Section Area, A_e	$417mm^2$	$237mm^2$	$128mm^2$	$84mm^2$
Core Type	00K5530E040	00K4022E060	00K4017E090	00K3515E060
number of parallel layer, p	6	3	2	1
$\sigma = R_{winding,ac}/R_{winding,dc}$	17.23	4.95	4.95	1.85

The parameters of the converters are summarized in Table 3.11.

Table 3.11: Converter Parameters for Different Designs with Various Number of Phases for the Same ΔI_L @ 2kW Output Power Level

	1-Phase	2-Phase	4-phase	6-Phase
Average Current(A)	13.33	6.66	3.33	2.22
Peak to Peak Ripple(A)	3.75	3.75	3.75	3.75
RMS Current(A)	13.38	6.75	3.50	2.47
Output Capacitor Rms Current(A)	6.43	3.02	1.16	1.16

The volume comparison of multi-phase boost converters with a various phases for the same ΔI_L @2kW output power level is given in Fig. 3.8. For this condition since the inductances are the same, the 1-phase design has inductor volume which is close to the other designs. However, the 1-phase design suffers from output capacitor volume since it has a higher output capacitor RMS current than the others. As can be seen, the 4-phase converter has a minimum volume than the others. However, volume comparison alone is not sufficient to determine the optimal phase number. For this reason, another performance criteria, power losses of designs are calculated.

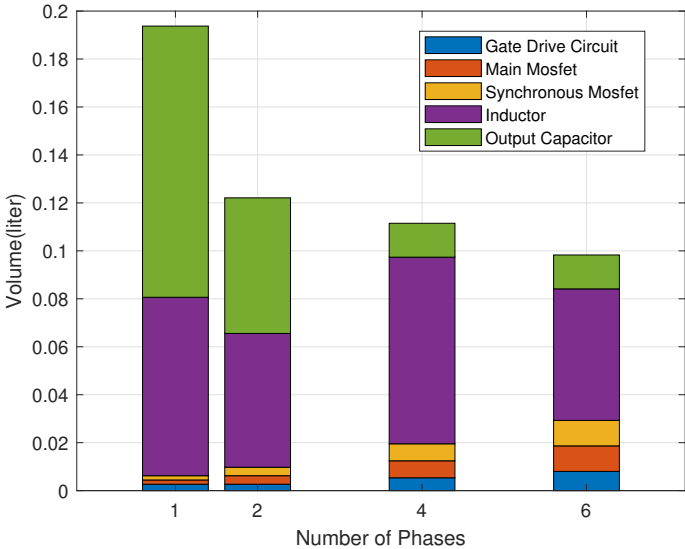


Figure 3.8: Volume comparison for converters at 150V input voltage, 2kW output power and the same inductor current ripple

Power losses at the 2kW output power level of all designs are given in Fig. 3.9. For this condition, a 1-phase converter has smaller winding resistance however due to the higher phase current its winding loss is higher than the others but now it is closer to the winding losses of other designs. Other components of the power losses increases as the number of phase increases. As a result, the 1-phase converter has lower power losses than the others.

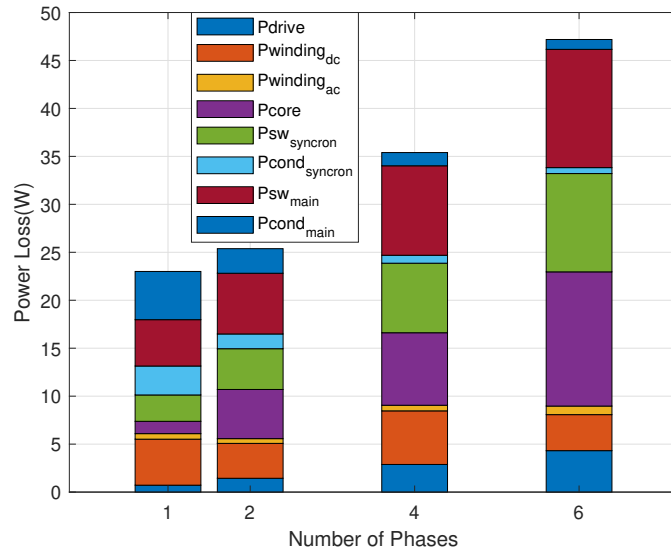


Figure 3.9: Power losses comparisons for converters at 150V input voltage, 2kW output power and 5% input current ripple

The performance outcomes of all designs are summarized in Table 3.12. As can be seen, a 2-phase design has a better FOM.

Table 3.12: Performance Comparison of Converters with Different Number of Phases for the Same % ΔI_L and 2kW Output Power

	1-Phase	2-Phase	4-phase	6-Phase
Power loss (W)	23	25.38	35.4	47.19
Volume (cm ³)	193.7	122.1	111.5	98.3
FOM	224.6	322.7	253.3	215.5

3.4 Chapter Summary

In this chapter, several multi-phase interleaved boost converters with various number of phases are designed and compared by considering converter efficiency and volume. Designs of the converters are conducted under the different operating conditions where input current ripple is kept constant at 2 different values and the same inductance is used for phases of all converters. A figure of merit based on the power losses of the converters and volumes of the converters are used to compare the overall performances of the converters. For 15% input current ripple, a converter with a 2-phase design has a better FOM. Another operating condition where input current ripple kept as 5% of the maximum input current is used and converters are designed. For this case, it is expected that converters with the higher number of phases have less inductor current ripple and hence less RMS current. Therefore their efficiencies are expected closer to the converters with less number of phases. For this design condition, 2-phase design and 4-phase designs are found to have higher FOM than the others. Converter with 2-phase design has lowest power losses and slightly higher FOM when compared to others. The last design condition is that the same inductance is used for all designs. For this case, the inductor current ripples are the same for all designs. Inductors of the converters are designed to have the same inductance. Results of this condition show that converter with a 2-phase design has the best FOM among them all. In conclusion, for all design conditions, converter with 2-phase is found to have the best FOM among all converters. As a result, in this study number of phases is selected as 2 for the 2kW converters considered in the following chapters.

CHAPTER 4

MATHEMATICAL ANALYSIS OF TWO-PHASE INTERLEAVED BOOST CONVERTERS WITH VARIOUS INDUCTOR TOPOLOGIES

Several multi-phase converters with the number of phases of 2, 4, 6, 8 and 10 are designed for 2kW and 100kW output power levels are designed in Chapter 3. The designs are performed such that all designs have the same input current ripple which is a critical parameter as stated in Chapter 2. It was shown that for 2kW output power level, 2-phase interleaved boost converter gives the best performance. As a result, the number of phases is selected as 2 for the 2kW converter that is designed in this study. In the case of a two-phase interleaved converter, loosely-coupled inductor, closely-coupled inductor and integrated winding coupled inductor topologies are mostly used to achieve a reduction in the size of magnetic components compared to a converter with discrete inductors. The circuit schematic of a two-phase interleaved boost converter with various inductor topologies is given in Fig. 4.1.

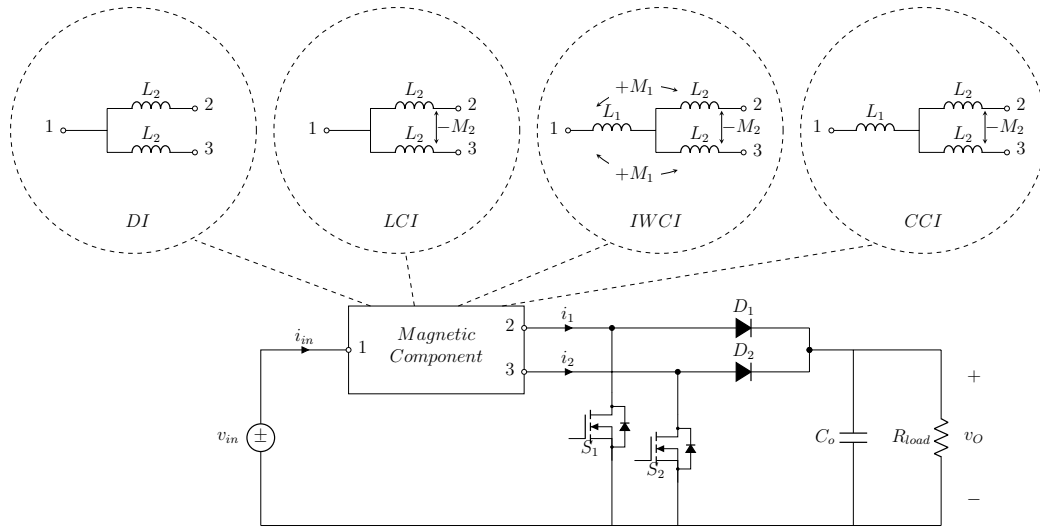


Figure 4.1: Two-phase interleaved boost converter with various inductor topologies

In this chapter, magnetic analysis of the DI, LCI, IWCI and CCI type inductors and electrical analysis of the converters with inductors are presented.

4.1 Discrete Inductors (DI)

The circuit schematic of a two-phase boost converter with discrete inductors is shown in Fig. 4.2.

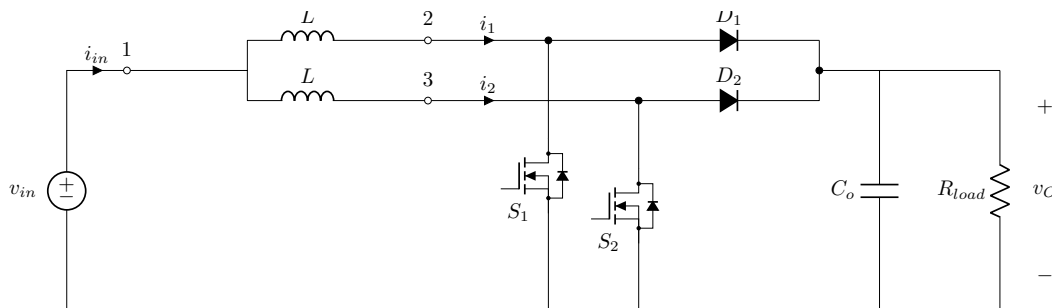


Figure 4.2: Two-phase boost converter with discrete inductors

4.1.1 Magnetic Analysis

The magnetic and electrical connection structure of a DI is shown in Fig. 4.3.

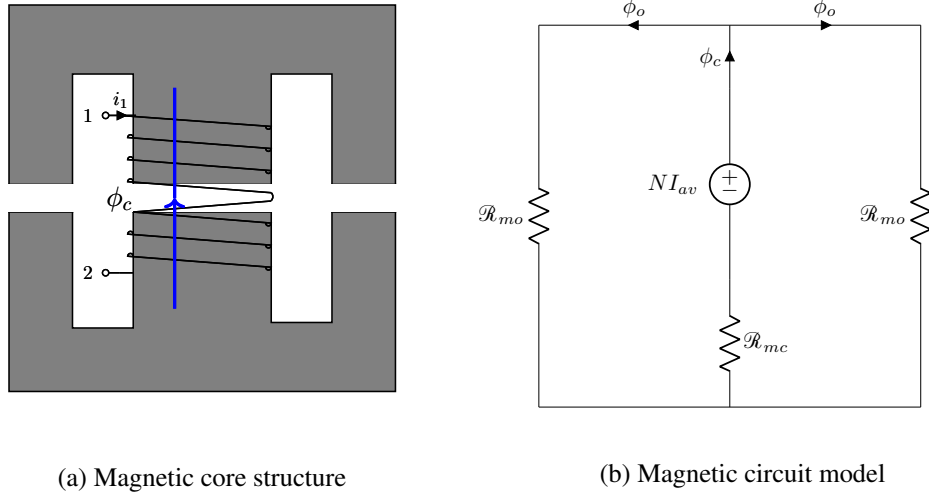


Figure 4.3: Magnetic core structure and magnetic circuit model of a DI

From the magnetic circuit model the following equation can be obtained.

$$NI_{av} = \Phi_o \mathcal{R}_{mo} + \Phi_c \mathcal{R}_{mc} \quad (4.1)$$

In this equations, N is the number of turns, I_{av} average value of the current of the phases, Φ_o magnetic flux on the outer leg, \mathcal{R}_{mo} reluctance of the outer leg of the core, Φ_c magnetic flux on the center leg, \mathcal{R}_{mc} reluctance of the center leg of the core.

The average or DC component of the magnetic flux of the outer legs and center leg of the DI can be written as in Eq. 4.2.

$$\begin{aligned} \Phi_c &= 2\Phi_o = \frac{NI_{av}}{\mathcal{R}_{mx}} \\ \mathcal{R}_{mx} &= \frac{\mathcal{R}_{mo} + 2\mathcal{R}_{mc}}{2} \end{aligned} \quad (4.2)$$

AC component of the magnetic flux can be written as in Eq. 4.3.

$$\begin{aligned}
V_{L,1} &= N \frac{d\phi_c}{dt} \\
V_{L,2} &= N \frac{d\phi_c}{dt}
\end{aligned}
\tag{4.3}$$

In these equations, $V_{L,1}$ is the voltage applied across the phase1 inductor, $V_{L,2}$ is the voltage applied across the phase2 inductor. The equation of AC component or peak to peak ripple of the magnetic flux of the center leg of DI is given in Eq. 4.4. The magnetic fluxes of the outer legs are equal to half of the center leg magnetic flux.

$$\phi_{c,pp} = \frac{V_{in}DT_s}{N}
\tag{4.4}$$

The peak value of the magnetic flux can be written as a sum of the DC component and half of the AC component of the magnetic flux as shown in Fig. 4.4. The peak value of the magnetic flux of the DI can be obtained by using Eq. 4.2 and Eq. 4.4. The equation for the peak values of the magnetic flux of the center leg is given in Eq. 4.5.

$$\phi_{c,max} = \frac{NI_{av}}{0.5\mathcal{R}_{mo} + \mathcal{R}_{mc}} + \frac{V_{in}DT_s}{2N}
\tag{4.5}$$

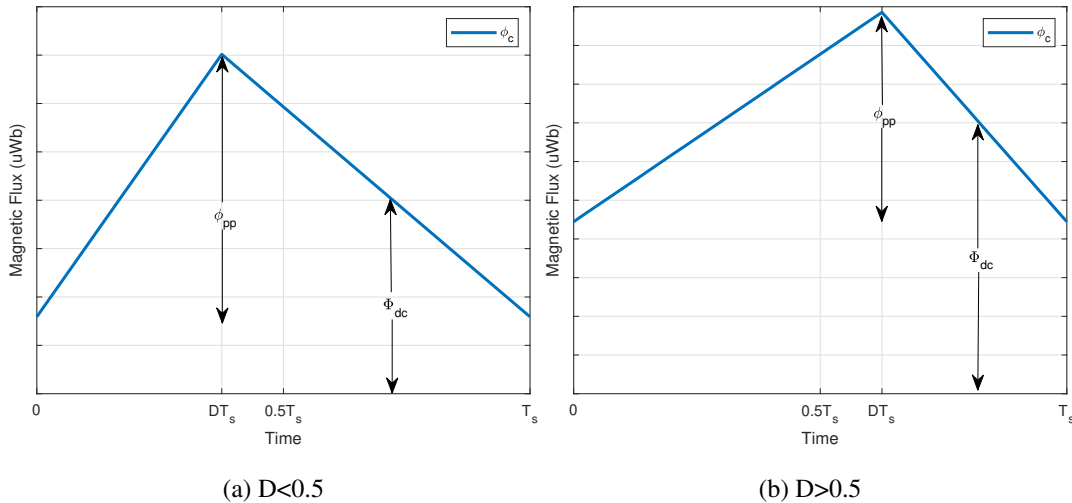


Figure 4.4: Waveforms of the magnetic fluxes in the DI core

4.1.2 Electrical Analysis of the Interleaved Boost Converter with Discrete Inductors

Similar to the converters with other inductor topologies, a two-phase interleaved boost converter with discrete inductors consist of 4 different operating modes. These are can be classified as mode1 ($S_1 : ON, S_2 : OFF$), mode2 ($S_1 : OFF, S_2 : ON$), mode3 ($S_1 : OFF, S_2 : OFF$) and mode4 ($S_1 : ON, S_2 : ON$). Operating modes and current waveforms of the converter with discrete inductors are shown in Fig. 2.2. Electrical analysis of the converter can be made by writing KVL voltage equations for each phase according to the switching state or operating mode. The KVL across phase 1 and phase 2 can be written as below.

$$\begin{aligned} V_{L,1} &= L \frac{di_1}{dt} \\ V_{L,2} &= L \frac{di_2}{dt} \end{aligned} \quad (4.6)$$

In these equations, L inductances of the inductors of the phases. Applied voltages to the phases of the converter can be expressed as:

$$V_{L,1} = \begin{cases} V_{in}; & S_1 : ON \\ V_{in} - V_o; & S_1 : OFF \end{cases} \quad (4.7)$$

$$V_{L,2} = \begin{cases} V_{in}; & S_2 : ON \\ V_{in} - V_o; & S_2 : OFF \end{cases} \quad (4.8)$$

Waveforms of the input and phase currents of the converter with DI are given in Fig. 2.2. By using Eq. 4.6, Eq. 4.7 and Eq. 4.8 and writing KVL across the phases of the converter and solving them together inductor and input current ripple equations can be obtained for each operating mode. The equations are listed in Table 4.1.

Table 4.1: Current Ripple Equations of the Converter with DI in Different Converter Operating Modes

$Mode1(S_1 : ON, S_2 : OFF)$	$Mode2(S_1 : OFF, S_2 : ON)$
$\begin{aligned} \frac{di_1}{dt} &= \frac{V_{in}}{L} \\ \frac{di_2}{dt} &= \frac{(V_{in} - V_o)}{L} \quad (4.9) \\ \frac{di_{in}}{dt} &= \frac{V_o(1 - 2D)}{L} \end{aligned}$	$\begin{aligned} \frac{di_1}{dt} &= \frac{(V_{in} - V_o)}{L} \\ \frac{di_2}{dt} &= \frac{V_{in}}{L} \quad (4.10) \\ \frac{di_{in}}{dt} &= \frac{V_o(1 - 2D)}{L} \end{aligned}$
$Mode3(S_1 : OFF, S_2 : OFF)$	$Mode4(S_1 : ON, S_2 : ON)$
$\begin{aligned} \frac{di_1}{dt} = \frac{di_2}{dt} &= \frac{(V_{in} - V_o)}{L} \quad (4.11) \\ \frac{di_{in}}{dt} &= \frac{2(V_{in} - V_o)}{L} \end{aligned}$	$\begin{aligned} \frac{di_1}{dt} = \frac{di_2}{dt} &= \frac{V_{in}}{L} \quad (4.12) \\ \frac{di_{in}}{dt} &= \frac{2V_{in}}{L} \end{aligned}$

Peak to peak inductor current ripple can be written by using current equations in mode1 for $D \leq 0.5$ and in mode2 for $D \geq 0.5$. Equations for the peak to peak input and inductor current ripples are given in below.

$$\Delta I_{L,pp} = \begin{cases} \frac{V_{in}DT_s}{L}; & D \leq 0.5 \\ \frac{(V_{in} - V_o)(1 - D)T_s}{L}; & D \geq 0.5 \end{cases} \quad (4.13)$$

$$\Delta I_{i_{in},pp} = \begin{cases} \frac{2(V_{in} - V_o)(0.5 - D)T_s}{L}; & D \leq 0.5 \\ \frac{2V_{in}(D - 0.5)T_s}{L}; & D \geq 0.5 \end{cases} \quad (4.14)$$

4.2 Loosely-Coupled Inductor (LCI)

Loosely-Coupled inductor (LCI) is mainly known as integrated transformer and inductor. It's magnetic core structure with winding layout is shown in Fig. 4.5. Mostly

used magnetic core types for LCI are E-E and E-I types of cores. LCI consists of two windings wound on the outer leg's of the magnetic core. These windings are inversely coupled to each other and connected to phases of a two-phase interleaved boost converter. The coupling between the windings is controlled by varying the length of the air-gap on the center leg of the magnetic core.

4.2.1 Magnetic Analysis

The magnetic and electrical connection structure and magnetic circuit model of the LCI are shown in Fig. 4.5. The direction of magnetic fluxes in the core are labeled.

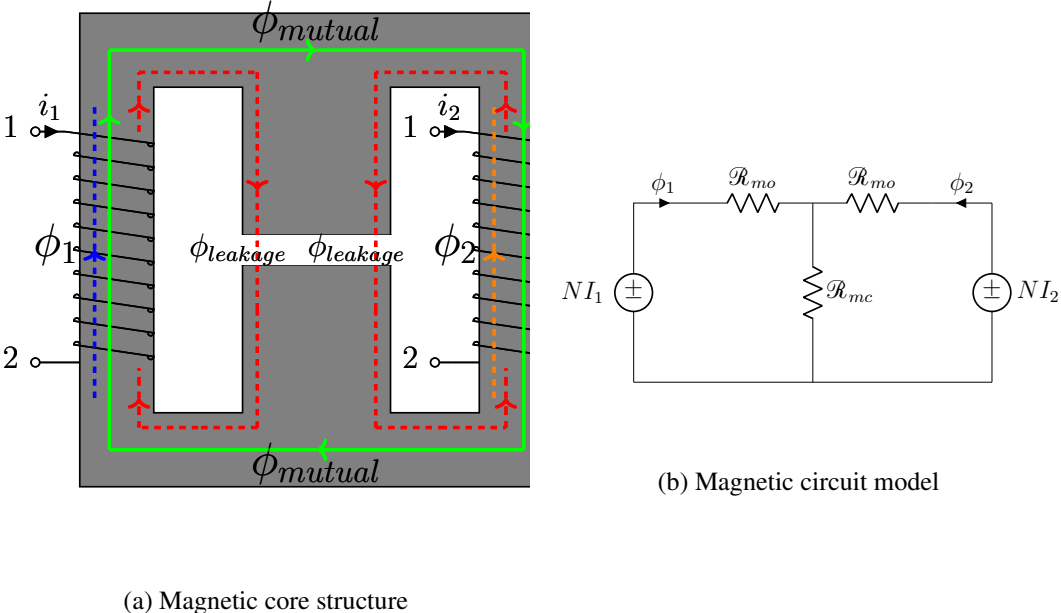


Figure 4.5: Magnetic core structure and magnetic circuit model a LCI

From the magnetic circuit model the following equations can be obtained.

$$\begin{aligned}
 NI_1 &= \Phi_1 \mathcal{R}_{mo} + (\Phi_1 + \Phi_2) \mathcal{R}_{mc} \\
 NI_2 &= \Phi_2 \mathcal{R}_{mo} + (\Phi_1 + \Phi_2) \mathcal{R}_{mc}
 \end{aligned}
 \tag{4.15}$$

For simplicity, $I_1 = I_2 = I_{av}$ and $\Phi_1 = \Phi_2 = \Phi_o$ equality's are assumed. The average or DC component of the magnetic flux of the outer legs and center leg can be written

as in Eq. 4.16.

$$\begin{aligned}\Phi_o &= \frac{NI_{av}}{\mathcal{R}_{mo} + 2\mathcal{R}_{mc}} \\ \Phi_c = 2\Phi_o &= \frac{2NI_{av}}{\mathcal{R}_{mo} + 2\mathcal{R}_{mc}}\end{aligned}\quad (4.16)$$

In these equations, N is the number of turns of the windings, I_1, I_2, I_{av} are the average or DC component of phase currents, Φ_1, Φ_2, Φ_o are the average or DC component of the outer leg magnetic fluxes, Φ_c average component of the center leg magnetic flux, \mathcal{R}_{mo} reluctance of the outer legs of the core, \mathcal{R}_{mc} reluctance of the center leg. AC component of the magnetic fluxes of outer legs can be written as in Eq. 4.17. The relationship between the outer leg's magnetic fluxes, the center leg magnetic fluxes, leakage and mutual magnetic fluxes can be written as in Eq. 4.18. AC components of the leakage and mutual fluxes are given in Eq. 4.19.

$$\begin{aligned}V_{L1} &= N \frac{d\phi_1}{dt} \\ V_{L2} &= N \frac{d\phi_2}{dt}\end{aligned}\quad (4.17)$$

$$\begin{aligned}\frac{d\phi_1}{dt} &= \frac{d\phi_{leakage} + d\phi_{mutual}}{dt} \\ \frac{d\phi_2}{dt} &= \frac{d\phi_{leakage} - d\phi_{mutual}}{dt}\end{aligned}\quad (4.18)$$

$$\phi_c = 2\phi_{leakage}$$

$$\begin{aligned}\frac{d\phi_{leakage}}{dt} &= \frac{V_{L1} + V_{L2}}{2N} \\ \frac{d\phi_{mutual}}{dt} &= \frac{V_{L1} - V_{L2}}{2N}\end{aligned}\quad (4.19)$$

In these equations, V_{L1} and V_{L2} are voltages applied to the phase1's and phase2's terminals, respectively. $\phi_{leakage}$ is the flux that is not linked between the windings, ϕ_{mutual} is the flux that is linked between the windings. The peak to peak ripple of outer leg magnetic fluxes are the same for $D < 0.5$ and $D > 0.5$ operating conditions, and it can be written during the switch on-state. The equations of AC component or peak to peak ripple of the magnetic flux of outer legs are given in Eq. 4.20.

$$\phi_{1,pp} = \phi_{2,pp} = \frac{V_{in}DT_s}{N}\quad (4.20)$$

On the other hand, peak to peak ripple of the magnetic flux of the center leg is not the same for $D < 0.5$ and $D > 0.5$ operating conditions. As seen from Eq. 4.18, the ripple of the center leg magnetic flux depends on voltages applied to both phases. For $D < 0.5$, it can be calculated during mode1. For $D > 0.5$, it can be calculated during mode4. The operating modes are shown in Fig. 2.6. The equations of AC component or peak to peak ripple of the magnetic flux of the center leg are given in Eq. 4.21.

$$\phi_{c,pp} = \begin{cases} \frac{1 - 2D}{1 - D} \frac{V_{in}DT_s}{N}; & D \leq 0.5 \\ \frac{2V_{in}(D - 0.5)T_s}{N}; & D \geq 0.5 \end{cases} \quad (4.21)$$

The maximum values of the fluxes in each leg can be written as a sum of the DC component and half of the AC component of the magnetic fluxes as shown in Fig. 4.6. The maximum values of the fluxes on the center and outer legs can be obtained by using Eq. 4.16, Eq. 4.20 and Eq. 4.21. The equations for maximum values of the fluxes on the outer legs and center leg are given in Eq. 4.22 and Eq. 4.23, respectively.

$$\phi_{o,max} = \frac{NI_{av}}{\mathcal{R}_{mo} + 2\mathcal{R}_{mc}} + \frac{1}{2} \cdot \frac{V_{in}DT_s}{N} \quad (4.22)$$

$$\phi_{c,max} = \begin{cases} \frac{2NI_{av}}{\mathcal{R}_{mo} + 2\mathcal{R}_{mc}} + \frac{1}{2} \cdot \frac{1 - 2D}{1 - D} \frac{V_{in}DT_s}{N}; & D \leq 0.5 \\ \frac{2NI_{av}}{\mathcal{R}_{mo} + 2\mathcal{R}_{mc}} + \frac{1}{2} \cdot \frac{2V_{in}(D - 0.5)T_s}{N}; & D \geq 0.5 \end{cases} \quad (4.23)$$

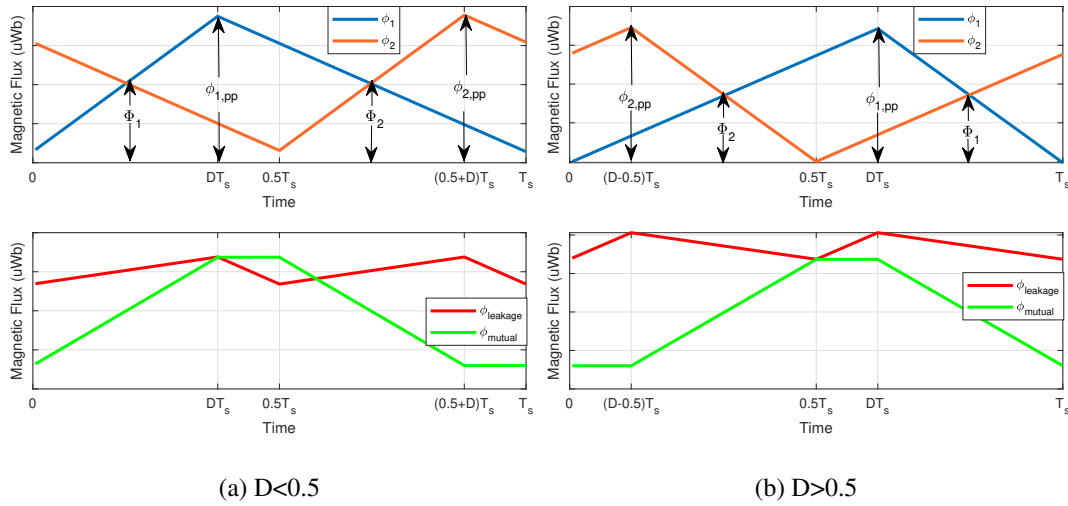
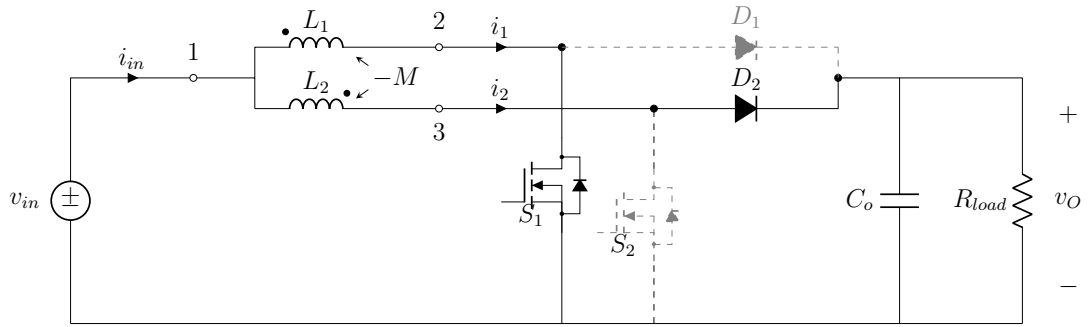


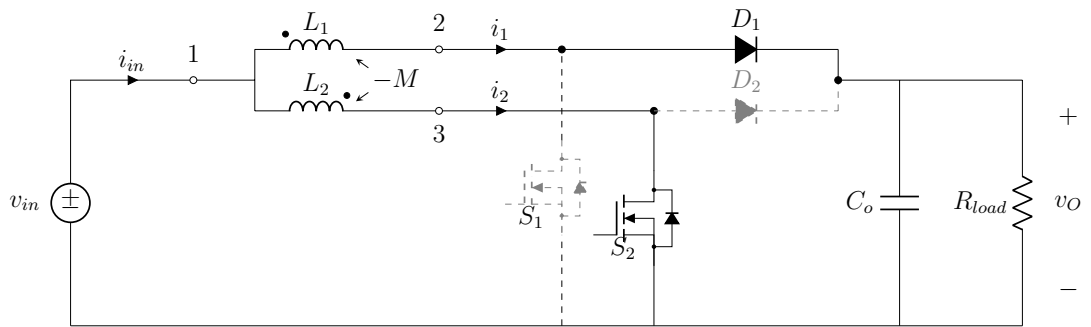
Figure 4.6: Waveforms of the magnetic fluxes in the LCI core

4.2.2 Electrical Analysis of the Interleaved Boost Converter with LCI

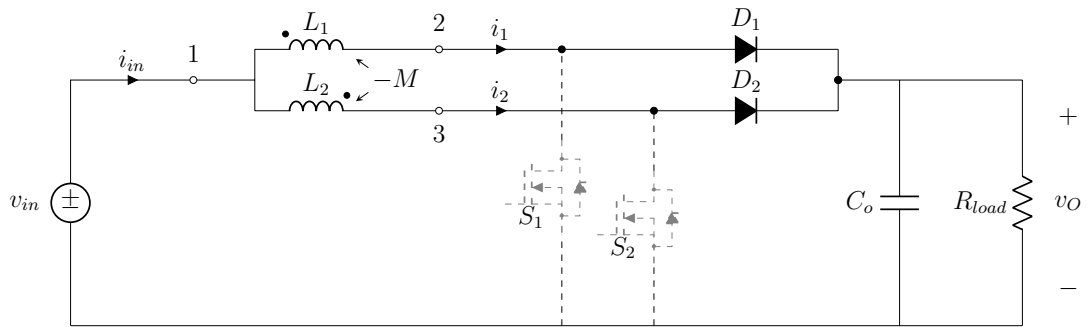
Two-phase interleaved boost converter with inversely coupled inductor consists of 4 different operating modes similar with the converter with discrete inductors. The operating modes of the converter with LCI are shown in Fig. 4.7. Electrical analysis of the converter can be made by writing KVL voltage equations for each phase according to the switching state or operating mode.



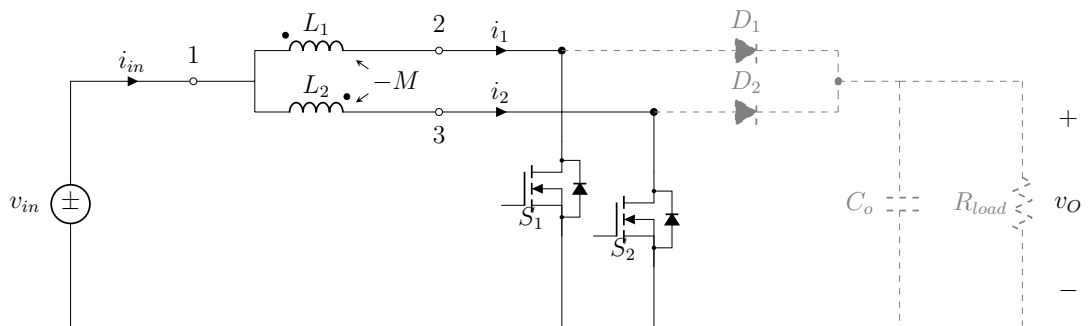
(a) mode1 ($S_1 : ON, S_2 : OFF$)



(b) mode2 ($S_1 : OFF, S_2 : ON$)



(c) mode3 ($S_1 : OFF, S_2 : OFF$)



(d) mode4 ($S_1 : ON, S_2 : ON$)

Figure 4.7: Operating modes of an interleaved two-phase boost converter with LCI

According to operating modes, the KVL equations for the phases of the converter can be written as follows.

In mode1:

$$\begin{aligned} V_{in} &= L_1 \frac{di_1}{dt} - M \frac{di_2}{dt} \\ V_{in} - V_o &= -M \frac{di_1}{dt} + L_2 \frac{di_2}{dt} \end{aligned} \quad (4.24)$$

In mode2:

$$\begin{aligned} V_{in} - V_o &= L_1 \frac{di_1}{dt} - M \frac{di_2}{dt} \\ V_{in} &= -M \frac{di_1}{dt} + L_2 \frac{di_2}{dt} \end{aligned} \quad (4.25)$$

In mode3:

$$\begin{aligned} V_{in} - V_o &= L_1 \frac{di_1}{dt} - M \frac{di_2}{dt} \\ V_{in} - V_o &= -M \frac{di_1}{dt} + L_2 \frac{di_2}{dt} \end{aligned} \quad (4.26)$$

In mode4:

$$\begin{aligned} V_{in} &= L_1 \frac{di_1}{dt} - M \frac{di_2}{dt} \\ V_{in} &= -M \frac{di_1}{dt} + L_2 \frac{di_2}{dt} \end{aligned} \quad (4.27)$$

In these equations, V_{in} is the input voltage, V_{out} output voltage, i_1 and i_2 are the phase 1 and phase 2 current, respectively. L_1 and L_2 are the phase 1 and phase 2 self inductances, respectively. M is the mutual inductance between the windings of the phases. The windings of phases are designed to be identical. Therefore, phase inductances can be written as $L_1 = L_2 = L$. By solving Eq. 4.24, Eq. 4.25, Eq. 4.26 and Eq. 4.27 together inductor and input current ripple equations can be obtained for each operating modes. The equations are listed in Table 4.2.

Table 4.2: Current Ripple Equations of the Converter with LCI in Different Converter Operating Modes

$Mode1(S_1 : ON, S_2 : OFF)$	$Mode2(S_1 : OFF, S_2 : ON)$
$\begin{aligned} \frac{di_1}{dt} &= \frac{1}{L-M}(V_{in} - \frac{V_o}{2}) + \frac{1}{L+M}(\frac{V_o}{2}) \\ \frac{di_2}{dt} &= \frac{1}{L-M}(V_{in} - \frac{V_o}{2}) - \frac{1}{L+M}(\frac{V_o}{2}) \\ \frac{di_{in}}{dt} &= \frac{2}{L-M}(V_{in} - \frac{V_o}{2}) \end{aligned} \quad (4.28)$	$\begin{aligned} \frac{di_1}{dt} &= \frac{1}{L-M}(V_{in} - \frac{V_o}{2}) - \frac{1}{L+M}(\frac{V_o}{2}) \\ \frac{di_2}{dt} &= \frac{1}{L-M}(V_{in} - \frac{V_o}{2}) + \frac{1}{L+M}(\frac{V_o}{2}) \\ \frac{di_{in}}{dt} &= \frac{2}{L-M}(V_{in} - \frac{V_o}{2}) \end{aligned} \quad (4.29)$
$Mode3(S_1 : OFF, S_2 : OFF)$	$Mode4(S_1 : ON, S_2 : ON)$
$\begin{aligned} \frac{di_1}{dt} = \frac{di_2}{dt} &= \frac{1}{L-M}(V_{in} - V_o) \\ \frac{di_{in}}{dt} &= \frac{2}{L-M}(V_{in} - V_o) \end{aligned} \quad (4.30)$	$\begin{aligned} \frac{di_1}{dt} = \frac{di_2}{dt} &= \frac{1}{L-M}V_{in} \\ \frac{di_{in}}{dt} &= \frac{2}{L-M}V_{in} \end{aligned} \quad (4.31)$

As seen in Fig. 2.6, the peak to peak inductor current ripple can be written by using current equation in mode1 for $D \leq 0.5$ and in mode2 for $D \geq 0.5$. Equations for the peak to peak input and inductor current ripple are given in below.

$$\Delta I_{L,pp} = \begin{cases} \left[\frac{1}{L-M}(V_{in} - \frac{V_o}{2}) + \frac{1}{L+M}(\frac{V_o}{2}) \right] DT_s; & D \leq 0.5 \\ \left[\frac{1}{L-M}(V_{in} - \frac{V_o}{2}) - \frac{1}{L+M}(\frac{V_o}{2}) \right] (1-D)T_s; & D \geq 0.5 \end{cases} \quad (4.32)$$

$$\Delta I_{in,pp} = \begin{cases} \left[\frac{2}{L-M}(V_{in} - \frac{V_o}{2}) \right] (0.5 - D)T_s; & D \leq 0.5 \\ \left[\frac{2}{L-M}V_{in} \right] (D - 0.5)T_s; & D \geq 0.5 \end{cases} \quad (4.33)$$

4.3 Integrated Winding Coupled Inductor (IWCI)

The terminal connections and inductances of an IWCI can be seen in Fig. 4.8.

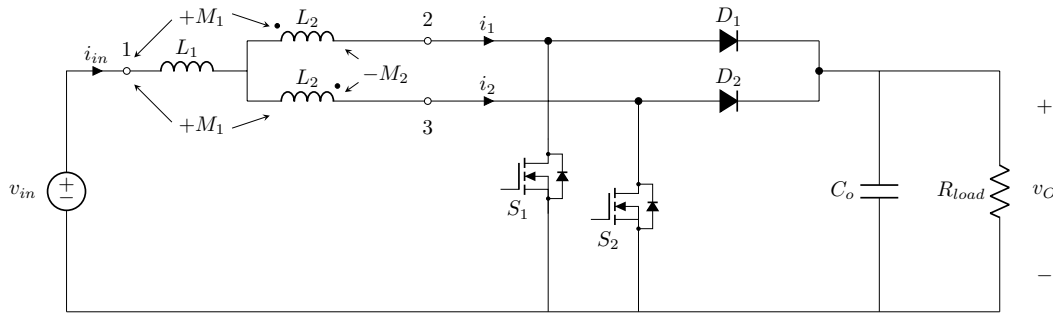


Figure 4.8: Two-phase interleaved boost converter with IWCI

4.3.1 Magnetic Analysis

The magnetic and electrical connection structure and magnetic circuit model of the IWCI are shown in Fig. 4.9. The direction of magnetic fluxes in the core is labeled. As can be seen, this topology has 3 windings. The winding wound on the center leg of a EE core is connected in series to the input source while the other windings are connected to the phases of the converter. Center winding is directly coupled to the other windings whereas outer windings are inversely coupled among themselves. The mutual inductance between the outer leg windings is controlled by adjusting the air-gap length in the center leg. Center leg winding is connected series to the outer leg windings.

From the magnetic circuit model, the following equations can be obtained.

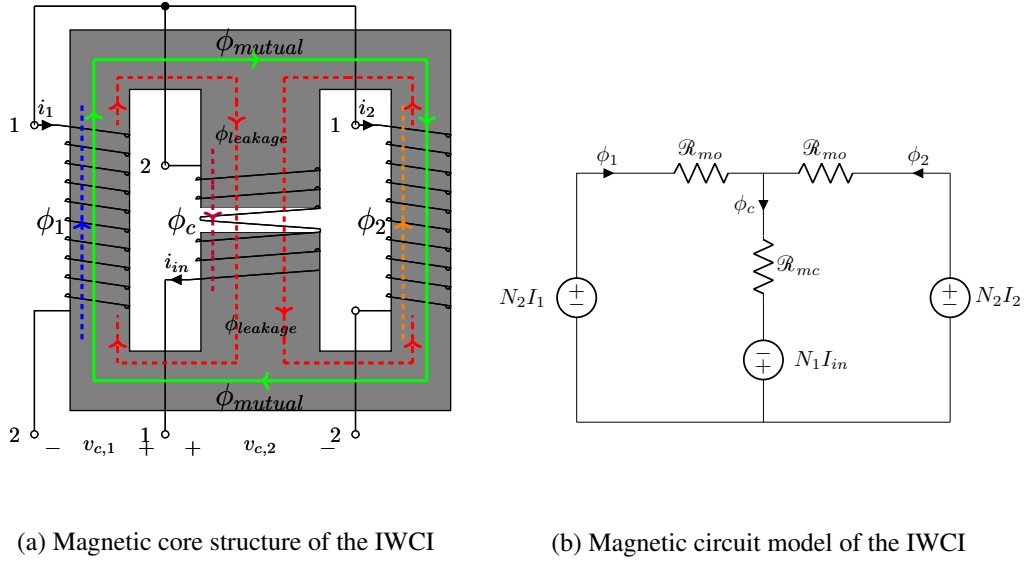


Figure 4.9: Magnetic core structure and magnetic circuit model of the IWCI

$$\begin{aligned}
 N_2 I_1 + N_1 I_{in} &= \Phi_1 \mathcal{R}_{mo} + \Phi_c \mathcal{R}_{mc} \\
 N_2 I_2 + N_1 I_{in} &= \Phi_2 \mathcal{R}_{mo} + \Phi_c \mathcal{R}_{mc} \\
 I_{in} &= I_1 + I_2 = 2I_{av} \\
 \Phi_c &= \Phi_1 + \Phi_2 = 2\Phi_o
 \end{aligned} \tag{4.34}$$

In these equations, N_1 is the number of turns of center leg winding, N_2 is the number of turns of outer leg windings, Φ_1, Φ_2 and Φ_o , are the average or DC component of the outer leg magnetic fluxes, Φ_c is the average or DC component of magnetic flux of the center leg. The average or DC component of the magnetic flux of the outer legs and center leg can be written as in Eq. 4.35.

$$\begin{aligned}
 \Phi_o &= \frac{(2N_1 + N_2)I_{av}}{\mathcal{R}_{mo} + 2\mathcal{R}_{mc}} \\
 \Phi_c = 2\Phi_o &= \frac{(2N_1 + N_2)2I_{av}}{\mathcal{R}_{mo} + 2\mathcal{R}_{mc}}
 \end{aligned} \tag{4.35}$$

The AC component of the magnetic flux of the outer legs can be written as in Eq. 4.17. The relationship between the outer leg's magnetic flux, the center leg magnetic flux, leakage and mutual magnetic flux can be written as in Eq. 4.37. The AC components of the leakage and mutual fluxes are given in Eq. 4.38.

$$\begin{aligned}
V_{1,2} &= N_1 \frac{d\phi_c}{dt} + N_2 \frac{d\phi_1}{dt} \\
V_{1,3} &= N_1 \frac{d\phi_c}{dt} + N_2 \frac{d\phi_2}{dt} \\
\frac{d\phi_c}{dt} &= \frac{d\phi_1}{dt} + \frac{d\phi_2}{dt}
\end{aligned} \tag{4.36}$$

$$\begin{aligned}
\frac{d\phi_1}{dt} &= \frac{d\phi_{leakage} + d\phi_{mutual}}{dt} \\
\frac{d\phi_2}{dt} &= \frac{d\phi_{leakage} - d\phi_{mutual}}{dt}
\end{aligned} \tag{4.37}$$

$$\begin{aligned}
\frac{d\phi_{leakage}}{dt} &= \frac{V_{1,2} + V_{1,3}}{2(2N_1 + N_2)} \\
\frac{d\phi_{mutual}}{dt} &= \frac{V_{1,2} - V_{1,3}}{2N_2}
\end{aligned} \tag{4.38}$$

In these equations, $V_{1,2}$ is the voltage applied across the center winding and phase 1 winding, $V_{1,3}$ is the voltage applied across the center winding and phase 2 winding. The terminals 1,2 and 3 are labeled in Fig. 4.8. Peak to peak ripple of the outer leg magnetic fluxes can be calculated separately for $D < 0.5$ and $D > 0.5$ operating conditions. For $D < 0.5$, it can be calculated during mode1 ($S_1 : ON, S_2 : OFF$). For $D > 0.5$, it can be calculated during mode2 ($S_1 : OFF, S_2 : ON$). The equations of AC components or peak to peak ripples of the magnetic fluxes of the outer legs are given in Eq. 4.39.

$$\phi_{o,pp} = \begin{cases} \frac{N_2 V_{in} + N_1 V_o}{N_2(2N_1 + N_2)} DT_s; & D \leq 0.5 \\ \frac{(N_1 + N_2)V_o - N_2 V_{in}}{N_2(2N_1 + N_2)} (1 - D)T_s; & D \geq 0.5 \end{cases} \tag{4.39}$$

Peak to peak ripple of the magnetic fluxes of the center leg is not the same for $D < 0.5$ and $D > 0.5$ operating conditions. As seen from Eq. 4.36, the ripple of center leg magnetic flux depends on voltages applied to both phases. For $D < 0.5$, it can be calculated during mode1. For $D > 0.5$, it can be calculated during mode2. The equations of AC components or peak to peak ripples of the magnetic fluxes of the center leg are given in Eq. 4.40.

$$\phi_{c,pp} = \begin{cases} \frac{2V_{in} - V_o}{2N_1 + N_2} DT_s; & D \leq 0.5 \\ \frac{V_o - 2V_{in}}{2N_1 + N_2} (1 - D)T_s; & D \geq 0.5 \end{cases} \tag{4.40}$$

The maximum values of the magnetic fluxes in each leg can be written as a sum of the DC component and half of the AC component of the magnetic fluxes as shown in Fig. 4.10. The maximum values of the magnetic fluxes of the center and the outer leg can be obtained by using Eq. 4.35, Eq. 4.39 and Eq. 4.40. The equations for maximum values of the magnetic fluxes of the outer legs and center leg are given in Eq. 4.41 and Eq. 4.42, respectively.

$$\phi_{o,max} = \begin{cases} \frac{(2N_1 + N_2)I_{av}}{\mathcal{R}_{mo} + 2\mathcal{R}_{mc}} + \frac{1}{2} \cdot \frac{N_2V_{in} + N_1V_o}{N_2(2N_1 + N_2)}DT_s; & D \leq 0.5 \\ \frac{(2N_1 + N_2)I_{av}}{\mathcal{R}_{mo} + 2\mathcal{R}_{mc}} + \frac{1}{2} \cdot \frac{(N_1 + N_2)V_o - N_2V_{in}}{N_2(2N_1 + N_2)}(1 - D)T_s; & D \geq 0.5 \end{cases} \quad (4.41)$$

$$\phi_{c,max} = \begin{cases} \frac{(2N_1 + N_2)2I_{av}}{\mathcal{R}_{mo} + 2\mathcal{R}_{mc}} + \frac{1}{2} \cdot \frac{2V_{in} - V_o}{2N_1 + N_2}DT_s; & D \leq 0.5 \\ \frac{(2N_1 + N_2)2I_{av}}{\mathcal{R}_{mo} + 2\mathcal{R}_{mc}} + \frac{1}{2} \cdot \frac{V_o - 2V_{in}}{2N_1 + N_2}(1 - D)T_s; & D \geq 0.5 \end{cases} \quad (4.42)$$

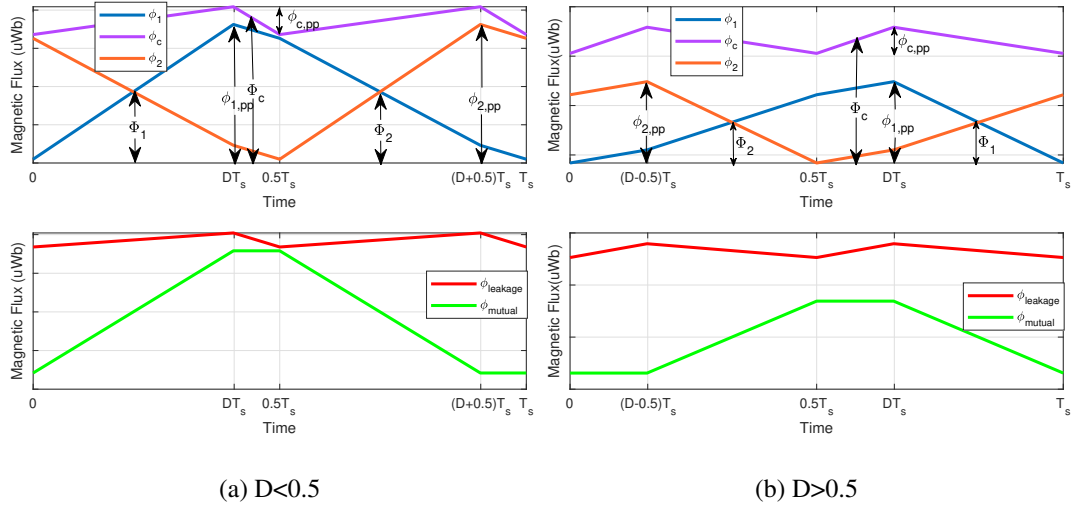


Figure 4.10: Waveforms of the magnetic fluxes in the IWCI core

4.3.2 Electrical Analysis of the Interleaved Boost Converter with IWCI

Two-phase interleaved boost converter with IWCI consists of the same 4 different operating modes similar to the previous topologies. The KVL across phase 1 and phase 2 can be written as below.

$$\begin{aligned} V_{1,2} &= L_1 \frac{di_{in}}{dt} + 2M_1 \frac{di_{in}}{dt} + L_2 \frac{di_1}{dt} - M_2 \frac{di_2}{dt} \\ V_{1,3} &= L_1 \frac{di_{in}}{dt} + 2M_1 \frac{di_{in}}{dt} + L_2 \frac{di_2}{dt} - M_2 \frac{di_1}{dt} \end{aligned} \quad (4.43)$$

In this equation, $V_{1,2}$ is the voltage applied across the center winding and phase1 winding, $V_{1,3}$ voltage applied across the center winding phase2 winding, i_1, i_2, i_{in} are the phase1, phase2 and input currents, respectively. L_1 is self inductance of the center leg winding, L_2 self inductance of the outer leg windings, M_1 mutual inductance between the center leg winding and outer leg windings, M_2 mutual inductance between the outer leg windings. Applied voltages can be written as:

$$V_{1,2} = \begin{cases} V_{in}; & S_1 : ON \\ V_{in} - V_o; & S_1 : OFF \end{cases} \quad (4.44)$$

$$V_{1,3} = \begin{cases} V_{in}; & S_2 : ON \\ V_{in} - V_o; & S_2 : OFF \end{cases} \quad (4.45)$$

Waveforms of input and phase currents of the converter with IWCI are similar to waveforms of the converter with LCI. By using Eq. 4.43, Eq. 4.44 and Eq. 4.45 and writing KVL across the phases of the converter and solving them together inductor and input current ripple equations can be obtained for each operating mode. These equations are listed in Table 4.3.

Table 4.3: Current Ripple Equations of the Converter with IWCI in Different Converter Operating Modes

$Mode1(S_1 : ON, S_2 : OFF)$	$Mode2(S_1 : OFF, S_2 : ON)$
$\begin{aligned} \frac{di_1}{dt} &= \frac{1}{2L_1 + L_2 + 4M_1 - M_2} (V_{in} - \frac{V_o}{2}) + \frac{1}{L_2 + M_2} (\frac{V_o}{2}) \\ \frac{di_2}{dt} &= \frac{1}{2L_1 + L_2 + 4M_1 - M_2} (V_{in} - \frac{V_o}{2}) - \frac{1}{L_2 + M_2} (\frac{V_o}{2}) \\ \frac{di_{in}}{dt} &= \frac{2}{2L_1 + L_2 + 4M_1 - M_2} (V_{in} - \frac{V_o}{2}) \end{aligned} \quad (4.46)$	$\begin{aligned} \frac{di_1}{dt} &= \frac{1}{2L_1 + L_2 + 4M_1 - M_2} (V_{in} - \frac{V_o}{2}) - \frac{1}{L_2 + M_2} (\frac{V_o}{2}) \\ \frac{di_2}{dt} &= \frac{1}{2L_1 + L_2 + 4M_1 - M_2} (V_{in} - \frac{V_o}{2}) + \frac{1}{L_2 + M_2} (\frac{V_o}{2}) \\ \frac{di_{in}}{dt} &= \frac{2}{2L_1 + L_2 + 4M_1 - M_2} (V_{in} - \frac{V_o}{2}) \end{aligned} \quad (4.47)$
$Mode3(S_1 : OFF, S_2 : OFF)$	$Mode4(S_1 : ON, S_2 : ON)$
$\begin{aligned} \frac{di_1}{dt} &= \frac{di_1}{dt} = \frac{1}{2L_1 + L_2 + 4M_1 - M_2} (V_{in} - V_o) \\ \frac{di_{in}}{dt} &= \frac{2}{2L_1 + L_2 + 4M_1 - M_2} (V_{in} - V_o) \end{aligned} \quad (4.48)$	$\begin{aligned} \frac{di_1}{dt} &= \frac{di_2}{dt} = \frac{1}{2L_1 + L_2 + 4M_1 - M_2} V_{in} \\ \frac{di_{in}}{dt} &= \frac{2}{2L_1 + L_2 + 4M_1 - M_2} V_{in} \end{aligned} \quad (4.49)$

As seen in Fig. 2.6, peak to peak inductor current ripple can be written from current equation during mode1 for $D \leq 0.5$ and during mode2 for $D \geq 0.5$. Equations for peak to peak input and inductor current ripples are given in below.

$$\Delta I_{L,pp} = \begin{cases} \left[\frac{1}{2L_1 + L_2 + 4M_1 - M_2} (V_{in} - \frac{V_o}{2}) + \frac{1}{L_2 + M_2} (\frac{V_o}{2}) \right] DT_s; & D \leq 0.5 \\ \left[\frac{1}{2L_1 + L_2 + 4M_1 - M_2} (V_{in} - \frac{V_o}{2}) - \frac{1}{L_2 + M_2} (\frac{V_o}{2}) \right] (1 - D)T_s; & D \geq 0.5 \end{cases} \quad (4.50)$$

$$\Delta I_{in,pp} = \begin{cases} \left[\frac{2}{2L_1 + L_2 + 4M_1 - M_2} (V_{in} - \frac{V_o}{2}) \right] (0.5 - D)T_s; & D \leq 0.5 \\ \left[\frac{2}{2L_1 + L_2 + 4M_1 - M_2} V_{in} \right] (D - 0.5)T_s; & D \geq 0.5 \end{cases} \quad (4.51)$$

4.4 Close-Coupled Inductor (CCI)

This topology composes of two separate inductors. One of them is called a boost inductor, BI which is connected in series to an input voltage source. The other inductor is called CCI which composes of two windings connected to the phases of the interleaved boost converter. The terminal connections of these inductors are shown in Fig. 4.11.

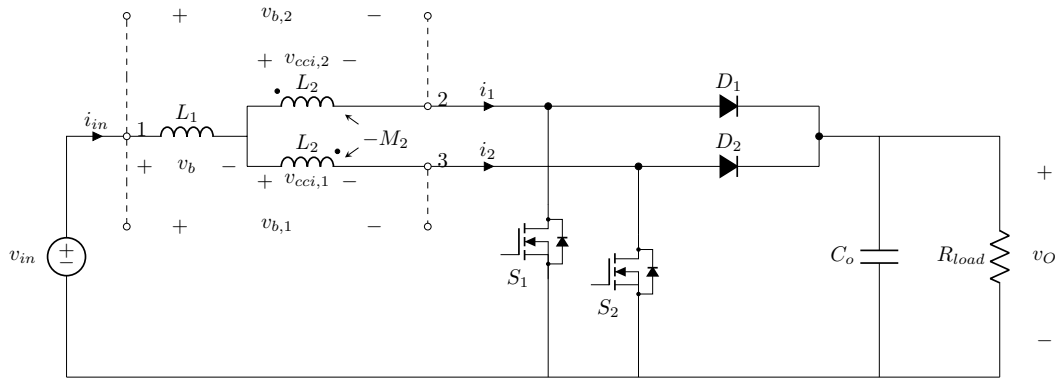


Figure 4.11: Two-phase boost converter with CCI

4.4.1 Magnetic Analysis

The magnetic core structures and magnetic circuit models of CCI and boost inductor (BI) are shown in Fig. 4.12 and Fig. 4.13, respectively. The directions of the magnetic fluxes in the core are labeled. As can be seen, the windings of CCI are inversely coupled to each other. With the help of inverse and strong coupling between the windings, there are not any DC flux components in the magnetic core.

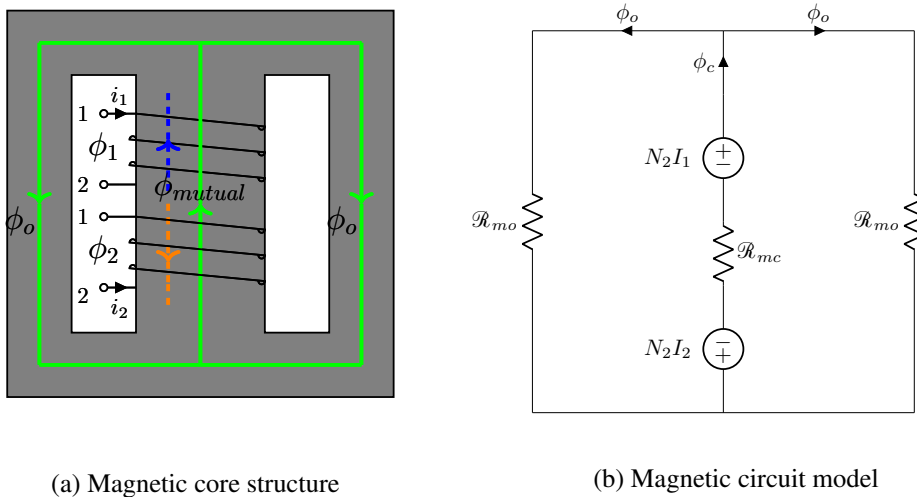
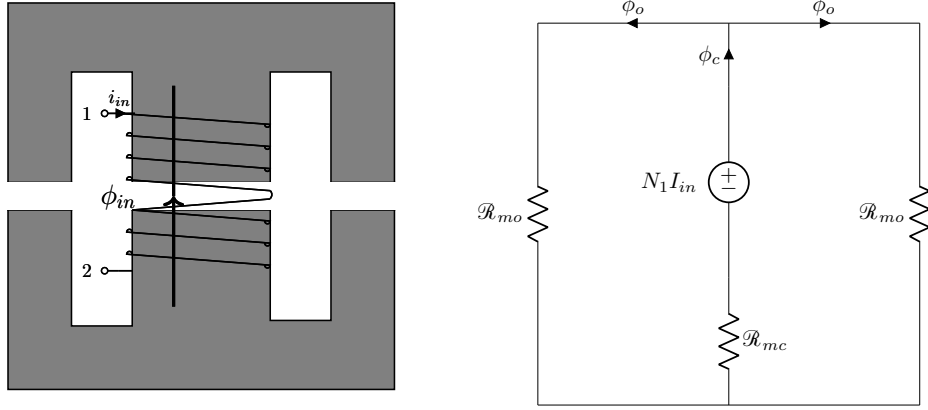


Figure 4.12: Magnetic core structure and magnetic circuit model of a CCI



(a) Magnetic core structure of the CCI-BI

(b) Magnetic circuit model of the CCI-BI

Figure 4.13: Magnetic core structure and magnetic circuit model of the CCI-BI

From the magnetic circuit model, the following equations can be obtained.

$$\begin{aligned}
 N_2 I_1 - N_2 I_2 &= \Phi_o \mathcal{R}_{mo} + \Phi_c \mathcal{R}_{mc} \\
 I_1 + I_2 &= 2I_{av} \\
 \Phi_c &= 2\Phi_o
 \end{aligned} \tag{4.52}$$

N_2 is the number of turns of the windings. The average or DC component of the magnetic fluxes of the outer legs and center leg of the CCI and BI can be written as in Eq. 4.53.

$$\begin{aligned}
 \Phi_o &= \Phi_c = 0 \\
 \Phi_b &= \frac{N_1 I_{in}}{\mathcal{R}_{mb}} \\
 \mathcal{R}_{mb} &= \frac{\mathcal{R}_{mo} + 2\mathcal{R}_{mc}}{2}
 \end{aligned} \tag{4.53}$$

The ripple values of the magnetic fluxes of the outer legs can be written as in Eq. 4.54.

$$\begin{aligned}
 V_{b,1} &= N_1 \frac{d\phi_b}{dt} + N_2 \frac{d\phi_1}{dt} \\
 V_{b,2} &= N_1 \frac{d\phi_b}{dt} + N_2 \frac{d\phi_2}{dt} \\
 \frac{d\phi_c}{dt} &= \frac{d\phi_1}{dt} - \frac{d\phi_2}{dt}
 \end{aligned} \tag{4.54}$$

The applied voltages across the boost inductor and phase 1 winding of CCI, $V_{b,1}$ and the boost inductor and phase 2 winding of CCI, $V_{b,2}$ are shown in Fig. 4.11. In order to obtain the peak to peak ripple of magnetic fluxes of CCI and CCI-BI, voltages applied to the boost inductor and windings of CCI should be calculated. These voltages are calculated by writing KVL according to the operating modes of the converter. The equations are given in below.

In mode1:

$$\begin{aligned}
 -v_{in} + v_b + v_{cci,1} &= 0 \\
 -v_{in} + v_b + v_{cci,2} + v_o &= 0 \\
 v_{cci,1} - v_{cci,2} &= v_o \\
 v_{cci,1} &= \frac{v_o}{2} \\
 v_b &= v_{in} - \frac{v_o}{2}
 \end{aligned} \tag{4.55}$$

In mode2:

$$\begin{aligned}
 -v_{in} + v_b + v_{cci,1} + v_o &= 0 \\
 -v_{in} + v_b + v_{cci,2} &= 0 \\
 v_{cci,1} - v_{cci,2} &= -v_o \\
 v_{cci,1} &= \frac{-v_o}{2} \\
 v_b &= \frac{v_{in} - v_o}{2}
 \end{aligned} \tag{4.56}$$

In mode3:

$$\begin{aligned}
 -v_{in} + v_b + v_{cci,1} + v_o &= 0 \\
 -v_{in} + v_b + v_{cci,2} + v_o &= 0 \\
 v_{cci,1} - v_{cci,2} &= 0 \\
 v_{cci,1} &= 0 \\
 v_b &= v_{in} - v_o
 \end{aligned} \tag{4.57}$$

In mode4:

$$\begin{aligned}
-v_{in} + v_b + v_{cci,1} &= 0 \\
-v_{in} + v_b + v_{cci,2} &= 0 \\
v_{cci,1} - v_{cci,2} &= 0 \\
v_{cci,1} &= 0 \\
v_b &= v_{in}
\end{aligned} \tag{4.58}$$

In these equations, v_{in} is the input voltage of the converter, v_o output voltage, v_b voltage across the boost inductor, $v_{cci,1}$ voltage across to phase1 winding of CCI, $v_{cci,2}$ voltage across to phase2 winding of CCI. Peak to peak ripple of the magnetic fluxes of the boost inductor and the center leg magnetic fluxes of the CCI can be calculated by using the voltages calculated in the above equations. The ripple values calculated separately for $D < 0.5$ and $D > 0.5$ operating conditions. By subtracting equations given in Eq. 4.54, peak to peak ripple of the center leg magnetic fluxes of the CCI can be found. For $D < 0.5$, mode1 and for $D > 0.5$, mode2 are used for applied voltages. The equations of AC component or peak to peak ripple of the magnetic fluxes of the center leg of the CCI are given in Eq. 4.59. The magnetic fluxes of the outer legs are equal to half of the center leg magnetic flux.

$$\phi_{c,pp} = \begin{cases} \frac{V_{in}}{(2N_2)(1-D)}DT_s; & D \leq 0.5 \\ \frac{V_{in}}{2N_2}T_s; & D \geq 0.5 \end{cases} \tag{4.59}$$

A similar analysis can be applied to the boost inductor to find the AC ripple of magnetic flux in the core of the boost inductor. For $D < 0.5$, mode1 and for $D > 0.5$, mode4 are used for applied voltages. The equations of AC component or peak to peak ripple of the magnetic flux of the boost inductor are given in Eq. 4.60.

$$\phi_{b,pp} = \begin{cases} \frac{V_{in}(1-2D)}{2N_1(1-D)}DT_s; & D \leq 0.5 \\ \frac{V_{in}}{N_1}(D-0.5)T_s; & D \geq 0.5 \end{cases} \tag{4.60}$$

The maximum values of the magnetic fluxes in each leg can be written as a sum of the DC component and half of the AC component of the magnetic fluxes as shown in Fig. 4.14. The maximum values of the magnetic flux of the CCI and BI can be

obtained by using Eq. 4.53, Eq. 4.59 and Eq. 4.60. The equations for the maximum values of the magnetic fluxes of the outer leg and center leg are given in Eq. 4.61 and Eq. 4.62, respectively.

$$\phi_{c,max} = \begin{cases} \frac{V_{in}}{(4N_2)(1-D)}DT_s; & D \leq 0.5 \\ \frac{V_{in}}{4N_2}T_s; & D \geq 0.5 \end{cases} \quad (4.61)$$

$$\phi_{b,max} = \begin{cases} \frac{N_1I_{in}}{R_{mb}} + \frac{V_{in}(1-2D)}{4N_1(1-D)}DT_s; & D \leq 0.5 \\ \frac{N_1I_{in}}{R_{mb}} + \frac{V_{in}}{2N_1}(D-0.5)T_s; & D \geq 0.5 \end{cases} \quad (4.62)$$

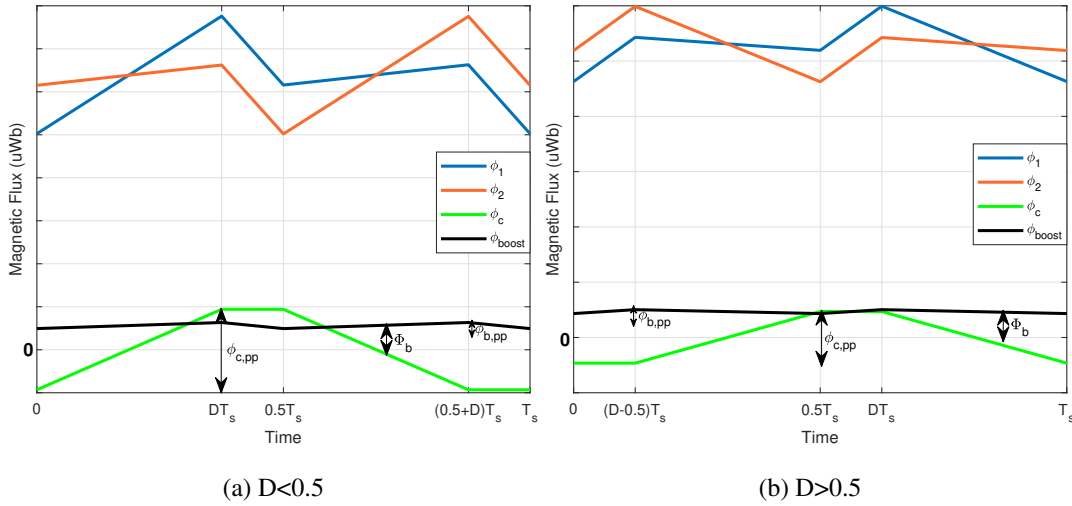


Figure 4.14: Waveforms of the magnetic fluxes in the CCI and BI core

4.4.2 Electrical Analysis of the Interleaved Boost Converter with CCI

Similar to the previous converters, a two-phase interleaved boost converter with CCI consists of the same 4 different operating modes. The KVL across phase 1 and phase 2 can be written as below.

$$\begin{aligned}
V_{b,1} &= L_1 \frac{di_{in}}{dt} + L_2 \frac{di_1}{dt} - M_2 \frac{di_2}{dt} \\
V_{b,2} &= L_1 \frac{di_{in}}{dt} + L_2 \frac{di_2}{dt} - M_2 \frac{di_1}{dt}
\end{aligned} \tag{4.63}$$

$V_{b,1}$ is the voltage applied across the boost inductor and phase1 winding of CCI, $V_{b,2}$ is the voltage applied across the boost inductor and phase2 winding of CCI, L_1 self-inductance of the boost, L_2 self-inductance of the windings of the CCI, M_2 mutual inductance between the windings of the CCI. Applied voltages can be expressed as:

$$V_{b,1} = \begin{cases} V_{in}; & S_1 : ON \\ V_{in} - V_o; & S_1 : OFF \end{cases} \tag{4.64}$$

$$V_{b,2} = \begin{cases} V_{in}; & S_2 : ON \\ V_{in} - V_o; & S_2 : OFF \end{cases} \tag{4.65}$$

Waveforms of input and phase currents of the converter with CCI are similar to the waveforms of converter with LCI and IWCI which are given in Fig. 2.6. By using Eq. 4.63, Eq. 4.64 and Eq. 4.65 and writing KVL across the phases of the converter and solving them together inductor and input current ripple equations can be obtained for each operating mode. These equations are listed in Table 4.4.

Table 4.4: Current Ripple Equations of the Converter with CCI in Different Converter Operating Modes

$Mode1(S_1 : ON, S_2 : OFF)$	$Mode2(S_1 : OFF, S_2 : ON)$
$ \begin{aligned} \frac{di_1}{dt} &= \frac{1}{2L_1 + L_2 - M_2} (V_{in} - \frac{V_o}{2}) + \frac{1}{L_2 + M_2} (\frac{V_o}{2}) \\ \frac{di_2}{dt} &= \frac{1}{2L_1 + L_2 - M_2} (V_{in} - \frac{V_o}{2}) - \frac{1}{L_2 + M_2} (\frac{V_o}{2}) \\ \frac{di_{in}}{dt} &= \frac{2}{2L_1 + L_2 - M_2} (V_{in} - \frac{V_o}{2}) \end{aligned} \tag{4.66} $	$ \begin{aligned} \frac{di_1}{dt} &= \frac{1}{2L_1 + L_2 - M_2} (V_{in} - \frac{V_o}{2}) - \frac{1}{L_2 + M_2} (\frac{V_o}{2}) \\ \frac{di_2}{dt} &= \frac{1}{2L_1 + L_2 - M_2} (V_{in} - \frac{V_o}{2}) + \frac{1}{L_2 + M_2} (\frac{V_o}{2}) \\ \frac{di_{in}}{dt} &= \frac{2}{2L_1 + L_2 - M_2} (V_{in} - \frac{V_o}{2}) \end{aligned} \tag{4.67} $
$Mode3(S_1 : OFF, S_2 : OFF)$	$Mode4(S_1 : ON, S_2 : ON)$
$ \begin{aligned} \frac{di_1}{dt} &= \frac{di_2}{dt} = \frac{1}{2L_1 + L_2 - M_2} (V_{in} - V_o) \\ \frac{di_{in}}{dt} &= \frac{2}{2L_1 + L_2 - M_2} (V_{in} - V_o) \end{aligned} \tag{4.68} $	$ \begin{aligned} \frac{di_1}{dt} &= \frac{di_2}{dt} = \frac{1}{2L_1 + L_2 - M_2} V_{in} \\ \frac{di_{in}}{dt} &= \frac{2}{2L_1 + L_2 - M_2} V_{in} \end{aligned} \tag{4.69} $

Peak to peak inductor current ripple can be written from current equation during mode1 for $D \leq 0.5$ and during mode2 for $D \geq 0.5$. Equations for the peak to peak input and inductor current ripples are given in below.

$$\Delta I_{L,pp} = \begin{cases} \left[\frac{1}{2L_1 + L_2 - M_2} (V_{in} - \frac{V_o}{2}) + \frac{1}{L_2 + M_2} (\frac{V_o}{2}) \right] DT_s; & D \leq 0.5 \\ \left[\frac{1}{2L_1 + L_2 - M_2} (V_{in} - \frac{V_o}{2}) - \frac{1}{L_2 + M_2} (\frac{V_o}{2}) \right] (1 - D)T_s; & D \geq 0.5 \end{cases} \quad (4.70)$$

$$\Delta I_{in,pp} = \begin{cases} \left[\frac{2}{2L_1 + L_2 - M_2} (V_{in} - \frac{V_o}{2}) \right] (0.5 - D)T_s; & D \leq 0.5 \\ \left[\frac{2}{2L_1 + L_2 - M_2} V_{in} \right] (D - 0.5)T_s; & D \geq 0.5 \end{cases} \quad (4.71)$$

4.5 Chapter Summary

In this chapter, two-phase interleaved boost converters with DI, LCI, IWCI and CCI topologies are analyzed and their electrical and magnetic equations are derived. These formulas will be used in the next chapter when designing the inductors.

CHAPTER 5

DESIGN OF INDUCTORS

The most common 2-phase coupled inductor topologies are mathematically analyzed in the previous chapter. Their critical current ripple and magnetic flux density formulas are derived. In this chapter, these formulas are used to design the inductors. Inductors are designed under the condition where all converters have the same input current ripple and output voltage ripple. The selection of this design condition is explained. Design methodologies for each inductor type are proposed. Finite element analysis (FEA) simulations are performed and used to update the design parameters by considering non-linearities such as fringing fluxes in the air-gap. Moreover, the selection of coupled inductor parameters is explained by considering the effect of these parameters on inductor performance.

5.1 Design Considerations

As stated in Chapter 2, the input current ripple of the converter is an important parameter, especially in fuel-cell electric vehicle applications. It can affect the input filter size in PFC applications. Moreover, to keep the filter size the same for all designs, input current ripple is kept constant for all converters with various inductor topologies. The other performance parameter that is kept the same for all designs is the output voltage ripple. The most dominant part of the output voltage ripple of a boost converter is the ripple caused due to the ESR of the output capacitor. The current of output capacitor of a boost converter has a large ripple. Peak to peak ripple of the output capacitor current equals peak inductor current. Therefore, by keeping the inductor current ripple constant, it is achieved that all converters have the same output voltage

ripple except the converter with discrete inductors. It is not possible to obtain both the input current ripple and inductor current ripple at desired values for the converter with discrete inductors. Thus, this converter is designed to have the same input current ripple as other converters employed with coupled inductors. Design parameters of the converters are summarized in Table 5.1.

Table 5.1: Converter Parameters

Input Voltage	Output Voltage	Output Power
150V-250V	400V	2kW
Switching Frequency	Input Current Ripple	Inductor Current Ripple
50kHz	15%	25%

The magnitude of the peak to peak input and inductor current ripple are calculated at maximum output power and minimum input voltage condition. The magnitude of input and inductor current ripples are given in the Eq. 5.1 and Eq. 5.2, respectively.

$$\Delta I_{in,pp} = \frac{P_{out,max}}{V_{in,min}} \cdot 15\% \quad (5.1)$$

$$\Delta I_{in,pp} = 2A$$

$$\Delta I_{L,pp} = \frac{P_{out,max}}{2V_{in,min}} \cdot 25\% \quad (5.2)$$

$$\Delta I_{L,pp} = 1.7A$$

5.2 Discrete Inductors

As stated before, discrete inductors are designed to have the same input current ripple as the other inductor types. However, while input current ripples the same, inductor current ripple of discrete inductors is higher than the others. This results in slightly higher output voltage ripple and higher power losses due to the increase in RMS value of the current of the phases. Inductor current ripple and input current ripple can not be adjusted to the desired values at the same time by using DIs.

5.2.1 Design Methodology

A design methodology given in Fig. 5.1 is proposed. DIs are designed by following this methodology.

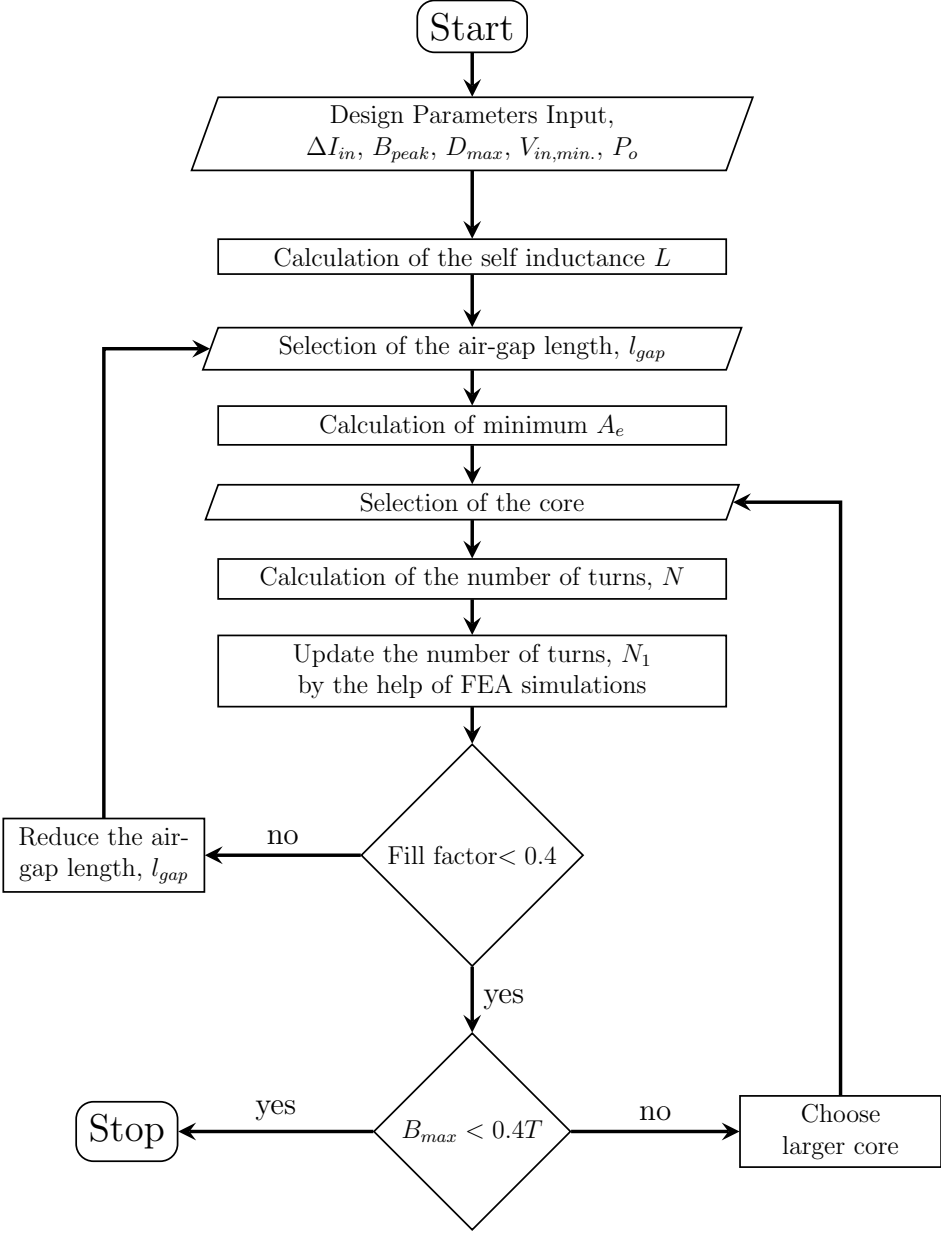


Figure 5.1: DI design flowchart

Step 1: Calculation of inductance, L

By using the input current ripple equation Eq. 4.14 the required inductance of discrete

inductors, L can be calculated as:

$$\frac{2 \cdot 150(0.625 - 0.5)}{L} \cdot 20 \cdot 10^{-6} = 2 \quad (5.3)$$

$$L = 375 \cdot 10^{-6} \mu H$$

Step 2: Selection of the air-gap length, l_{gap}

In this step, the air-gap length which is applied to the inductor is chosen. It is selected as 1.7mm. Selecting air-gap length smaller results in a larger magnetic core. While selecting larger air-gap length results in a higher number of turns which will increase both copper loss and fill factor.

Step 3: Calculation of minimum cross-section area, A_e

Minimum cross-section area, A_e is calculated from B_{peak} limit. By using Eq. 4.5, peak magnetic flux density of the discrete inductors can be written as:

$$B_{peak} = \frac{\frac{NI_{av}}{\mathcal{R}_{mx}} + \frac{V_{in}DT_s}{2N}}{A_e} \quad (5.4)$$

where,

$$\mathcal{R}_{mx} = 0.5\mathcal{R}_{mo} + \mathcal{R}_{mc}$$

$$\mathcal{R}_{mx} = \frac{2l_{gap}}{\mu_0 A_e} \quad (5.5)$$

$$N = \sqrt{\mathcal{R}_{mx} L}$$

Substituting Eq. 5.5 into the Eq. 5.4 yields,

$$A_e = \left[\frac{LI_{av} + 0.5V_{in}DT_s}{B_{peak} \sqrt{\frac{2l_{gap}L}{\mu_0}}} \right]^2 \quad (5.6)$$

The fringing effect has not been taken into account yet. So, for a ferrite core with 0.4T saturation magnetic flux density value limiting B_{peak} to 0.25T is a good design input for A_e calculation to select a core. Solving Eq. 5.6 for 0.25T B_{peak} gives the minimum A_e value as $186mm^2$. Based on this volume, ETD49/25/16 core with N87 material [37] which has A_e of $211mm^2$ from TDK is selected.

Step 4: Calculation of the number of turns, N

After the selection of the magnetic core, the number of turns can be calculated by using Eq. 5.7.

$$L = \frac{N^2}{0.5\mathcal{R}_{mo} + \mathcal{R}_{mc}} \quad (5.7)$$

The reluctances are calculated as:

$$\begin{aligned} \mathcal{R}_{mc} &= \frac{l_c - l_{gap}}{\mu_r \mu_0 A_e} + \frac{l_{gap}}{\mu_0 A_e} = 6.52 \frac{A}{uWb} \\ \mathcal{R}_{mo} &= \frac{l_o - l_{gap}}{\mu_r \mu_0 A_e / 2} + \frac{l_{gap}}{\mu_0 A_e / 2} = 12.58 \frac{A}{uWb} \end{aligned} \quad (5.8)$$

Substituting Eq. 5.8 into the Eq. 5.7 gives the number of turns, N equals 69 is determined.

Step 5: FEA analysis and update the number of turns, N

In this step, the number of turns is updated according to new reluctance values. The reluctances are calculated from FEA results. The reluctances \mathcal{R}_{mo} and \mathcal{R}_{mc} can be calculated by using the following formula.

$$\begin{aligned} \lambda &= N\phi \\ \phi_{dc} &= \frac{2NI_{av}}{\mathcal{R}_{mo} + 2\mathcal{R}_{mc}} \\ \mathcal{R}_{mo} &= 2\mathcal{R}_{mc} \end{aligned} \quad (5.9)$$

From FEA simulations, average value of λ is found as 0.0044 Weber. Substituting this value into Eq. 5.9, the reluctances can be found as:

$$\begin{aligned} \mathcal{R}_{mo} &= 7.05 \frac{A}{\mu\text{Weber}} \\ \mathcal{R}_{mc} &= 3.52 \frac{A}{\mu\text{Weber}} \end{aligned} \quad (5.10)$$

The new value of the number of turns can be calculated by substituting reluctance results into the Eq. 5.7 which yields the number of turns, N as 52. Details of the FEA simulations are also given in the following subsection.

Step 6: Checking fill factor, k_{cu}

After calculation of the number of turns it can be checked whether this number of turns exceeds the fill factor limit. Total conductor area and fill factor can be calculated

by using the following formula.

$$\begin{aligned}
 A_{conductor,total} &= n \cdot N \cdot A_{wire} \\
 A_{wire} &= \pi r^2 \\
 k_{cu} &= \frac{A_{conductor,total}}{A_{winding}}
 \end{aligned}
 \tag{5.11}$$

n is the number of parallel layers, N number of turns, A_{wire} area of the wire, r radius of the wire, $A_{conductor,total}$ total area of the winding, $A_{winding}$ total winding area of the core, k_{cu} fill factor. Wire thickness is determined by the average inductor current. In the current design, A_{wire} is determined by choosing AWG22 wire with a diameter of 0.65 mm.

For round-type conductors, as a rule of thumb 0.4 is a limited value for the fill factor. If the fill factor is higher than the limit value at this step, a smaller air-gap can be selected by returning to the 2nd step, since a smaller air gap will result in a less number of turns.

Step 7: Checking B_{peak}

In the final step of the design procedure, after updating the number of turns, B_{peak} should be checked whether it is less than the saturation level of the magnetic core. It can also be calculated by using the reluctance values calculated in FEA simulations and Eq. 5.4. FEA results show that maximum value of the magnetic flux density of the core reaches 0.332 Tesla which is below the saturation level. Here the right core is selected in the first iteration. This step finalizes the design procedure. If the resultant flux density was higher than the limit, a bigger core, if much lower than the limit a smaller core should be selected and the other design steps should be followed.

5.2.2 Finite Element Analysis (FEA) Simulations

FEA simulations are performed by using Ansys Maxwell 3D. The model of the DIs in FEA simulations is shown in Fig. 5.3. The winding of the inductor is modeled as a stranded conductor and this winding is excited by using the phase current waveform of the converter with DIs that is taken from the circuit simulations. The 3D model is simulated by using a transient solver. FEA result of the magnetic flux density along

the center leg of the core is given in Fig. 5.2. The magnitude of the magnetic flux density plot on the magnetic core at the time when the current of the winding is at its maximum value is given in Fig. 5.3.

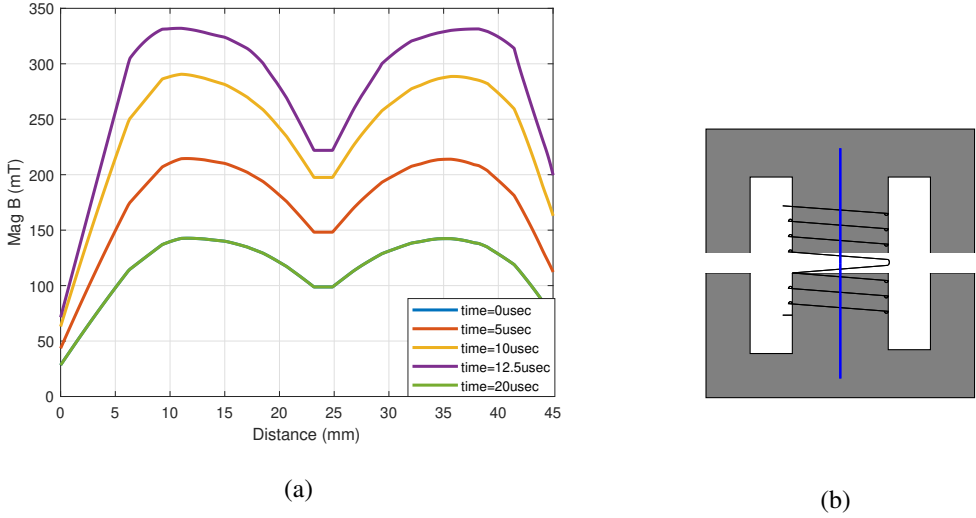


Figure 5.2: FEA result of the magnitude of the magnetic flux density along the line shown in b) on the center leg of DI

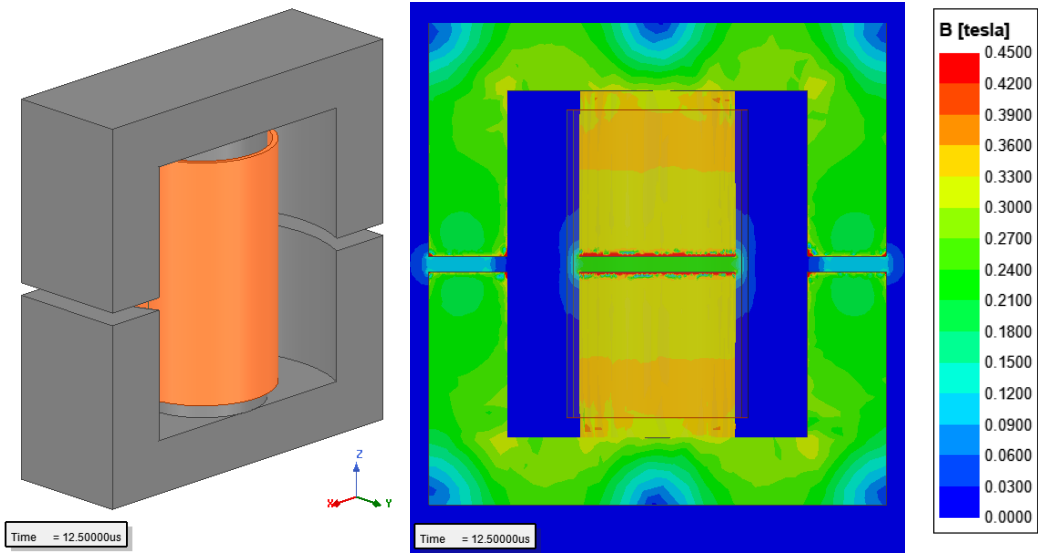


Figure 5.3: 3D model of DI in FEA and magnitude of magnetic flux density of the core along the cross-section of x-z plane

5.3 Loosely-Coupled Inductor

The formulas derived in Section 4.2.2 and Section 4.2.1 are used to design the LCI. Outer leg magnetic flux density is considered during the design procedure since it is always greater than the center leg magnetic flux density. Moreover, it can also be observed that, as can be seen in Fig. 5.4 the magnetic flux density increases concerning duty cycle thus, the operating point is selected as maximum power and minimum input voltage.

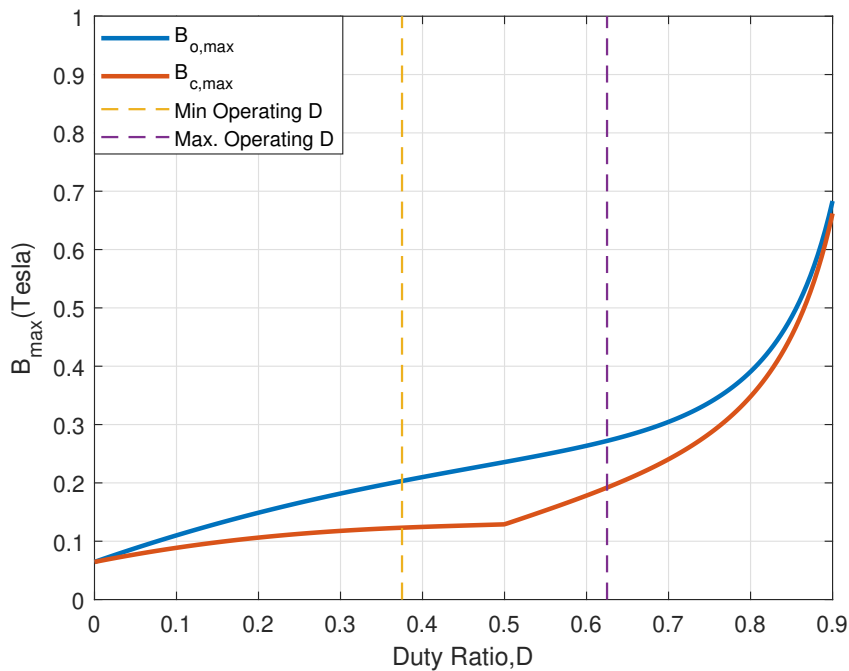


Figure 5.4: Magnetic flux density of the outer leg and center leg of the LCI vs duty cycle for a selected core and coupling coefficient, $\alpha : 0.8$

5.3.1 Design Methodology

A design methodology given in Fig. 5.5 is proposed and LCI is designed by following this methodology. The design steps following the initialization are explained in the following text.

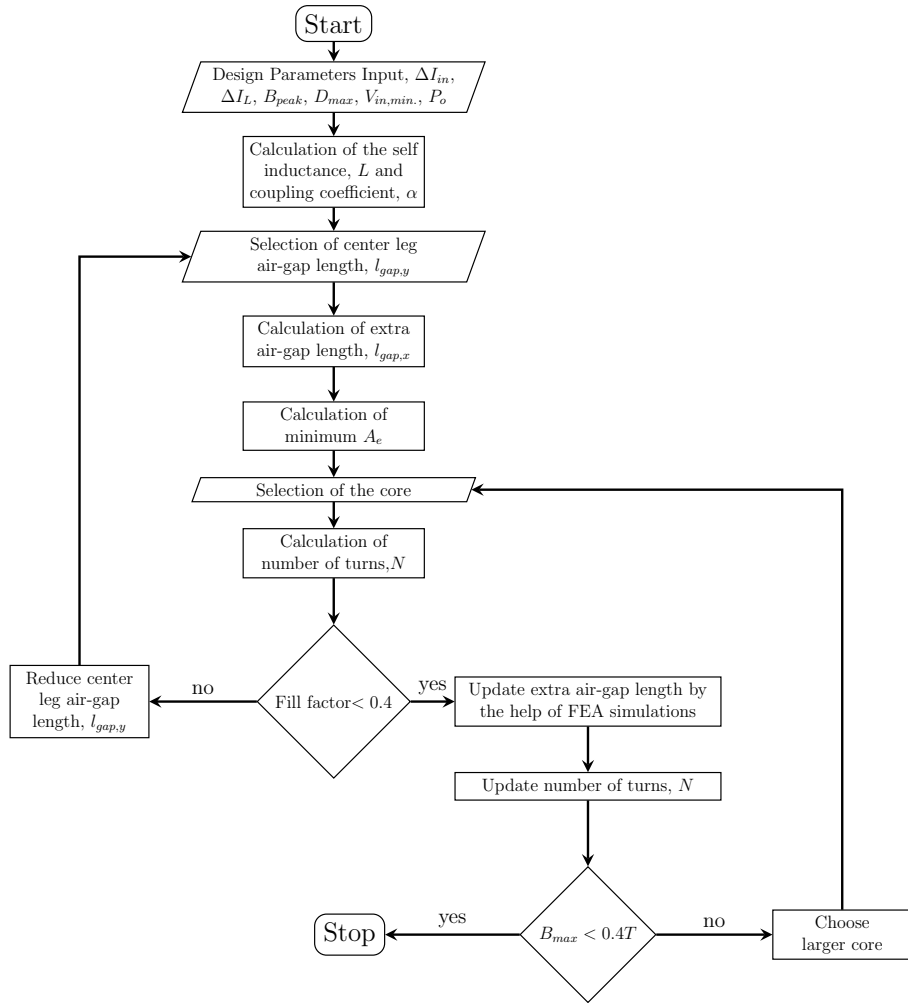


Figure 5.5: LCI design flowchart

Step 1: Calculation of coupling coefficient and self inductance

By using the inductor current ripple equation Eq. 4.32 and input current ripple equation Eq. 4.33, the required self inductance of the LCI and coupling coefficient of the LCI can be calculated as:

$$\Delta I_{in,pp} = \frac{2}{L - M} V_{in} (D - 0.5) T_s \quad (5.12)$$

$$M = \alpha L$$

$$\frac{2}{(1-\alpha)L} \cdot 150 \cdot 0.125 \cdot 20 \cdot 10^{-6} = 2 \quad (5.13)$$

$$(1-\alpha)L = 375 \cdot 10^{-6}$$

$$\Delta I_{L,pp} = \left[\frac{1}{L-M} \left(V_{in} - \frac{V_o}{2} \right) - \frac{1}{L+M} \left(\frac{V_o}{2} \right) \right] (1-D) T_s$$

$$\left(-\frac{50}{(1-\alpha)L} - \frac{200}{(1+\alpha)L} \right) \cdot 0.375 \cdot 20 \cdot 10^{-6} = -1.7 \quad (5.14)$$

$$(1+\alpha)L = 2142.85 \cdot 10^{-6}$$

Solving equations together yields:

$$\alpha = 0.7 \quad (5.15)$$

$$L = 1250 \mu H$$

As can be seen, once the input and output ripple values are fixed there is unique inductance and coupling coefficient for an assumed operating point.

Step 2: Selection of the gap on the center leg, $l_{gap,y}$

In commercial gapped E-E cores, mostly available total air-gap lengths on the center leg are 1mm, 2mm, 3mm and 4mm. For a custom-designed core, the gap on the center leg can be increased. But selecting of a large air-gap on the center leg results in an increase in the number of turns required to obtain desired inductance values. That comes at a cost of inductor winding loss, moreover, that may exceed the limit of the fill factor of the core. On the other hand, a smaller air-gap length results in higher magnetic flux density value. Therefore, for the initial design point, E-E core with 4mm air-gap length on the center leg is selected.

Step 3: Calculation of extra air-gap applied on all legs, $l_{gap,x}$

In this step, in order to obtain desired coupling coefficient, the extra air-gaps are added on all legs of the magnetic core is calculated. In Fig. 5.6, this extra air-gap length is denoted as $l_{gap,x}$ while air-gap on the center leg only which comes with magnetic core denoted as $l_{gap,y}$.

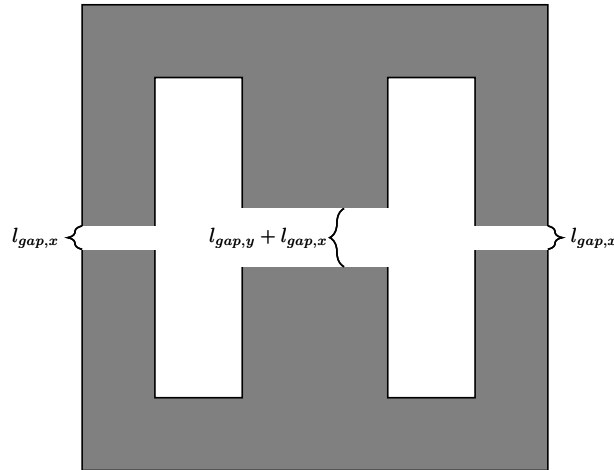


Figure 5.6: Definitions of the air-gaps

The coupling coefficient can be as follows by neglecting the reluctance of the core since it is far smaller than the reluctance of air-gaps.

$$\alpha = \frac{\mathcal{R}_{mc}}{\mathcal{R}_{mc} + \mathcal{R}_{mo}}$$

$$\alpha = \frac{\frac{l_{gap,x} + l_{gap,y}}{\mu_0 \dot{A}_e}}{\frac{l_{gap,x} + l_{gap,y}}{\mu_0 \dot{A}_e} + \frac{l_{gap,x}}{\mu_0 \dot{A}_e/2}} \quad (5.16)$$

The solution of Eq. 5.16 is $l_{gap,x} = 1mm$. Note that, in this calculation, the effect of fringing flux is not considered. It will be taken into account in the later steps.

Step 4: Calculation of minimum cross-section area, A_e

As can be seen from Eq. 4.22, Eq. 4.23 and Fig. 5.10, peak magnetic flux density of outer legs always greater than the peak magnetic flux of center leg. Therefore, unlike conventional inductor design methods, to avoid saturation outer leg's peak magnetic flux density should be considered. By using Eq. 4.22, the peak magnetic flux density

of the outer legs of LCI can be written as:

$$B_{peak,o} = \frac{NI_{av}}{\mathcal{R}_{mo} + 2\mathcal{R}_{mc}} + \frac{1}{2} \frac{V_{in}DT_s}{N A_e/2} \quad (5.17)$$

$$B_{peak,o} = \frac{2N^2 I_{av} + (\mathcal{R}_{mo} + 2\mathcal{R}_{mc})V_{in}DT_s}{NA_e(\mathcal{R}_{mo} + 2\mathcal{R}_{mc})}$$

where,

$$\mathcal{R}_{mo} + 2\mathcal{R}_{mc} = \frac{1 + \alpha}{1 - \alpha} \mathcal{R}_{mo}$$

$$N^2 = \frac{L(\mathcal{R}_{mo}^2 + 2\mathcal{R}_{mo}\mathcal{R}_{mc})}{\mathcal{R}_{mo} + \mathcal{R}_{mc}} \quad (5.18)$$

$$N^2 = \mathcal{R}_{mo}(1 + \alpha)L$$

$$\mathcal{R}_{mo} = \frac{2l_{gap,x}}{\mu_0 A_e}$$

Substituting Eq. 5.18 into the Eq. 5.17 yields,

$$A_e = \left[\frac{2LI_{av}(1 - \alpha) + V_{in}DT_s}{B_{peak,o} \sqrt{\frac{L(1 + \alpha)l_{gap,x}}{\mu_0}}} \right]^2 \quad (5.19)$$

As mentioned before, the fringing effect has not been taken into account yet. So, for a ferrite core with 0.4T saturation magnetic flux density value limiting B_{peak} to 0.3T is a good design input for A_e calculation to select a core. Solving Eq. 5.19 for 0.3T, B_{peak} gives the minimum A_e equal to $316.7mm^2$. Based on this volume, magnetic core E55/28/21 with N87 material [38] which has A_e of $347mm^2$ from TDK is selected.

Step 5: Calculation of the number of turns, N

After selection of the magnetic core, the number of turns can be calculated by using the equation following equation.

$$L = N^2 \frac{\mathcal{R}_{mo} + \mathcal{R}_{mc}}{\mathcal{R}_{mo}^2 + 2\mathcal{R}_{mo}\mathcal{R}_{mc}} \quad (5.20)$$

The reluctances are calculated as:

$$\mathcal{R}_{mc} = \frac{l_c - l_{gap,x} - l_{gap,y}}{\mu_r \mu_0 A_e} + \frac{l_{gap,x} + l_{gap,y}}{\mu_0 A_e} = 11.50 \frac{A}{uWb} \quad (5.21)$$

$$\mathcal{R}_{mo} = \frac{l_o - l_{gap,x}}{\mu_r \mu_0 A_e/2} + \frac{l_{gap,x}}{\mu_0 A_e/2} = 4.81 \frac{A}{uWb}$$

Substituting Eq. 5.15 and Eq. 5.21 into the Eq. 5.20 gives the number of turns N equals 102 is determined.

Step 6: Checking fill factor, k_{cu}

After calculation of the number of turns, it can be checked whether this number of turns exceeds the fill factor limit. Fill factor can be calculated by using the Eq. 5.11. Similar to DIs, AWG22 wire is taken for the determination of A_{wire} . If the fill factor is higher than the limit value, 0.4, at this step, a smaller air gap can be selected by returning to the 2nd step. A smaller air gap will result in a smaller number of turns.

Step 7: Update $l_{gap,x}$ by using FEA simulations

Magnetic reluctances vary considerably in cores with high air gaps, such as coupled inductors, due to fringing fluxes. This results in a different coupling coefficient, inductance and maximum magnetic flux density values than expected. There are studies proposing analytical methods for estimating the fringing flux effect on reluctance values [39],[40]. However, FEA results are found to be more accurate after the pre-evaluations. The FEA model is provided in the following subsection. The comparison between FEA results and analytical methods is given in the next chapter. By using FEA simulations, the value of the air-gap added to all legs is updated, which will bring the coupling coefficient to the set value of 0.7. As seen from Fig. 5.7, coupling coefficient, α equals 0.7 when $l_{gap,x}$ equals 0.3mm. Then, reluctances are re-calculated with the new air-gap length.

Step 8: Update Number of Turns, N

In this step, the number of turns is updated according to new reluctance values. The reluctances are calculated by using the FEA simulations. The reluctances \mathcal{R}_{mo} and \mathcal{R}_{mc} can be calculated by using the following formula.

$$\begin{aligned} \lambda &= N\phi \\ \phi_{dc} &= \frac{NI_{av}}{\mathcal{R}_{mo} + 2\mathcal{R}_{mc}} \\ \alpha &= \frac{\mathcal{R}_{mc}}{\mathcal{R}_{mo} + \mathcal{R}_{mc}} \end{aligned} \quad (5.22)$$

From FEA simulations average value of λ is found as 0.0025 Weber. α is found as

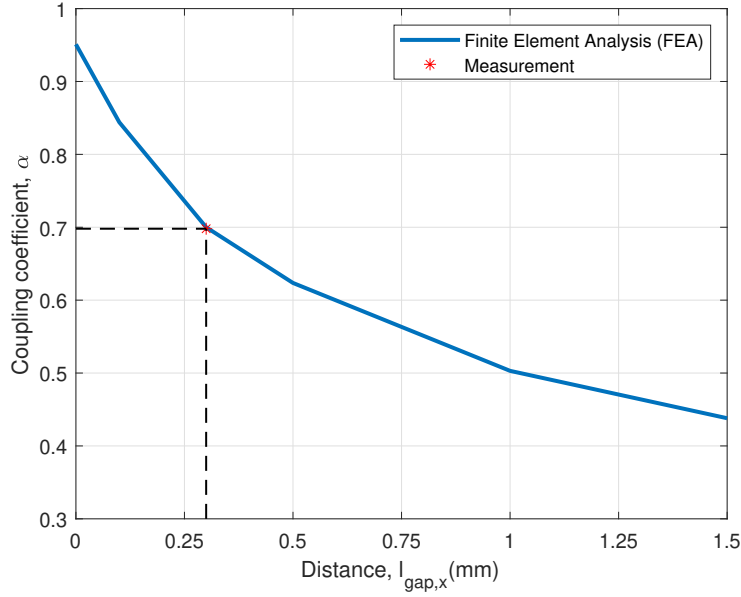


Figure 5.7: Coupling coefficient as a function of the extra air-gap distance, $l_{gap,x}$ of LCI

0.7. Substituting these values into the Eq. 5.22, the reluctances can be found as:

$$\begin{aligned} \mathcal{R}_{mo} &= 1.371 \frac{A}{\mu\text{Weber}} \\ \mathcal{R}_{mc} &= 3.1987 \frac{A}{\mu\text{Weber}} \end{aligned} \quad (5.23)$$

The new value of number of turns can be calculated by substituting reluctance results into the Eq. 5.20. The new value of number of turns, N is found as 54.

Step 9: Checking B_{peak}

After the consideration of the fringing effect, reluctances are now smaller which results in less the number of turns. As the number of turns decreases B_{peak} increases. Therefore, before the finalization of the inductor design, B_{peak} should be checked. Note that, in the design input stage B_{peak} is limited to 0.3T in order to have enough margin after the fringing effect. It can also be calculated by using the reluctance values calculated in FEA simulations and Eq. 5.17. FEA results show that the maximum value of magnetic flux density of the core reaches 0.352T which is below the saturation level. This concludes the design procedure. If the core flux density was above 0.4T, the design process will go to the core selection step to update the core with a

bigger one and the algorithm goes from there on.

5.3.2 Finite Element Analysis (FEA) Simulations

FEA simulations are performed by using ANSYS Maxwell 3D. The model of the LCI in FEA simulations is shown in Fig. 5.9. The windings of the LCI are modeled as a stranded conductor and these winding are excited by using the phase current waveforms of the converter with LCI taken from the circuit simulations. The 3D model is simulated by using a transient solver. FEA result of the magnetic flux density along the outer leg of the core is given in Fig. 5.8. The magnitude of the magnetic flux density plot on the magnetic core at the time when the current of the one winding is at its maximum value is given in Fig. 5.9.

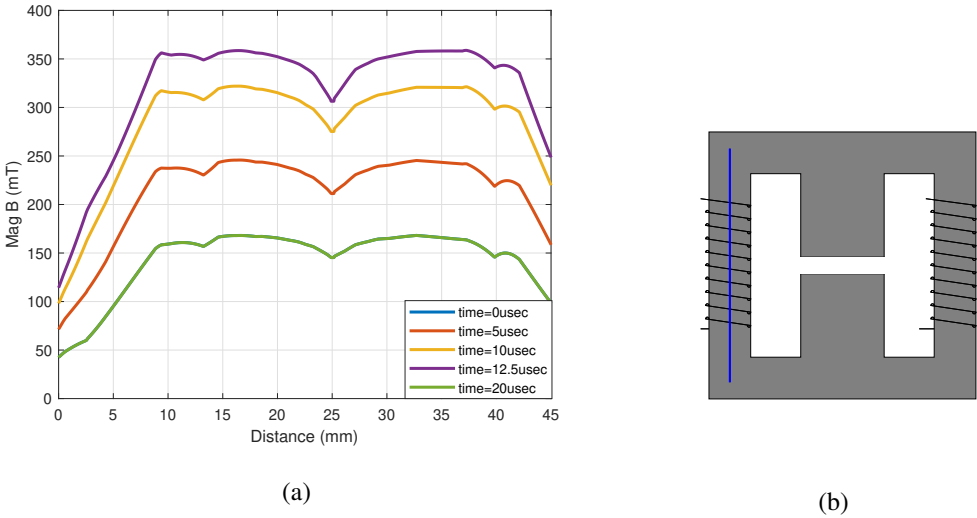


Figure 5.8: FEA result of the magnitude of the magnetic flux density along the line shown in b) on the outer leg legs of the LCI

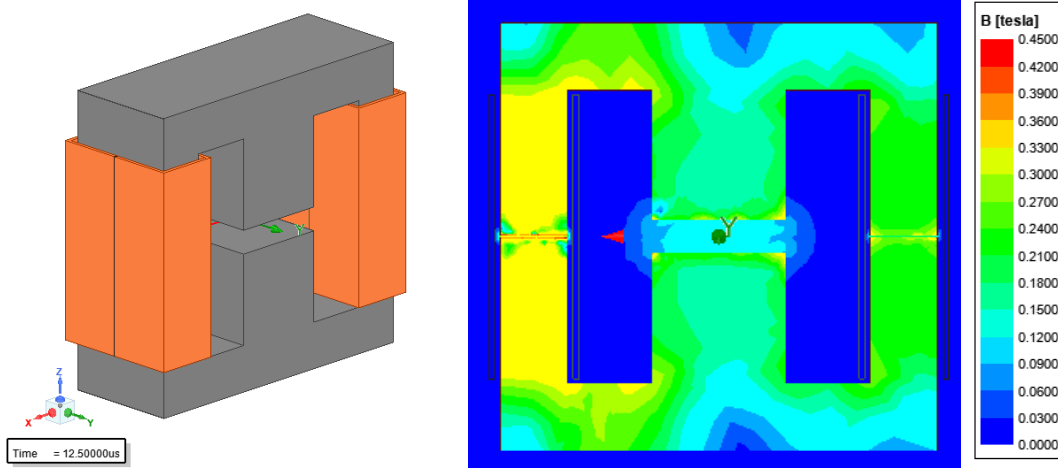


Figure 5.9: 3D model of the LCI in FEA and magnitude of the magnetic flux density of the core along the cross-section of x-z plane

5.3.3 Effect of Coupling Coefficient on Inductor Parameters

As seen from Eq. 5.13, to obtain desired input current ripple, the self-inductance of the windings of LCI can take different values as a function of the coupling coefficient. The ratio between the input current ripple and inductor current ripple is also determined by the coupling coefficient. The effect of the coupling coefficient on the LCI design is investigated. During this investigation, a magnetic core from TDK E55/28/21 with N87 material [38] is selected. First of all, the relationship between the outer leg magnetic flux density, center leg magnetic flux density and coupling coefficient is examined. The peak magnetic flux equations calculated in Chapter 4 are used. The ratio of the outer leg peak magnetic flux density to the center leg peak magnetic flux density of the LCI as a function of the duty cycle for different coupling coefficients is given in Fig. 5.10. As well known, in a traditional uncoupled inductors center leg magnetic flux density equals to outer leg magnetic flux density. However, as seen from Fig. 5.10, the outer leg magnetic flux density of the LCI is always greater than the center leg magnetic flux density. The ratio between the $B_{c,max}$ and $B_{o,max}$ decreases as coupling between the windings increases. It is expected because an increase in coupling means less flux going through the center leg of the magnetic core. When the effect of the duty cycle on the ratio of magnetic flux densities are con-

sidered, it is observed that when $D = 0.5$ the ratio equals to minimum value and it increases for other duty cycle value than the 0.5.

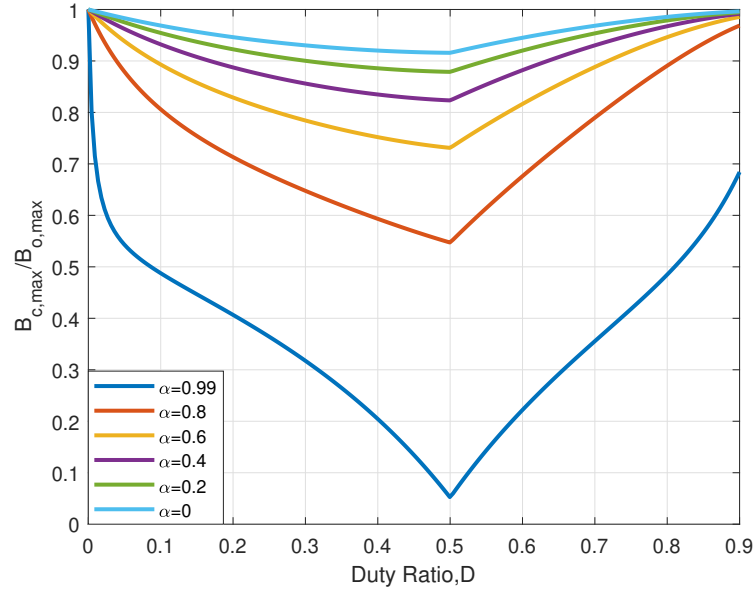


Figure 5.10: Magnetic flux density ratio of the center leg to the outer leg of the LCI vs duty cycle as a function of coupling coefficient, α

In Eq. 5.13 and Eq. 5.14, relationships between coupling coefficient and self inductance are given. For a constant ΔI_{in} , as the coupling coefficient increases more turns are required. At the same time both AC and DC magnetic flux densities decreases, vice-versa. Fig. 5.11 shows the AC and DC component of the magnetic flux densities of the outer and center legs and the number of turns as a function of α . Fig. 5.12 shows the relationship between the number of turns, B_{peak} and α . As can be seen, the outer leg peak magnetic flux density is always greater than the center leg magnetic flux density. For selecting α , there are some practical limits such as fill factor which limits the number of turns and saturation of core which limits the peak magnetic flux density on the core. For this study, as seen from the Fig. 5.12 coupling factor can take a value from 0.65 to 0.9. In order to find the optimum value for the coupling coefficient, power losses of the LCI are analyzed. Fig. 5.13 shows the power loss of the LCI versus the coupling factor. As the coupling factor decreases, the inductor current ripple increases for constant input current ripple which results in an increase in core loss and AC winding loss. On the other hand, conduction loss decreases with

decreasing coupling factors. The most dominant part of total inductor loss is the DC winding loss which is mainly affected by the number of turns. From an efficiency point of view the optimum value of the coupling coefficient is the minimum value limited by saturation. However, it would be reasonable to leave some margin from the saturation limit as magnetic flux density will increase due to fringing effects. In conclusion, it seems that selected α as 0.7 which brings inductor current ripple to 25% is also reasonable in terms of efficiency and utilization of the core.

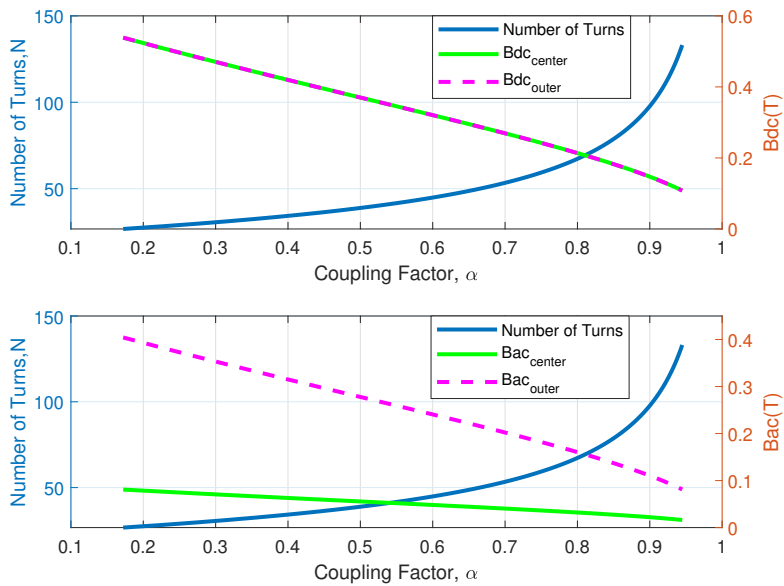


Figure 5.11: For constant ΔI_{in} , AC magnetic flux density, DC magnetic flux density and number of turns of LCI vs coupling factor, α

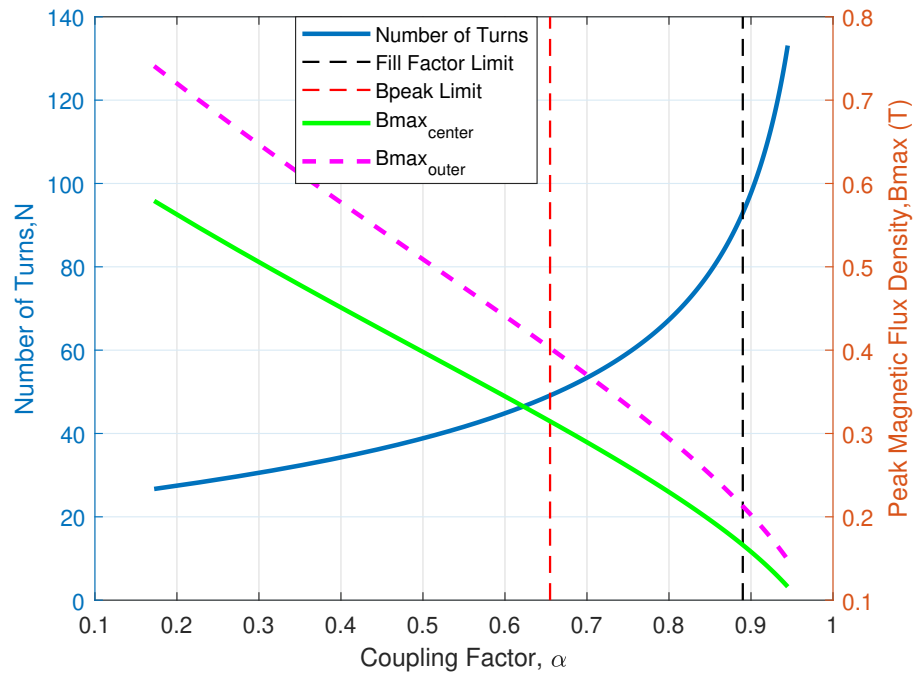


Figure 5.12: For constant ΔI_{in} , peak magnetic flux density and number of turns of LCI vs coupling factor, α

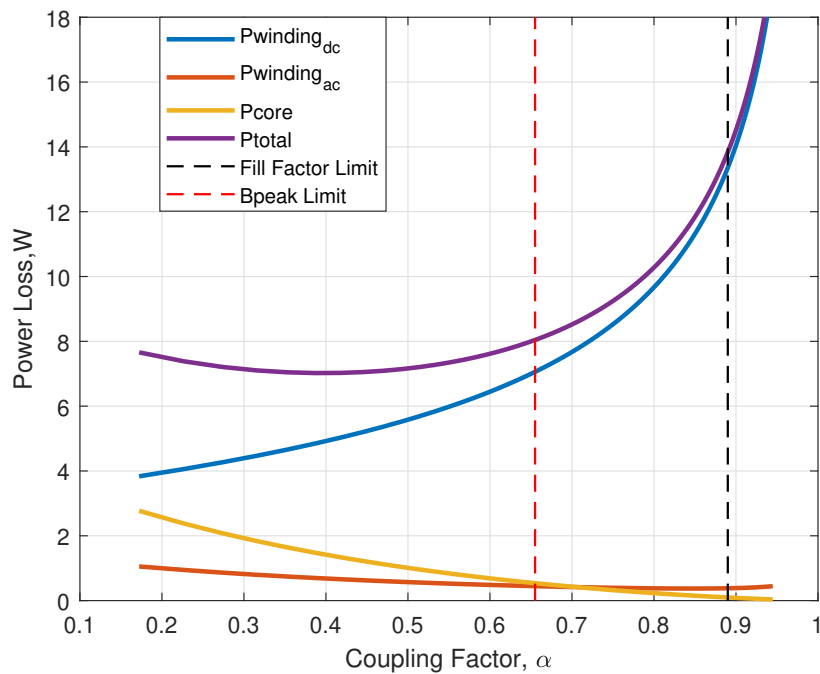


Figure 5.13: Power loss of LCI as a function coupling factor, α

5.4 Integrated Winding Coupled Inductor

The formulas derived in Section 4.3.2 and Section 4.3.1 are used to design the IWCI. Operating point is selected as maximum power and minimum input voltage since the magnetic flux density increases with respect to the duty cycle. Similar to LCI, the maximum flux density of the outer legs of IWCI is always greater than the maximum flux density of the center leg as can be seen in Fig. 5.14. The ratio between the center leg magnetic flux density and outer leg magnetic flux density decreases with increasing coupling coefficient, α and increases with increasing ratio of the turns ratio of the center leg winding to the turns ratio of the outer leg windings, β . Thus, the operating point is selected as maximum power and minimum input voltage.

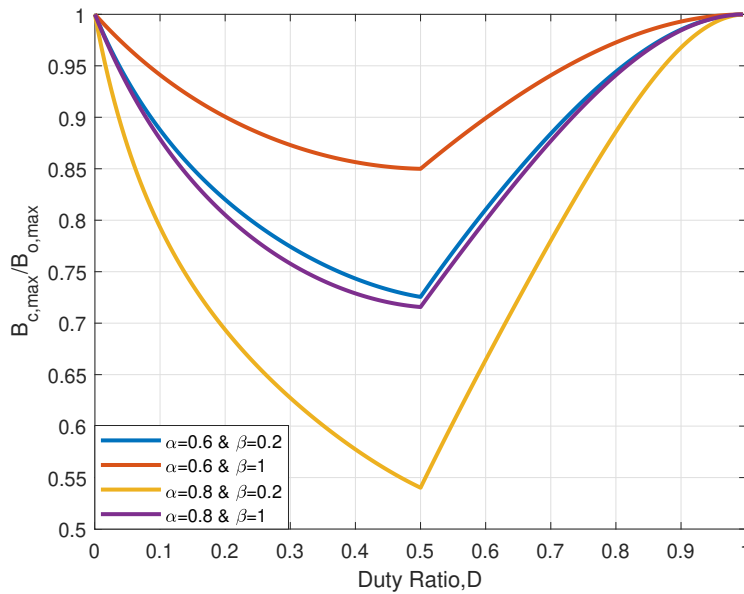


Figure 5.14: Magnetic flux density ratio of the center leg to the outer leg of the IWCI vs duty cycle as a function of coupling coefficient, α

5.4.1 Design Methodology

A design methodology given in Fig. 5.15 is proposed and IWCI is designed by following this methodology. The design steps following the initialization are explained in the following text.

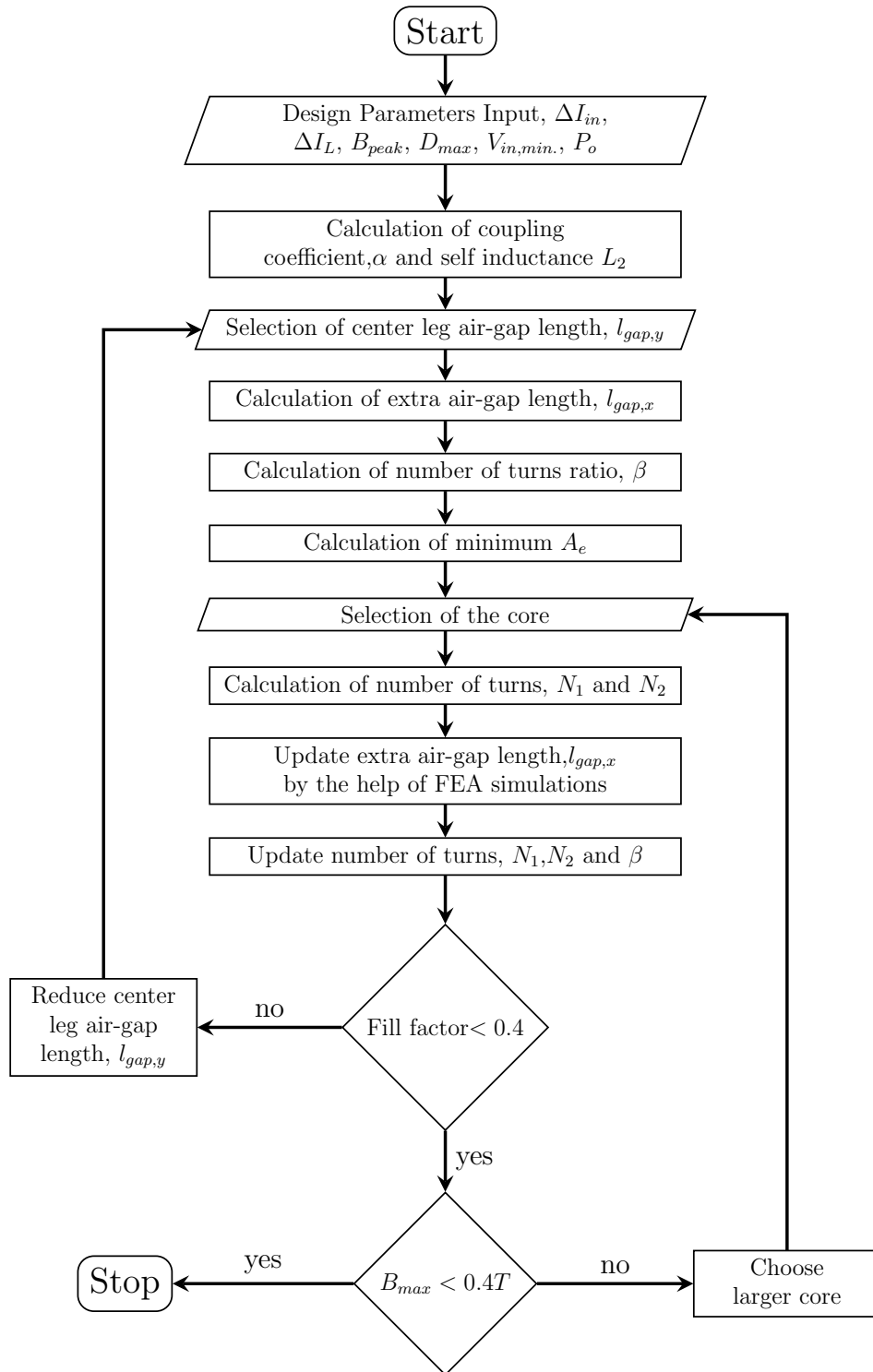


Figure 5.15: IWCI design flowchart

Step 1: Selection of coupling coefficient and calculation of L_2 from current ripple equations

By using the inductor current ripple equation Eq. 4.50 and input current ripple equation Eq. 4.51 the required self-inductance of the outer windings, L_2 and coupling coefficient between the outer windings can be calculated as:

$$\left[\frac{2 \cdot 150}{2L_1 + L_2 + 4M_1 - M_2} \right] (0.625 - 0.5) \cdot 20 \cdot 10^{-6} = 2$$

$$M_1 = \frac{L_1 N_2}{2N_1} \quad (5.24)$$

$$\frac{2(N_1 + N_2)}{N_1} L_1 + (1 - \alpha)L_2 = 375 \cdot 10^{-6}$$

$$\left[-\frac{50}{\frac{2(N_1 + N_2)}{N_1} L_1 + (1 - \alpha)L_2} - \frac{200}{(1 + \alpha)L_2} \right] (1 - 0.625) \cdot 20 \cdot 10^{-6} = -1.7$$

$$(1 + \alpha)L_2 = 2142.85 \cdot 10^{-6} \quad (5.25)$$

Coupling coefficient between the outer leg windings of IWCI, α is selected as 0.75. As known from Section. 5.3.3, that values of coupling coefficient reduces the power loss of the inductor. The self-inductance of outer leg windings is calculated by substituting α value into the Eq. 5.25.

$$\alpha = 0.75 \quad (5.26)$$

$$L_2 = 1224 \mu H$$

Step 2: Selection of the gap on the center leg, $l_{gap,y}$

The effect of air-gap length on inductor parameters is similar to LCI as explained before. For the initial design point, E-E core with 4mm air-gap length on the center leg is selected.

Step 3: Calculation of extra air-gap applied on all legs, $l_{gap,x}$

In this step, in order to obtain the desired coupling coefficient between the outer leg windings, the extra air-gap added on all legs of the magnetic core is calculated. In the figure below this extra air-gap length is denoted as $l_{gap,x}$ while air-gap on the center

leg only which comes with magnetic core denoted as $l_{gap,y}$. Illustration of air-gaps on magnetic core is shown in Fig. 5.6.

$$\alpha = \frac{\mathcal{R}_{mc}}{\mathcal{R}_{mc} + \mathcal{R}_{mo}}$$

$$\alpha = \frac{l_{gap,x} + l_{gap,y}}{\mu_0 \dot{A}_e} \quad (5.27)$$

$$\frac{l_{gap,x} + l_{gap,y}}{\mu_0 \dot{A}_e} + \frac{l_{gap,x}}{\mu_0 \dot{A}_e / 2}$$

The solution of Eq. 5.27 is $l_{gap,x} = 0.8mm$. Note that, in this calculation, the effect of fringing flux is not considered. It will be taken into account in the later steps.

Step 4: Calculation of the turns ratio, β

In this step, the ratio of the number of turns of the center leg winding to the number of turns of the outer leg windings, β is calculated.

$$\beta = \frac{N_1}{N_2} \quad (5.28)$$

The inductances of the IWCI can be written as below.

$$L_1 = N_1^2 \frac{1}{\mathcal{R}_{mo} + 2\mathcal{R}_{mc}}$$

$$M_1 = \frac{N_1 N_2}{2} \frac{1}{\mathcal{R}_{mo} + 2\mathcal{R}_{mc}} \quad (5.29)$$

$$L_2 = N_2^2 \frac{\mathcal{R}_{mc} + \mathcal{R}_{mo}}{\mathcal{R}_{mo}^2 + 2\mathcal{R}_{mc}\mathcal{R}_{mo}}$$

$$M_2 = N_2^2 \frac{\mathcal{R}_{mc}}{\mathcal{R}_{mo}^2 + 2\mathcal{R}_{mc}\mathcal{R}_{mo}}$$

Substituting Eq. 5.28 and Eq. 5.29 into the Eq. 5.24 the β can be calculated as:

$$2\beta(\beta + 1) = \frac{375 \cdot 10^{-6} - (1 - \alpha)L_2}{(1 - \alpha)L_2} \quad (5.30)$$

$$\beta = 0.37$$

Step 5: Calculation of the minimum cross-section area, A_e

As can be seen from Eq. 4.41, Eq. 4.42 and Fig. 5.14, peak magnetic flux density of outer legs always greater than the peak magnetic flux of center leg. Therefore,

peak outer leg flux density is considered when selecting the magnetic core. By using Eq. 4.41, peak magnetic flux density of the outer legs of IWCI can be written as:

$$B_{peak,o} = \frac{\frac{(2\beta + 1)N_2I_{av}}{\mathcal{R}_{mo} + 2\mathcal{R}_{mc}} + \frac{0.5V_o(\beta + D)(1 - D)T_s}{N_2(2\beta + 1)}}{A_e/2} \quad (5.31)$$

where,

$$\begin{aligned} \mathcal{R}_{mo} + 2\mathcal{R}_{mc} &= \frac{1 + \alpha}{1 - \alpha} \mathcal{R}_{mo} \\ N_2 &= \sqrt{\mathcal{R}_{mo}(1 + \alpha)L_2} \\ \mathcal{R}_{mo} &= \frac{2l_{gap,x}}{\mu_0 A_e} \end{aligned} \quad (5.32)$$

Substituting Eq. 5.32 into the Eq. 5.31 yields,

$$A_e = \left[\frac{2(2\beta + 1)^2(1 - \alpha)L_2 + V_o(\beta + D)(1 - D)T_s}{B_{peak,o}(2\beta + 1) \sqrt{\frac{2l_{gap,x}L_2(1 + \alpha)}{\mu_0}}} \right]^2 \quad (5.33)$$

As mentioned before, the fringing effect has not been taken into account yet. So, for a ferrite core with 0.4T saturation magnetic flux density value limiting B_{peak} to 0.3T is a good design input for A_e calculation to select a core. Solving Eq. 5.33 for 0.3T B_{peak} gives the minimum A_e value as $316.04mm^2$. Based on this volume, E55/28/21 core with N87 material [38] which has A_e of $347mm^2$ from TDK is selected.

Step 6: Calculation of the number of turns, N_1 and N_2

After selection of the magnetic core, the number of turns N_1 and N_2 can be calculated by using the equation Eq. 5.34.

$$\begin{aligned} N_2 &= \sqrt{L_2 \mathcal{R}_{mo}} \\ N_1 &= \beta N_2 \end{aligned} \quad (5.34)$$

The reluctances are calculated as:

$$\begin{aligned} \mathcal{R}_{mc} &= \frac{l_c - l_{gap,x} - l_{gap,y}}{\mu_r \mu_0 A_e} + \frac{l_{gap,x} + l_{gap,y}}{\mu_0 A_e} = 11.04 \frac{A}{uWb} \\ \mathcal{R}_{mo} &= \frac{l_o - l_{gap,x}}{\mu_r \mu_0 A_e/2} + \frac{l_{gap,x}}{\mu_0 A_e/2} = 3.69 \frac{A}{uWb} \end{aligned} \quad (5.35)$$

Substituting Eq. 5.35 into the Eq. 5.34 gives number of turns, N_2 equals 89 and N_1 equals 33.

Step 7: Update $l_{gap,x}$ by using FEA simulations

As stated before, until now the fringing effect is ignored. FEA simulations are used to find the value of $l_{gap,x}$. As seen from Fig. 6.7, coupling coefficient, α equals 0.75 when $l_{gap,x}$ equals 0.2mm. The reluctances are re-calculated with the new air-gap length.

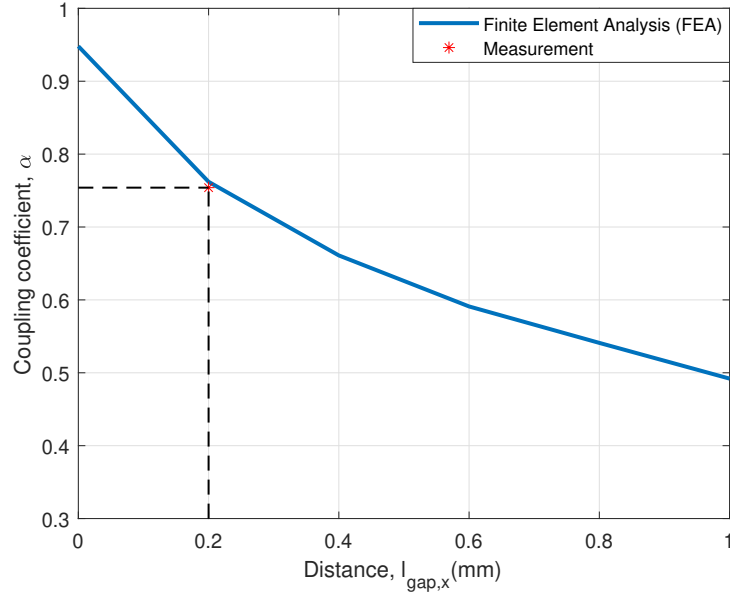


Figure 5.16: Coupling coefficient vs air-gap distance of FEA solution of the IWCI

Step 8: Update Number of Turns, N_1 and N_2

In this step, the number of turns is updated according to new reluctance values. The reluctances are calculated from FEA results. The reluctances \mathcal{R}_{mo} and \mathcal{R}_{mc} can be calculated by using the following formula.

$$\lambda = N\phi$$

$$\phi_{dc,outer} = \frac{(2N_1 + N_2)I_{av}}{\mathcal{R}_{mo} + 2\mathcal{R}_{mc}} \quad (5.36)$$

$$\alpha = \frac{\mathcal{R}_{mc}}{\mathcal{R}_{mo} + \mathcal{R}_{mc}}$$

From FEA simulations, average value of λ of the outer leg windings is found as 0.000049 Weber. α is found as 0.765. Substituting these values into Eq. 5.36, the

reluctances can be found as:

$$\begin{aligned}\mathcal{R}_{mo} &= 1.068 \frac{A}{\mu\text{Weber}} \\ \mathcal{R}_{mc} &= 3.477 \frac{A}{\mu\text{Weber}}\end{aligned}\tag{5.37}$$

The new value of the number of turns can be calculated by substituting reluctance results and the self inductance result of outer leg windings, L_2 which is found as $1137\mu\text{H}$ into the Eq. 5.30 and Eq. 5.34. The new values of the number of turns are as follows.

$$\begin{aligned}N_2 &= 45 \\ \beta &= 0.164 \\ N_1 &= 7\end{aligned}\tag{5.38}$$

Step 9: Checking fill factor, k_{cu}

After updating the number of turns, it can be checked whether this number of turns exceeds the fill factor limit. Fill factor can be calculated by using Eq. 5.11. Again AWG22 wire is used for windings of the IWCI. If the fill factor is higher than the limit value at this step, a smaller air gap can be selected by returning to the 2nd step. A smaller air gap will result in a smaller number of turns.

Step 10: Checking B_{peak}

In the final step of the design procedure, after updating the number of turns B_{peak} should be checked whether it is less than the saturation level of the magnetic core. It can also be calculated by using the reluctance values calculated in FEA simulations and Eq. 5.31. FEA results show that the maximum value of magnetic flux density of the core reaches 0.379 Tesla which is below the saturation level. This step finalizes the design procedure. If B_{peak} is found greater than the limit value, a new iteration of the design procedure can be applied with a larger core.

5.4.2 Finite Element Analysis (FEA) Simulations

FEA simulations are performed by using ANSYS Maxwell 3D. The model of the IWCI in FEA simulations is shown in Fig. 5.18. The windings of the IWCI are modeled as a stranded conductor and these windings are excited by using the current

waveforms of the two-phase interleaved converter with IWCI that is taken from the circuit simulations. The 3D model is simulated by using a transient solver. FEA result of the magnetic flux density along the outer leg of the core is given in Fig. 5.17. The magnitude of the magnetic flux density plot on the magnetic core at the time when the current of the outer leg winding is at its maximum value is given in Fig. 5.18.

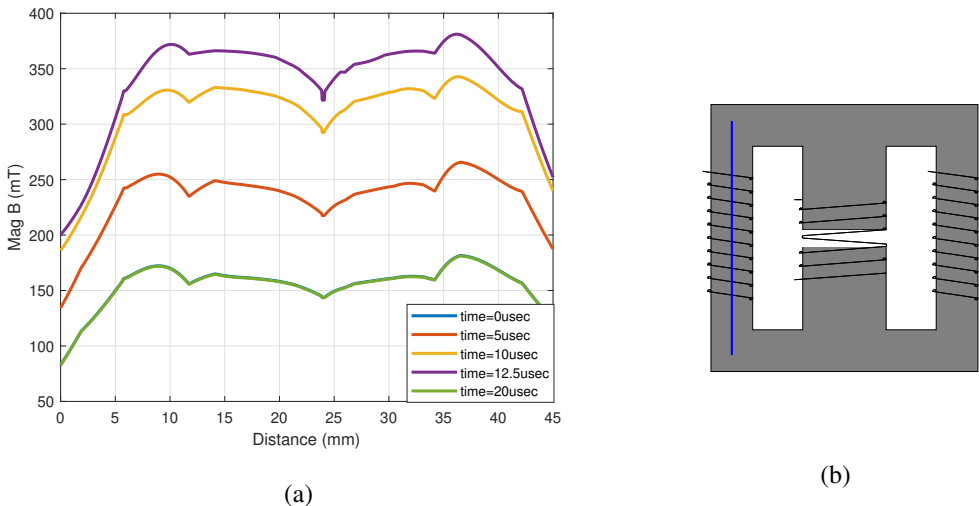


Figure 5.17: FEA result of the magnitude of the magnetic flux density along the line shown in b) on the outer leg legs of the IWCI

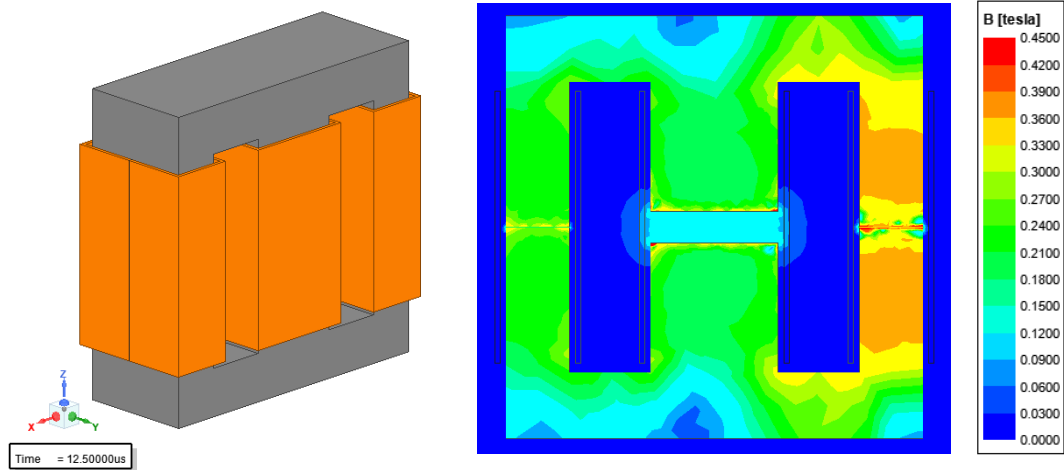


Figure 5.18: 3D model of IWCI in FEA and magnitude of magnetic flux density of the core along the cross-section of x-z plane

5.5 Close-Coupled Inductor

The close-coupled inductor topology consists of two inductors. One is called a boost inductor which is connected in series to the input side and limits the input current ripple. The other one is called a close-coupled inductor which is consist of two strongly coupled windings that are connected to the phases of a two-phase boost converter. This inductor is limiting the inductor current ripple. These two inductors are designed separately.

5.5.1 Boost Inductor

The formulas derived in Section 4.4.2 and Section 4.4.1 are used to design the BI.

5.5.1.1 Design Methodology

The design methodology of the BI is very similar to the DIs design methodology. The same design flowchart shown in Fig. 5.1 can be used. The equations for the current ripple and magnetic flux density are different from the DIs.

Step 1: Calculation of the self-inductance, L_1

By using the input current ripple equation Eq. 4.71 the required inductance of boost inductor, L_1 can be calculated as:

$$\left[\frac{2}{2L_1 + L_2 - M_2} 150 \right] (0.625 - 0.5) \cdot 20 \cdot 10^{-6} = 2$$
$$L_2 = M_2 \quad (5.39)$$
$$L_1 = 187.5 \cdot 10^{-6} \mu H$$

Step 2: Selection of the air-gap length, l_{gap}

In this step, the air-gap length which is applied to the inductor is chosen. It is selected as 1.75mm. Selecting air-gap length smaller results in a larger magnetic core. While selecting larger air-gap length results in a higher number of turns which will increase both copper loss and fill factor.

Step 3: Calculation of the minimum cross-section area, A_e

Minimum cross-section area, A_e is calculated from B_{peak} limit. By using Eq. 4.62, peak magnetic flux density of the boost inductor can be written as:

$$B_{peak} = \frac{\frac{N_1 I_{in}}{\mathcal{R}_{mb}} + \frac{V_{in}(D - 0.5)T_s}{2N_1}}{A_e} \quad (5.40)$$

where,

$$\begin{aligned} \mathcal{R}_{mb} &= 0.5\mathcal{R}_{mo} + \mathcal{R}_{mc} \\ \mathcal{R}_{mb} &= \frac{2l_{gap}}{\mu_0 A_e} \\ N_1 &= \sqrt{\mathcal{R}_{mb} L_1} \end{aligned} \quad (5.41)$$

Substituting Eq. 5.41 into the Eq. 5.40 yields,

$$A_e = \left[\frac{L_1 I_{in} + 0.5V_{in}(D - 0.5)T_s}{B_{peak} \sqrt{\frac{2l_{gap} L_1}{\mu_0}}} \right]^2 \quad (5.42)$$

The fringing effect has not been taken into account yet. So, for a ferrite core with 0.4T saturation magnetic flux density value limiting B_{peak} to 0.25T is a good design input for A_e calculation to select a core. Solving Eq. 5.42 for 0.25T B_{peak} gives the minimum A_e value of $215mm^2$. Based on this volume, ETD49/25/16 core with N87 material [37] which has A_e of $211mm^2$ from TDK is selected.

Step 4: Calculation of number of turns, N_1

After selection of the magnetic core, the number of turns can be calculated by using the equation Eq. 5.43.

$$L_1 = \frac{N_1^2}{0.5\mathcal{R}_{mo} + \mathcal{R}_{mc}} \quad (5.43)$$

The reluctances are calculated as:

$$\begin{aligned} \mathcal{R}_{mc} &= \frac{l_c - l_{gap}}{\mu_r \mu_0 A_e} + \frac{l_{gap}}{\mu_0 A_e} = 6.9 \frac{A}{uWb} \\ \mathcal{R}_{mo} &= \frac{l_o - l_{gap}}{\mu_r \mu_0 A_e / 2} + \frac{l_{gap}}{\mu_0 A_e / 2} = 13.3 \frac{A}{uWb} \end{aligned} \quad (5.44)$$

Substituting Eq. 5.44 into the Eq. 5.43 gives number of turns, N_1 equals 50.

Step 5: FEA analysis and update the number of turns, N_1

In this step, the number of turns is updated according to new reluctance values. The reluctances are calculated from FEA results. The reluctances \mathcal{R}_{mo} and \mathcal{R}_{mc} can be calculated by using the following formula.

$$\begin{aligned}\lambda &= N\phi \\ \phi_{dc} &= \frac{2N_1 I_{in}}{\mathcal{R}_{mo} + 2\mathcal{R}_{mc}} \\ \mathcal{R}_{mo} &= 2\mathcal{R}_{mc}\end{aligned}\tag{5.45}$$

From FEA simulations, average value of λ is found as 0.0044 Weber. Substituting this value into Eq. 5.45, the reluctances can be found as:

$$\begin{aligned}\mathcal{R}_{mo} &= 7.568 \frac{A}{\mu\text{Weber}} \\ \mathcal{R}_{mc} &= 3.784 \frac{A}{\mu\text{Weber}}\end{aligned}\tag{5.46}$$

The new value of the number of turns can be calculated by substituting reluctance results into Eq. 5.43 which yields the number of turns, N_1 as 37.

Step 6: Checking fill factor, k_{cu}

After updating the number of turns, it can be checked whether this number of turns exceeds the fill factor limit. Fill factor can be calculated by using Eq. 5.11. If the fill factor is higher than the limit value at this step, a smaller air gap can be selected by returning to the 2nd step. A smaller air gap will result in a smaller number of turns.

Step 7: Checking B_{peak}

In the final step of the design procedure, after updating the number of turns, B_{peak} should be checked whether it is less than the saturation level of the magnetic core. It can also be calculated by using the reluctance values calculated in FEA simulations and Eq. 5.40. FEA results show that the maximum value of magnetic flux density of the core reaches 0.364 Tesla which is below the saturation level. This step finalizes the design procedure.

5.5.1.2 Finite Element Analysis (FEA) Simulations

FEA simulations are performed by using ANSYS Maxwell 3D. The model of the BI in FEA simulations is shown in Fig. 5.20. The winding of the BI is modeled as a stranded conductor and this winding is excited by using the input current waveform of the two-phase interleaved converter with CCI that is taken from the circuit simulations. The 3D model is simulated by using a transient solver. FEA result of magnetic flux density along the center leg of the core is given in Fig. 5.19. The magnitude of magnetic flux density plot on the magnetic core at the time when the current of the winding is at its maximum value is given in Fig. 5.20.

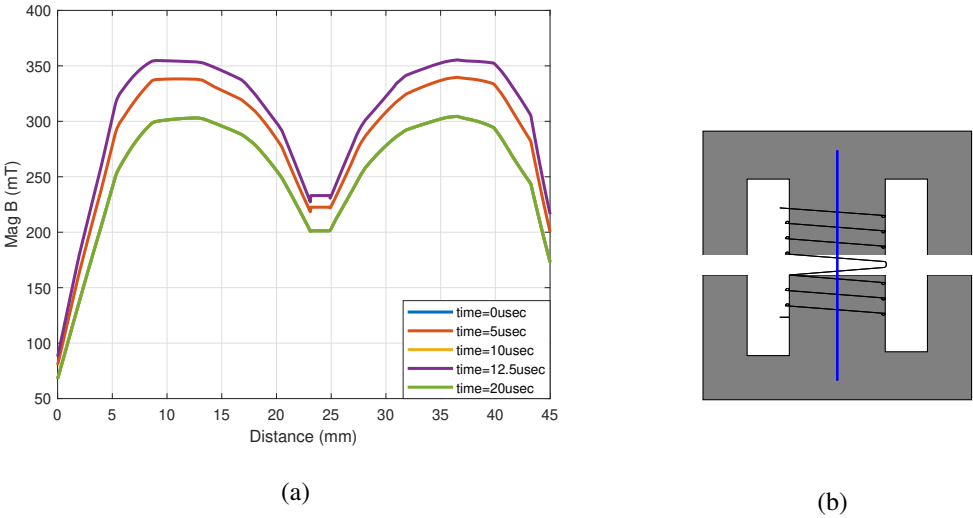


Figure 5.19: FEA result of the magnitude of the magnetic flux density along the line shown in b) on the center leg legs of the BI

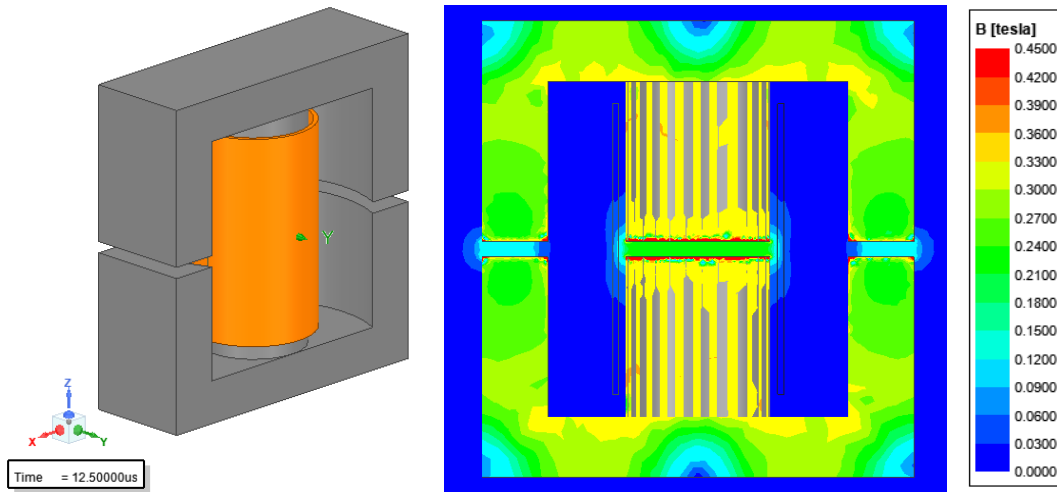


Figure 5.20: 3D model of CCI-BI in FEA and magnitude of magnetic flux density of the core along the cross-section of x-z plane

5.5.2 Close-Coupled Inductor

The close-coupled inductor which is shown in Fig. 4.12 consists of two windings that are strongly coupled to each other. Therefore, there are not any DC fluxes in the core of CCI and this allows a smaller core to be selected for it. The self-inductances of CCI are determined by the inductor current ripple value. CCI is designed at $D = 0.5$ because it's peak magnetic flux reaches the maximum value at this point. Fig. 5.21 shows the ratio of peak magnetic flux of CCI to the peak magnetic flux at $D = 0.5$.

5.5.2.1 Design Methodology

A design methodology is proposed and CCI is designed by following this methodology. The proposed design flowchart is given in below in Fig. 5.22.

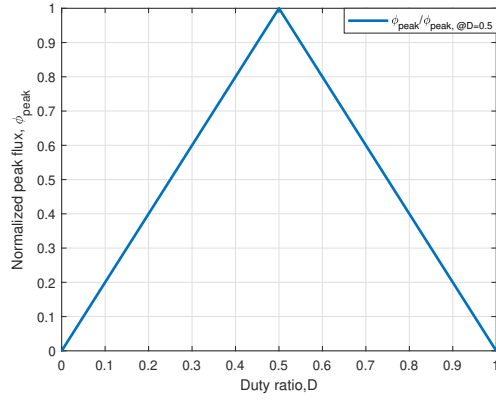


Figure 5.21: Ratio of peak magnetic flux of the CCI normalized to the peak magnetic flux at D=0.5

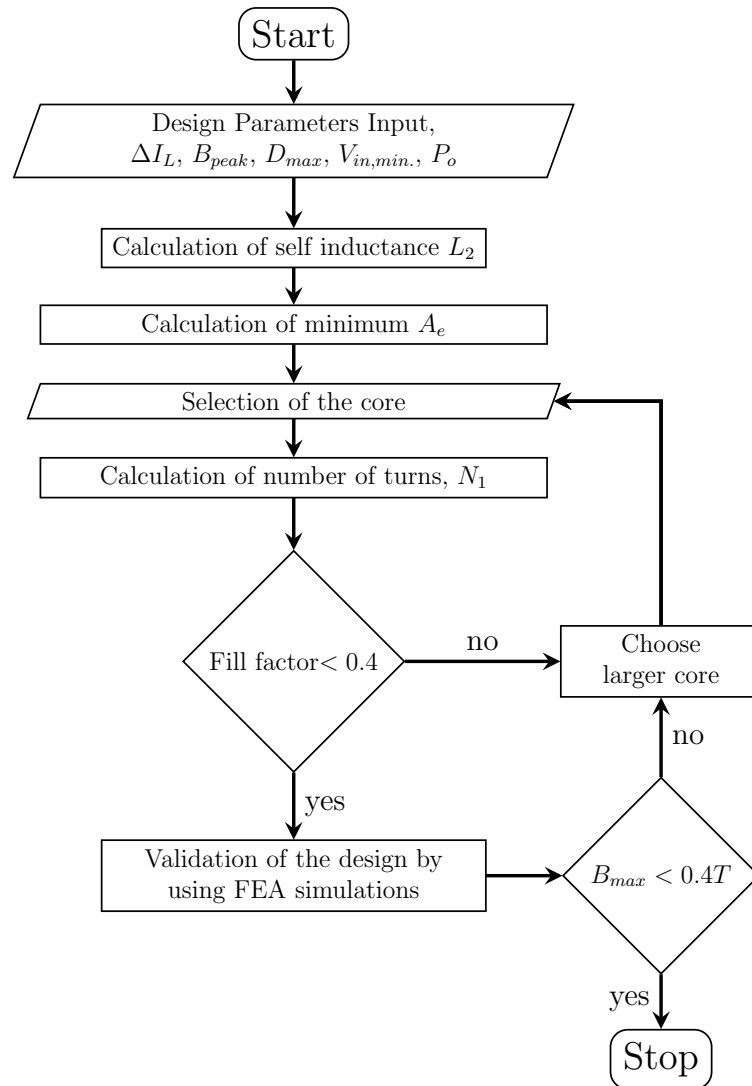


Figure 5.22: CCI design flowchart

Step 1: Calculation of the self-inductance, L_2

By using the inductor current ripple equation Eq. 4.70 the required self-inductance of the CCI windings, L_2 can be calculated as:

$$\left[-\frac{50}{2 \cdot 187.5 \cdot 10^{-6} + L_2 - M_2} - \frac{200}{L_2 + M_2} \right] (1 - 0.625) 20 \cdot 10^{-6} = -1.7 \quad (5.47)$$

$$L_2 = M_2 = 1071 \cdot 10^{-6} \mu H$$

Step 2: Calculation of minimum cross-section area, A_e

As stated above, peak magnetic flux density reaches its maximum at $D = 0.5$ for CCI. The Minimum cross section area, A_e is calculated from B_{peak} limit. By using Eq. 4.61 at this point. Peak magnetic flux density of the CCI at $D = 0.5$ can be written as:

$$B_{peak} = \frac{V_{in} T_s}{4 N_2 A_e} \quad (5.48)$$

where,

$$N_2 = \sqrt{(0.5 \mathcal{R}_{mo} + \mathcal{R}_{mc}) L_2}$$

$$\mathcal{R}_{mo} = \frac{2l_o}{\mu_0 \mu_r A_e} \quad (5.49)$$

$$\mathcal{R}_{mc} = \frac{l_c}{\mu_0 \mu_r A_e}$$

In order to simplify design procedure, the following assumptions can be made.

$$l_o = 2l_c$$

$$l_c = 2.5 \sqrt{\frac{4A_e}{\pi}} \quad (5.50)$$

Substituting Eq. 5.49 and Eq. 5.50 into Eq. 5.48 yields,

$$A_e = \left[\frac{V_{in} T_s}{4 \sqrt{\frac{L_2 \cdot 15}{\sqrt{\pi} \mu_0 \mu_r} B_{peak}}} \right]^{\frac{4}{3}} \quad (5.51)$$

Since there is not any air-gap on the core of CCI, there is not any fringing fluxes. Therefore, for a ferrite core with 0.4 Tesla saturation magnetic flux density value B_{peak}

is selected as high as 0.375Tesla for A_e calculation to select a core. This is the main advantage of CCI along with zero dc flux on the core. Solving Eq. 5.51 for 0.375Tesla B_{peak} gives the minimum A_e value of $167.56mm^2$. As a magnetic core, ETD44/22/15 core with N87 material [41] which has A_e of $172mm^2$ from TDK is selected.

Step 3: Calculation of the number of turns, N_2

After selection of the magnetic core, the number of turns can be calculated by using Eq. 5.52.

$$L_2 = \frac{N_2^2}{0.5\mathcal{R}_{mo} + \mathcal{R}_{mc}} \quad (5.52)$$

The reluctances are calculated as:

$$\begin{aligned} \mathcal{R}_{mc} &= \frac{l_c}{\mu_r \mu_0 A_e} = 0.08 \frac{A}{uWb} \\ \mathcal{R}_{mo} &= \frac{l_o}{\mu_r \mu_0 A_e / 2} = 0.3 \frac{A}{uWb} \end{aligned} \quad (5.53)$$

Substituting the reluctance values and L_2 value into Eq. 5.52 gives the number of turns, N_2 as 16.

Step 4: Checking fill factor, k_{cu}

After calculating the number of turns, it can be checked whether this number of turns exceeds the fill factor limit. Fill factor can be calculated by using Eq. 5.11. For round-type conductors, as a rule of thumb 0.4 is a limited value for the fill factor. If the fill factor is higher than the limit value at this step, a larger core can be selected.

Step 5: Validation of design by using FEA

In the last step, validation of design can be done by using FEA simulation. Inductances, magnetic flux density etc. can be calculated using FEA. After that it can be checked whether these parameters are as expected and within an acceptable range. Fig 5.23 shows the FEA result of the magnitude of magnetic flux density along the center leg of the core of the CCI.

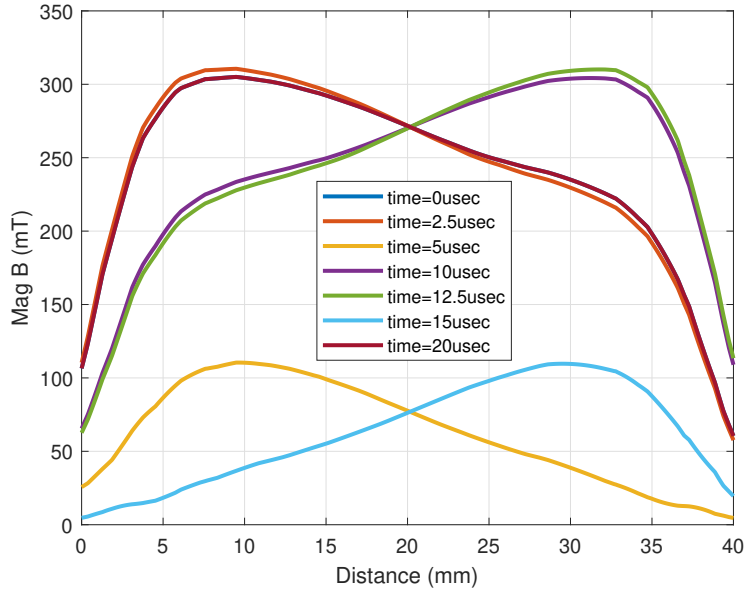


Figure 5.23: FEA result of the magnitude of magnetic flux density along the center leg of the CCI

5.6 Chapter Summary

In this chapter, different coupled inductor topologies and discrete inductors are designed. In the first part, the design condition is discussed. All inductors are designed so that they all have the same performance. For each inductor topology, design methodology is proposed. Detailed design procedures are explained. The effect of fringing fluxes on the inductor parameters is examined. FEA simulations are conducted and design parameters are updated based on the FEA results. Moreover, the effect of coupling coefficient on the inductor performance is examined for the LCI topology which will be valid for also IWCI topology.

CHAPTER 6

CONVERTER IMPLEMENTATION

In the previous chapter, LCI, IWCI, CCI and DI are designed by using the proposed design methodologies. In this chapter, properties of implemented inductors are presented. The measurement procedure for each coupled type of coupled inductors is proposed. Moreover, the effect of fringing flux on the reluctance of magnetic cores is analytically calculated by using proposed formulas in the literature. The comparison between the analytical calculation, FEA results and measurement results is done by considering the effect of fringing flux on inductors parameters. The other components of the two-phase interleaved boost converter are given in this chapter. After that power loss analysis is conducted. Moreover, the derivation of the transfer function of a two-phase interleaved boost converter with IWCI is provided.

6.1 Measurement Procedure for the Coupled Inductors

In this section, measurement procedures for the measurements of the inductances of LCI, IWCI and CCI are proposed.

6.1.1 LCI

Measurement of inductances of LCI can be done by using the following measurements and connections.

Measurement of self inductances

Measurement 1: (Self inductances measurement)

$L_{winding1}$ = Measurement across the terminals 1 and 2 while terminals 3 and 4 left open

$L_{winding2}$ = Measurement across the terminals 3 and 4 while terminals 1 and 2 left open

Generally, transformers leakage inductances are measured by shorting the secondary and measuring the primary. However, this measurement method does not give accurate results in LCI. Because the leakage inductance in LCI cannot be neglected. The leakage inductance of LCI can be measured by making the following connection. Measurement 2:(Leakage inductance measurement)

$2L_{leakage}$ = Measurement across the terminals 1 and 4 while terminals 2 and 3 are shorted

Then, the mutual inductance between the windings can be calculated by using the following formula.

$$M = Measurement1 - \frac{Measurement2}{2} \quad (6.1)$$

Electrical circuit connections and terminals of the LCI are shown in Fig. 6.1.

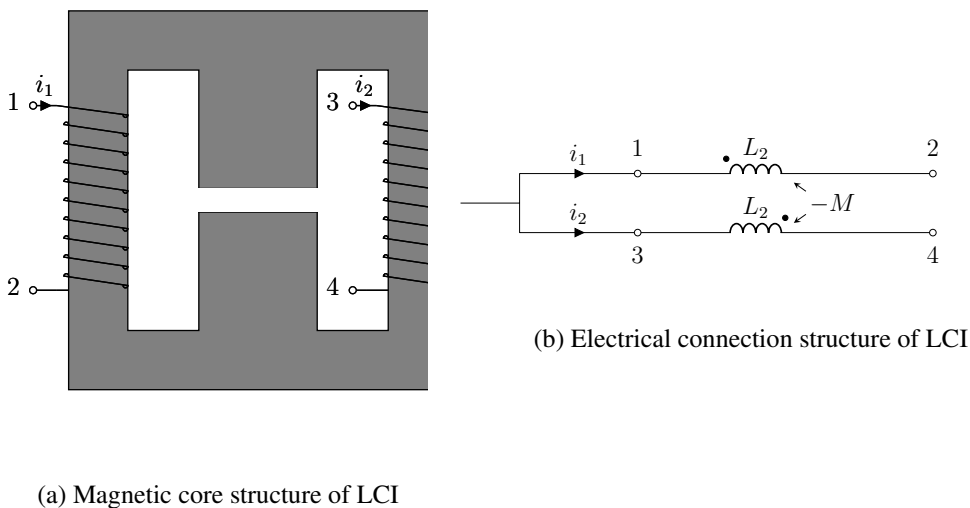


Figure 6.1: Electrical connections and terminals of the LCI

6.1.2 IWCI

Measurement of inductances of the IWCI can be done by using the following measurements and connections.

Terminals 2,3 and 5 are shorted.

Measurement1 = Measurement across terminals 5-6 or 3-4.

Measurement2 = Measurement across terminals 1 and 2.

Terminals 2,3 and 5 are not shorted. Terminals 3 and 6 are shorted.

Measurement3 = Measurement across terminals 5 and 6.

Measurement4 = Measurement across terminals 4 and 6.

Terminals 2,3 and 5 are not shorted. Terminals 3-6 and 1-2 are shorted.

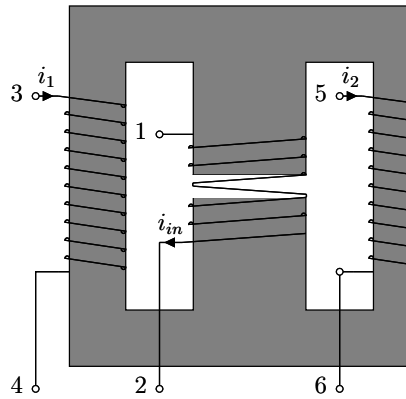
Measurement5 = Measurement across terminals 5 and 6.

Measurement6 = Measurement across terminals 4 and 5.

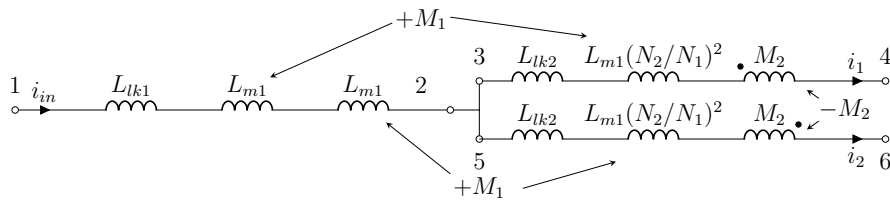
Then, the inductances can be calculated by using the following equations.

$$\begin{aligned}
 L_2 &= \textit{Measurement1} \\
 L_1 &= \textit{Measurement2} \\
 M_1 &= \frac{\textit{Measurement4} - \textit{Measurement6}}{2} \cdot \frac{N_1}{N_2} \\
 L_{m1} &= M_1 \frac{N_1}{N_2} \\
 L_{lk1} &= L_1 - 2L_{m1} \\
 M_2 &= L_2 - \frac{\textit{Measurement4}}{2}
 \end{aligned} \tag{6.2}$$

where N_1 is the number of turns of center winding and N_2 is the number of turns of the outer leg windings. Electrical circuit connections and terminals of IWCI are shown in Fig. 6.2.



(a) Magnetic core structure of IWCI



(b) Electrical connection structure of IWCI

Figure 6.2: Electrical connections and terminals of IWCI

6.1.3 CCI

Measurement of inductances of the CCI can be done by using the following measurements and connections.

Measurement of self-inductances

Measurement 1: (Self-inductances measurement)

$L_{winding1}$ = Measurement across terminals 1 and 2 while terminals 3 and 4 left open

$L_{winding2}$ = Measurement across terminals 3 and 4 while terminals 1 and 2 left open

Measurement 2:(Leakage inductance measurement)

$2L_{leakage} = \text{Measurement across terminals 1 and 4 while terminals 2 and 3 are shorted}$

Then, the mutual inductance between the windings can be calculated by using the following formula.

$$M = \text{Measurement1} - \frac{\text{Measurement2}}{2} \quad (6.3)$$

Electrical circuit connection and terminals of the CCI are shown in Fig. 6.3.

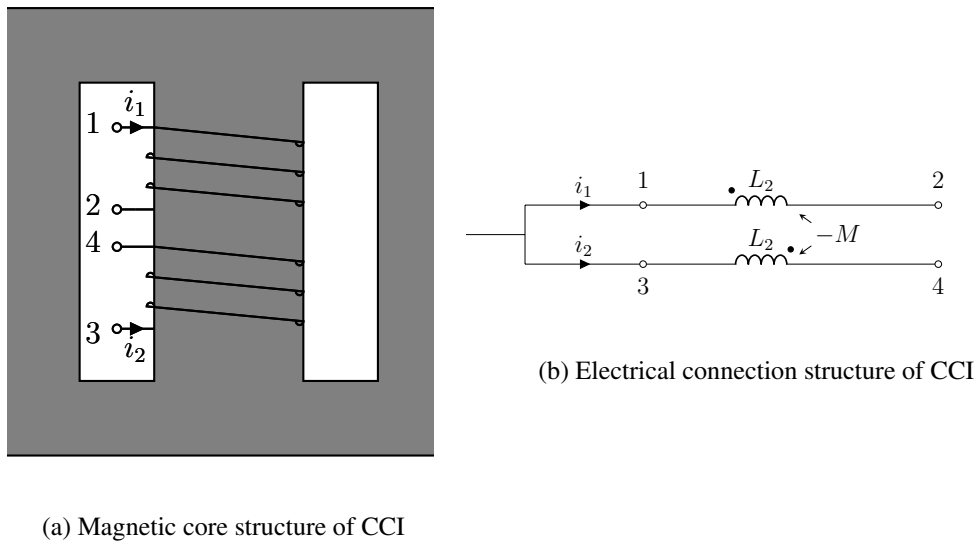


Figure 6.3: Electrical connection and terminals of CCI

6.2 Validation of FEA Results

In this section validation of FEA results is done by comparing them with measurement results. Moreover, the effect of fringing flux on the reluctances is calculated analytically by using proposed methods in the literature. Fringing fluxes around the air-gaps can have a drastic effect on coupling effect, inductance, maximum flux density and other inductor parameters. Therefore, for gapped inductors the reluctances of the magnetic core should be analyzed by considering the fringing effect.

Method 1:

This method, which is proposed in [40], calculates air-gap fringing flux effect on the reluctances by using the following formulas.

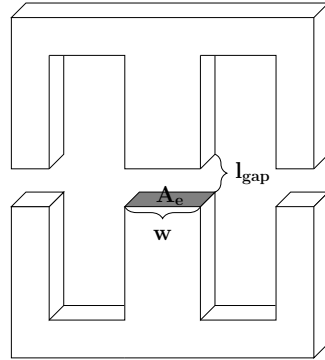


Figure 6.4: Method 1 dimensions definitions

$$X_{fq} = 1 + \frac{ql_{gap}}{\sqrt{A_{gap}}} \ln \frac{2w}{l_{gap}} \quad (6.4)$$
$$\mathcal{R}_{fq} = \frac{\mathcal{R}_{gap}}{X_{fq}}$$

In this equation, q is a constant used to reduce the accuracy error, l_{gap} is the length of the air-gap, A_{gap} cross-section area of the air-gap, w width of the core across the air-gap, X_{fq} correction factor for fringing flux, \mathcal{R}_{gap} reluctance of the air-gap without considering fringing effect, \mathcal{R}_{fq} reluctance of the air-gap with considering fringing effect. Mclayman did not propose the q coefficient in this formula. In another study [42] a constant is suggested in order to reduce the margin of error of this formula. For this coefficient, it is suggested a number between 0.85-0.95 for ETD cores and 1-1.1 for EE cores. However, these numbers do not sufficiently reduce the margin of error in reluctance calculations in our study. When the q value is set as 1.5 in the examinations made in this thesis, the margin of error for ETD cores has decreased considerably. Therefore, in this study, the q number is taken as 1.5. The main disadvantage of Mclayman's formula is that only the 2-D dimension core is analyzed while making these calculations.

Method 2:

The method is proposed in [39] which is more accurate than the previous one. This method considers the 3D fringing effect. The reluctance formulas for the outer leg and the center leg are given in Eq. 6.5, Eq. 6.6 and Eq. 6.7, Eq. 6.8, respectively.

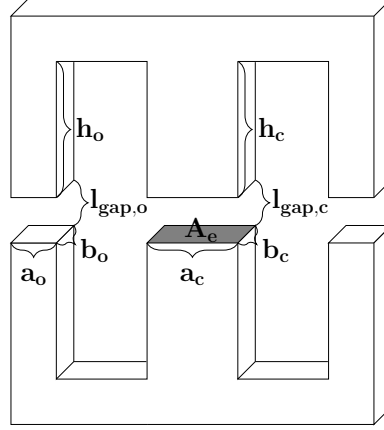


Figure 6.5: Method 2 dimensions definitions

$$F_{o-x} = \frac{\frac{a_o}{l_{gap,o}}}{\frac{a_o}{l_{gap,o}} + \frac{2}{\pi} \left(1 + \ln \frac{\pi h_o}{2l_{gap,o}}\right)} \quad F_{o-y} = \frac{\frac{b_o}{l_{gap,o}}}{\frac{b_o}{l_{gap,o}} + \frac{2}{\pi} \left(1 + \ln \frac{\pi h_o}{2l_{gap,o}}\right)} \quad (6.5)$$

$$\mathcal{R}_{o-total} = F_{o-x} \cdot F_{o-y} \cdot \frac{l_{gap,o}}{\mu_0 A_e / 2} \quad (6.6)$$

$$F_{c-x} = \frac{\frac{a_c}{l_{gap,c}}}{\frac{a_c}{l_{gap,c}} + \frac{2}{\pi} \left(1 + \ln \frac{\pi h_c}{2l_{gap,c}}\right)} \quad F_{c-y} = \frac{\frac{b_c}{l_{gap,c}}}{\frac{b_c}{l_{gap,c}} + \frac{2}{\pi} \left(1 + \ln \frac{\pi h_c}{2l_{gap,c}}\right)} \quad (6.7)$$

$$\mathcal{R}_{c-total} = F_{c-x} \cdot F_{c-y} \cdot \frac{l_{gap,c}}{\mu_0 A_e} \quad (6.8)$$

In these equations, a_c , a_o are the width of the core on the air-gap of the center leg and the outer leg, respectively. b_c , b_o are the depth of the core on the air-gap of the center leg and outer leg, respectively. h_c , h_o are the height from air-gap to core of the

center leg and outer leg, respectively. $l_{gap,c}$, $l_{gap,o}$ are the length of the air-gap of the center leg and outer leg, respectively. F_{c-x} , F_{o-x} are the fringing factors along the x-axis of the center leg and outer leg, respectively. F_{c-y} , F_{o-y} are the fringing factors along the y-axis of the center leg and outer leg, respectively. $\mathcal{R}_{c-total}$, $\mathcal{R}_{o-total}$ are the total reluctances with consideration of fringing flux of the center leg and outer leg, respectively.

6.2.1 Sensitivity Analysis for DI

Numerical calculations of reluctances considering the fringing effect are done by using the formulas presented in Section 6.2. The accuracy of these formulas is compared with FEA simulation results and measurement results. Table 6.1 shows that method 1 gives very close results to measurement and FEA results in inductance calculation by taking fringing effects into account. On the other hand, method 2 gives results that are not close to measurements.

Table 6.1: Comparison of Fringing Effect Calculation Methods with FEA and Experimental Results

	Method 1	Method 2	FEA Results	Measurement Results
L_1	$376.45\mu H$	$409.7\mu H$	$394.02\mu H$	$372.3\mu H$
B_{peak}	$0.32T$	$0.34T$	$0.332T$	<i>NA</i>
\mathcal{R}_{mo}	$6.55A/\mu Wb$	$5.74A/\mu Wb$	$6.93A/\mu Wb$	<i>NA</i>
\mathcal{R}_{mc}	$3.91A/\mu Wb$	$3.73A/\mu Wb$	$3.46A/\mu Wb$	<i>NA</i>
ΔI_{in}	$1.99A$	$1.83A$	1.90	$2.014A$

Sensitivity analysis can be done according to the change in inductance and hence in the input current ripple. Table 6.2 shows the error difference between the desired values for all methods, FEA and measurement results. For method 1, FEA and measurement the error difference is less than 1%. For method 2, the accuracy is less than the others which have nearly 10% error.

Table 6.2: Sensitivity Analysis of the DI Accuracy Error with Respect to Design Inputs

	Method 1	Method 2	FEA Results	Measurement Results
L_1	0.39%	9.25%	5.07%	0.72%
ΔI_{in}	0.5%	8.5%	5%	0.7%

6.2.2 Sensitivity Analysis for LCI

The relationship between the coupling coefficient of the LCI as a function of extra gap length is calculated with both methods. Fig. 6.6 shows that coupling coefficient calculated by method 2 is the same with FEA results. On the other hand, method 1 has some error. Also, note that the analytical solution neglecting the fringing effect calculates the coupling coefficient with a high error.

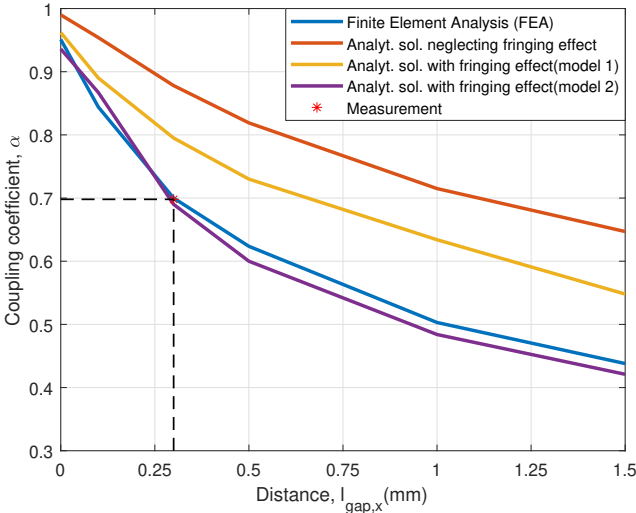


Figure 6.6: Coupling coefficient vs air-gap length calculated with different methods and FEA simulations

Even though good estimation of fringing effect on coupling coefficient by using method 2, as seen from Table 6.3, the reluctances and hence inductances calculated by method 2 are not close to the FEA results and measurement results. Therefore, the

current ripples are different from the expected. That difference in current ripple values makes it not possible to compare inductors designed under the same conditions, which is the main purpose of this study.

Table 6.3: Comparison of Fringing Effect Calculation Methods with FEA and Experimental Results

	Method 1	Method 2	FEA Results	Measurement Results
L	$1227.8\mu H$	$1367.3\mu H$	$1248\mu H$	$1261\mu H$
M	$965.4\mu H$	$954.6\mu H$	$879\mu H$	$880\mu H$
α	0.786	0.698	0.704	0.698
B_{peak}	$0.29T$	$0.39T$	$0.35T$	NA
\mathcal{R}_{mo}	$1.33A/\mu Wb$	$1.26A/\mu Wb$	$1.37A/\mu Wb$	NA
\mathcal{R}_{mc}	$4.89A/\mu Wb$	$2.90A/\mu Wb$	$3.20A/\mu Wb$	NA
ΔI_{in}	$2.86A$	$1.82A$	$2.03A$	$1.97A$
ΔI_L	$2.11A$	$1.55A$	$1.72A$	$1.68A$

Moreover, due to the practical limits, it is not possible to precisely adjust the air-gap length. The coupling coefficient is measured as 0.685. Also, inductances are measured slightly less than desired values. Sensitivity analysis can be done according to the change in coupling factor. Table 6.4 shows the error difference between the desired values for all methods, FEA and measurement results.

Table 6.4: Sensitivity Analysis of LCI Accuracy Error with Respect to Design Inputs

	Method 1	Method 2	FEA Results	Measurement Results
α	12.28%	0.28%	0.57%	0.28%
ΔI_{in}	43%	9%	1.5%	1.5%
ΔI_L	24.1%	8.8%	1.2%	1.2%

6.2.3 Sensitivity Analysis for IWCI

The relationship between the coupling coefficient of the LCI as a function of extra gap length is calculated with both methods. Fig. 6.7 shows that coupling coefficient calculated by method 2 is the same with FEA results. On the other hand, method 1 has some error. Also, note that the analytical solution neglecting the fringing effect calculates the coupling coefficient with a high error. Table 6.5 shows the results of both method, FEA simulations and measurements for the IWCI. As can be seen, FEA results are very close to the measurements. So, FEA simulations should be carried before implementing the IWCI.

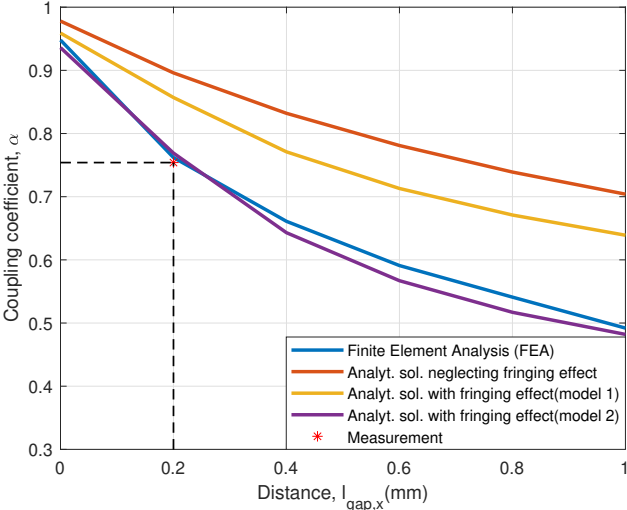


Figure 6.7: Coupling coefficient vs air-gap length calculated with different methods

Table 6.5: Comparison of Fringing Effect Calculation Methods with FEA and Experimental Results

	Method 1	Method 2	FEA Results	Measurement Results
L_1	$4.63\mu H$	$7.32\mu H$	$7.54\mu H$	$7.9\mu H$
M_1	$14.89\mu H$	$23.54\mu H$	$23.52\mu H$	$21.07\mu H$
L_2	$1340.8\mu H$	$1312.7\mu H$	$1136\mu H$	$1156\mu H$
M_2	$1149.4\mu H$	$1010\mu H$	$866\mu H$	$872\mu H$
α	0.857	0.769	0.762	0.754
B_{peak}	$0.33T$	$0.45T$	$0.379T$	NA
\mathcal{R}_{mo}	$0.81A/\mu Wb$	$0.87A/\mu Wb$	$1.068A/\mu Wb$	NA
\mathcal{R}_{mc}	$4.88A/\mu Wb$	$2.91A/\mu Wb$	$3.477A/\mu Wb$	NA
ΔI_{in}	$2.88A$	$1.82A$	$1.98A$	$1.95A$
ΔI_L	$2.04A$	$1.55A$	$1.74A$	1.72

As seen from the table, due to the practical limits it is not possible to precisely adjust the air-gap length. The coupling coefficient is measured as 0.754. Also, inductances are measured slightly less than desired values. Sensitivity analysis can be done according to the change in coupling factor. Table 6.6 shows the error difference between the desired values for all methods, FEA and measurement results. The difference is a maximum of 1.5% which is an acceptable value.

Table 6.6: Sensitivity Analysis of the IWCI Accuracy Error with Respect to Design Inputs

	Method 1	Method 2	FEA Results	Measurement Results
α	14.26%	2.53%	1.6%	0.53%
ΔI_{in}	44%	9%	1%	2.5%
ΔI_L	20%	8.82%	2.35%	1.18%

6.2.4 Sensitivity Analysis for BI

Numerical calculations of reluctances considering the fringing effect are done by using the formulas presented in Section 6.2. The accuracy of these formulas is compared with FEA simulation results and measurement results. Table 6.7 shows that method 1 gives very close results to measurement and FEA results in inductance calculation by taking the fringing effects into account. On the other hand, method 2 gives results that are not close to measurements.

Table 6.7: Comparison of Fringing Effect Calculation Methods with FEA and Experimental Results

	Method 1	Method 2	FEA Results	Measurement Results
L_1	$186.97\mu H$	$205.41\mu H$	$194.93\mu H$	$187.27\mu H$
B_{peak}	$0.35T$	$0.376T$	$0.364T$	<i>NA</i>
\mathcal{R}_{mo}	$6.66A/\mu Wb$	$5.78A/\mu Wb$	$7.013A/\mu Wb$	<i>NA</i>
\mathcal{R}_{mc}	$3.99A/\mu Wb$	$3.77A/\mu Wb$	$3.506A/\mu Wb$	<i>NA</i>
ΔI_{in}	$2.005A$	$1.82A$	1.92	$2.003A$

Sensitivity analysis can be done according to the change in inductance and hence in the input current ripple. Table 6.8 shows the error difference between the desired values for all methods, FEA and measurement results. For method 1, FEA and measurement the error difference is less than 1%. For method 2, the accuracy is less than the others which have nearly 10% error.

Table 6.8: Sensitivity Analysis of the CCI-BI Accuracy Error with Respect to Design Inputs

	Method 1	Method 2	FEA Results	Measurement Results
L_1	0.28%	9.55%	3.96%	0.12%
ΔI_{in}	0.25%	9%	4%	0.15%

6.3 Implementation of Inductors

Implemented inductor prototypes are shown in Fig. 6.8. The parameters of designed inductors are summarized in Table 6.9.

Table 6.9: Inductor Parameters

	DI	LCI	IWCI	CCI	CCI-BI
Inductance	$L_2 = 372.3\mu H$	$L_2 = 1261\mu H$ $M_2 = 880\mu H$	$L_1 = 7.9\mu H$ $M_1 = 21.07\mu H$ $L_2 = 1156\mu H$ $M_2 = 872\mu H$	$L_2 = 1010\mu H$ $M_2 = 997\mu H$	$L_1 = 187.27\mu H$
Number of turns	N=52	$N_2 = 54$	$N_1 = 7$ $N_2 = 45$	$N_2 = 16$	$N_1 = 37$
B_{peak}	0.332T	0.352T	0.379T	0.27T	0.364T
B_{pp}	0.17T	0.2T	0.23T	0.27T	0.05T
Rwinding	69.66m Ω	81.66m Ω	$R_{center} = 12.78m\Omega, R_{outer} = 85.83m\Omega$	24.1m Ω	26.6m Ω
Rwinding@50kHz	2.36 Ω	2.58 Ω	$R_{center} = 37m\Omega, R_{outer} = 2.339\Omega$	4.5 Ω	1.242 Ω
Current density	7A/mm ²	7A/mm ²	7A/mm ²	7A/mm ²	7A/mm ²
Number of parallel layer	3	3	Center= 6, Outer= 3	3	6
Cross section area	210mm ²	347.5mm ²	347.5mm ²	172mm ²	210mm ²
Core type	2x ETD49/25/16	E55/28/21	E55/28/21	ETD44/22/15	ETD49/25/16
Weight	336.9gr	323.3gr	330.7gr	134.1gr	189.2gr
Volume	95cm ³	100cm ³	105cm ³	45cm ³	50cm ³

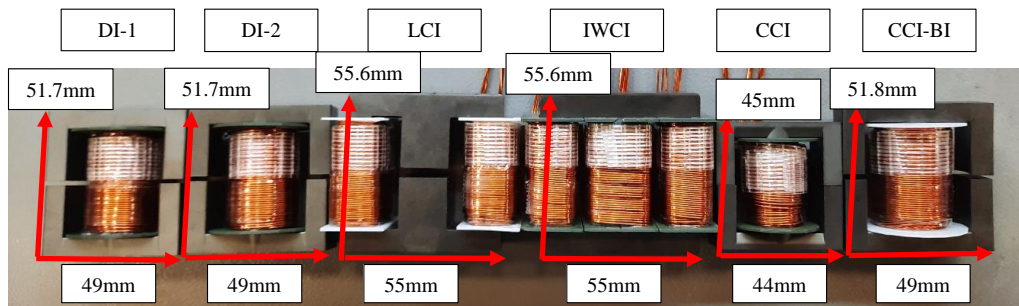


Figure 6.8: Implemented inductor prototypes

6.4 Other Components of the Converter

The other components of the converter were selected by considering voltage and current ratings. The selected components are summarized in Table 6.10.

Table 6.10: Other Components of the Converter

Component	Part Number	Manufacturer
Main Mosfet	C3M0060065K [43]	Wolfspeed
Diode	C3D20065D [44]	Wolfspeed
Output Capacitor	EKWA451ELL470MJ45S [45]	Nippon Chemicon
Gate Driver	UCC21520 [46]	Texas Instruments
Driver Power Supply	R12P21503D [47]	Recom
Digital Controller	TMS320F28069 [48]	Texas Instruments

6.5 Power Loss Analysis

In this section, power loss calculations of the converters with different inductor topologies are conducted. Converter power losses consist of conduction and switching losses of the main MOSFETs, P_{cond} and $P_{switching}$, diode losses, P_{diode} , winding and core losses of the inductor, $P_{winding}$ and P_{core} and gate drive losses, P_{drive} . Before calculations of losses, parameters of the converters with different inductors are given in Table 6.11.

Table 6.11: Parameters of the Converters with Designed Inductors

	LCI	IWCI	CCI	DI
Average Phase Current(A)	6.66	6.66	6.66	6.66
Peak to Peak Inductor Current Ripple(A)	1.7	1.7	1.7	5
RMS Phase Current(A)	6.68	6.68	6.68	6.82

Conduction losses of main MOSFETs are calculated by using Eq. 3.12. On state resistance of MOSFETs are given in MOSFETs datasheets as $45m\Omega$.

Switching losses of main MOSFETs are calculated by using Eq. 3.11. E_{on} , E_{off} and E_{oss} values are taken from the datasheet of the MOSFETs. The manufacturer provides the graphs of these switching energies as a function of current, voltage and gate resistance as shown in Fig. 6.9. By using these graphs for our operating conditions

switching energy values can be calculated.

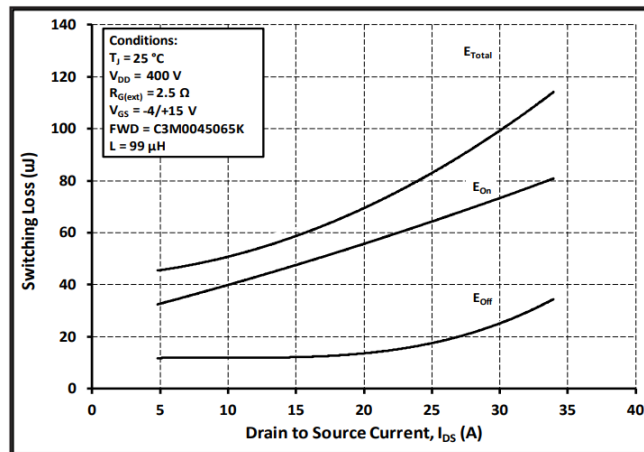


Figure 6.9: Clamped Inductive Switching Energy vs. Drain Current (VDD = 400V) [43]

Diode losses of the converters can be calculated by using Eq. 3.13. The voltage drop, capacitance stored energy constants are provided in the datasheet of diodes.

Gate drive losses of the converter can be calculated by using Eq. 3.14. Driver supply losses are calculated by using the efficiency of driver supply provided in the datasheet and current drawn by the gate driver.

Winding losses of the inductor can be divided into two components. One of them is DC winding losses due to the DC current flowing through the DC winding resistance. The other one is used for representing high-frequency losses of the inductor. As stated in Chapter 3, at high-frequency operation, AC resistance of the windings increases exponentially because of the skin effect and the proximity effect [49] and hence the winding losses increase. The skin depth of copper at 50kHz can be calculated by using the formula provided in [50]. The skin depth of copper at 50kHz is calculated as 0.292 mm. The radius of copper used in inductors is 0.325 mm which yields a conductor depth to skin depth ratio near to 1.

In order to take into account high frequency effects of winding losses, winding resistances are measured by using impedance analyzer Bode 100 [51]. The resistance results @50kHz given in Table 6.9 are used for the calculation of AC winding losses. Even though the high-frequency resistance measurement results might not be accu-

rate since AC components of the currents of the inductors are considerable small, AC winding losses will not be significant. However, for more accurate calculation of winding losses or for transformers where current only has AC component the proximity effect should be considered by using FEA simulations.

The exponents in the Steinmetz equation are calculated by using the core loss vs frequency, magnetic flux density graph of magnetic material which is shown in Fig. 6.10. Steinmetz equations with derived exponents is given in Eq. 6.9. As stated in Chapter 3, core loss calculation with Steinmetz equations does not consider the DC bias effect. In this chapter, DC bias effect is considered with the help of FEA simulations. In the FEA simulations, inductor current excitations were applied as both DC and AC components of current. Besides, only the AC component of the current was applied and the effect of dc bias was examined. FEA simulations were also repeated with the 2D model and the results for the LCI are given in Table 6.12. Moreover, the formula shown in Eq. 6.10 and proposed in [52] is used to find the equivalent frequency of the magnetic flux density. This formula calculates the sinusoidal equivalent frequency of a rectangular AC excitation. This frequency is used in the core loss formula given in Eq. 6.9.

$$P_v = 1.115 \cdot f^{1.145} \cdot \left(\frac{\Delta B}{2}\right)^{2.738} \quad (6.9)$$

where, P_v is the core loss per volume in W/m^3 , f is the frequency in Hz and ΔB is the peak to peak magnetic flux density on the core in Tesla.

$$f_{eq} = \frac{2}{B_{pp}^2 \pi^2} \int_T \left(\frac{dB}{dt}\right)^2 dt \quad (6.10)$$

Applying Eq. 6.10 for LCI yields, f_{eq} as 43.2kHz. Moreover, the AC flux component on the center leg of the LCI is very small when compared to AC flux on the outer legs. Therefore, during core loss calculation volume of the center leg can be subtracted from the volume of the core.

As can be seen from Table 6.12, core loss decreases with DC bias in the FEA results. Also, analytically calculated core loss by using equivalent frequency gives a result close to the 3D FEA result with the DC component of current is not applied. This

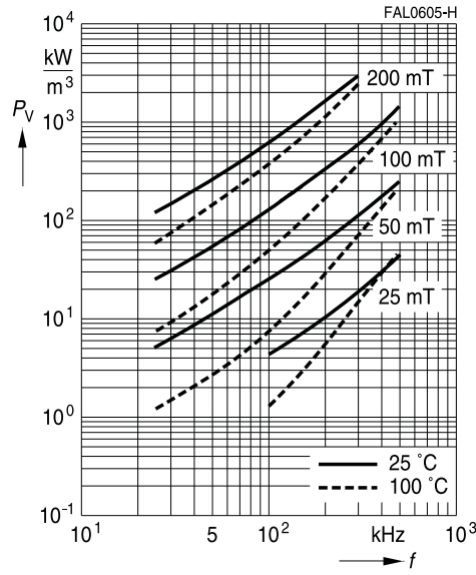


Figure 6.10: Core loss per volume as a function of frequency and magnetic flux density [53]

confirms that analytical calculations using the Steinmetz equation do not consider the DC bias effect and it gives more accurate results when calculated with equivalent frequency.

The results of equivalent frequencies of all inductors and core loss results of all inductor simulated in 3D FEA in order to consider the DC bias effect are given in Table 6.13.

Table 6.12: Core Loss Results for LCI

	2D with DC=0	2D with DC≠0	3D with DC=0	3D with DC≠0	Analytical Calculation using f_{eq}
Core Loss	0.267W	0.287W	0.348W	0.285W	0.38W

Fig. 6.11 shows theoretically calculated power losses of the converters with coupled inductor topologies and discrete inductors at full load of minimum input voltage condition. A breakdown of theoretical power losses of converters with LCI, IWCI, CCI and DI are given in Fig. 6.12a, Fig. 6.12b, Fig. 6.13a and Fig. 6.13b, respectively.

Table 6.13: Core Loss Results for Inductors

	3D with DC \neq 0	Analy. Calc. using $f = f_{eq}$	Analy. Calc. using $f = f_{sw}$
LCI	0.285W	0.36W	0.46W
IWCI	0.321W	0.63W	0.78W
CCI-BI	0.015W	0.004W	0.005W
CCI	4.06W	3.78W	4.7W
DI	0.188W	0.217W	0.268W

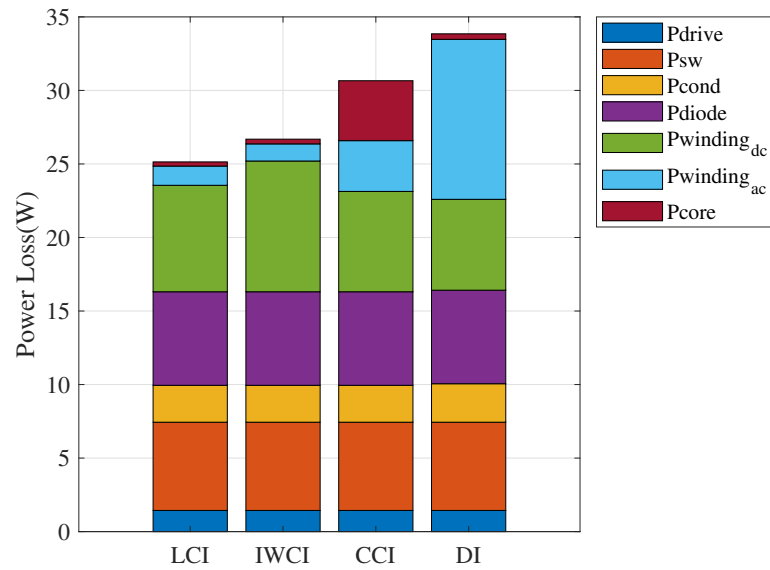


Figure 6.11: Theoretical calculated power losses of converters with various inductor topologies

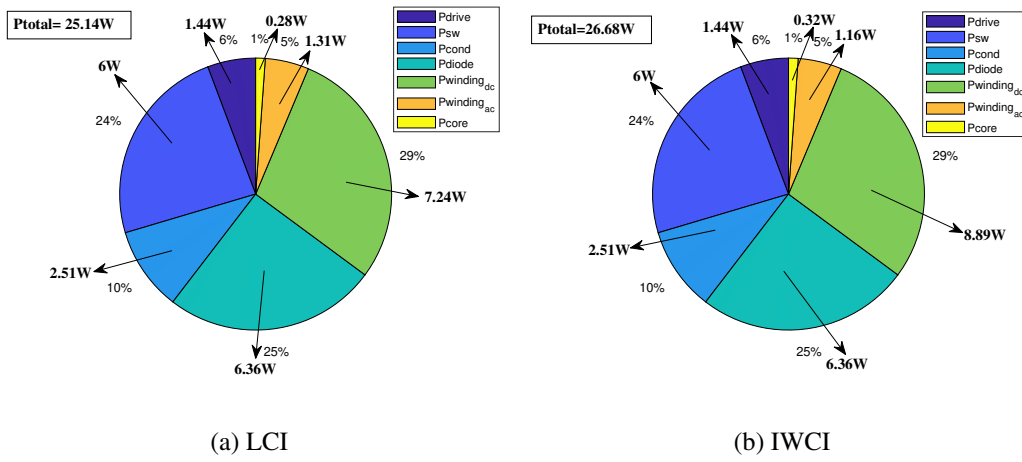


Figure 6.12: Breakdown of power losses of converters with different inductors-1

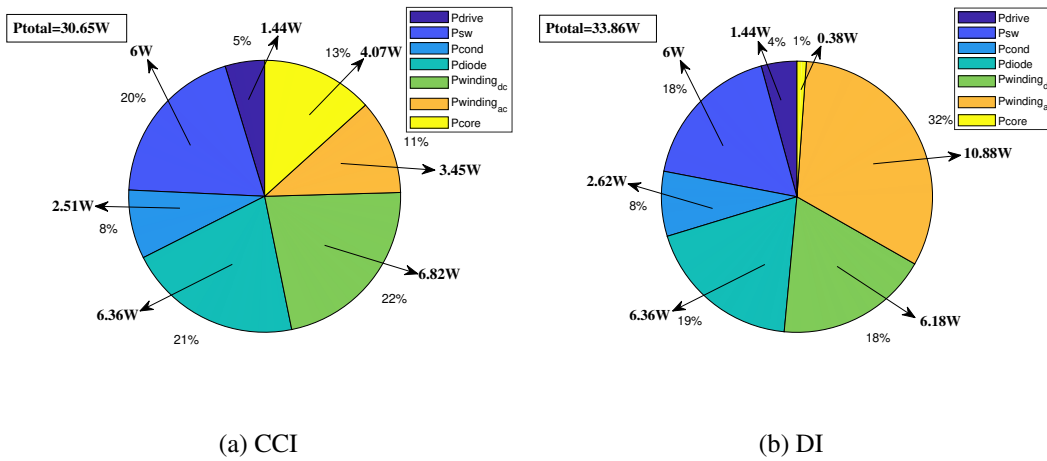


Figure 6.13: Breakdown of power losses of converters with different inductors-2

6.6 Control Loop Design

As stated in [54], modeling of the coupled inductor topology as self and mutual inductances is well suited when the leakage inductance of the coupled inductors does not play a determinant role in the converter operation. The change of topology does not play an important role in closed-loop operation of the converter. The experimental results show that all converters have similar responses. Therefore, transfer function derivation of the converter is done for only IWCI.

6.6.1 Small-signal Modeling of the Converter

The small-signal model of a two-phase interleaved boost converter with IWCI is done by using the averaged switch model. Averaged switch model proposed by Erickson [55], replaces the converter switches with an equivalent averaged switch model. In this way, time-dependent switching of the circuit is eliminated, [54]. The resulting equivalent circuit of the converter can then be perturbed and linearized to obtain a small-signal model. In the next section, this method will be applied to the two-phase interleaved boost converter with IWCI.

6.6.2 Averaged Switch Modelling of the Boost Converter with IWCI

Derivations of averaged model and transfer functions of a two-phase interleaved boost converter with IWCI are given in Appendix A.2. The derived averaged model of two-phase interleaved converter with IWCI is shown in Fig. 6.14.

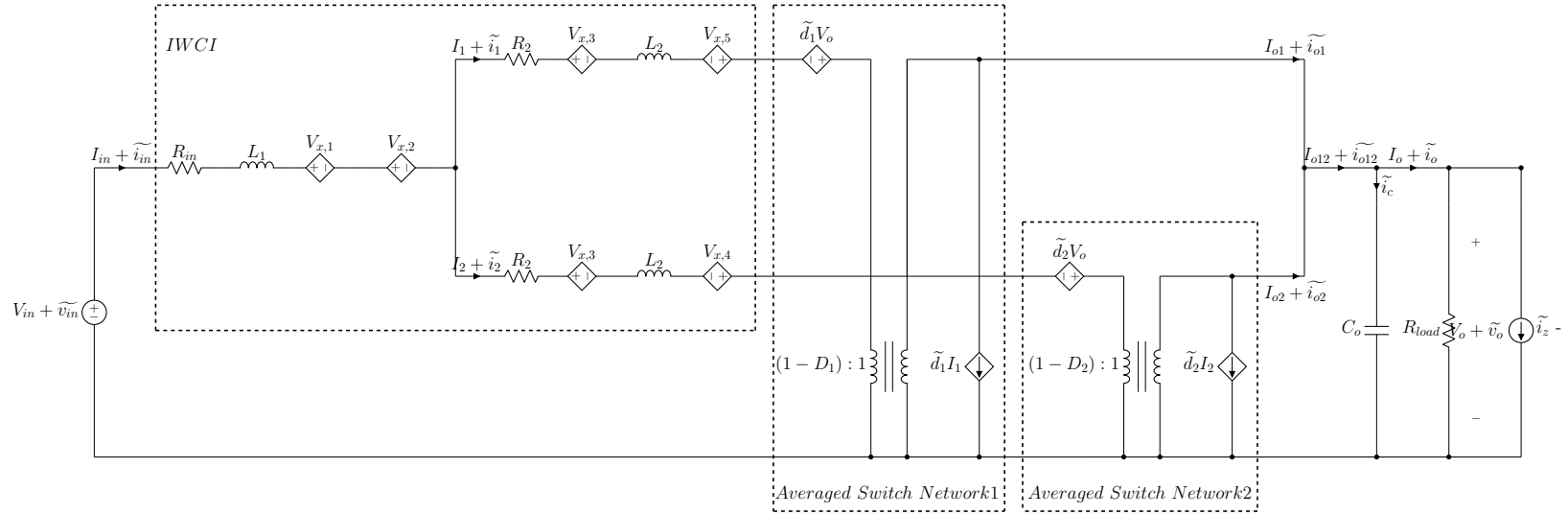


Figure 6.14: DC and small-signal averaged model of a two-phase interleaved boost converter with IWCI

Controlled voltage sources can be expressed as:

$$\begin{aligned}
 V_{x,1} &= L_{m1} \frac{d(I_1 + \tilde{i}_1)}{dt} & V_{x,2} &= L_{m1} \frac{d(I_2 + \tilde{i}_2)}{dt} & V_{x,3} &= L_{m1} \frac{d(I_{in} + \tilde{i}_{in})}{dt} \\
 V_{x,4} &= L_{m2} \frac{d(I_1 + \tilde{i}_1)}{dt} & V_{x,5} &= L_{m2} \frac{d(I_2 + \tilde{i}_2)}{dt}
 \end{aligned} \tag{6.11}$$

Now, by using Equations A.9, A.10 and A.11 the small-signal model of the IWCI interleaved boost converter can be represented in state-space form as:

$$\dot{\tilde{\mathbf{x}}} = \mathbf{A}\tilde{\mathbf{x}} + \mathbf{B}\tilde{\mathbf{u}} \quad \tilde{\mathbf{y}} = \mathbf{C}\tilde{\mathbf{x}} + \mathbf{D}\tilde{\mathbf{u}} \quad (6.12)$$

where the state vector, $\tilde{\mathbf{x}}$, contains the small-signal components of the phase currents flowing through the IWCI outer windings and the voltage across the output capacitor. The input vector, $\tilde{\mathbf{u}}$, contains the control inputs of each phase and the load disturbance current. The output vector, $\tilde{\mathbf{y}}$, comprises the output of the converter of phase currents and output voltage.

$$\mathbf{x} = \begin{bmatrix} \tilde{i}_1 & \tilde{i}_2 & \tilde{v}_o \end{bmatrix}^T \quad \mathbf{u} = \begin{bmatrix} \tilde{d}_1 & \tilde{d}_2 & \tilde{i}_z & \tilde{v}_{in} \end{bmatrix}^T \quad \mathbf{y} = \begin{bmatrix} \tilde{i}_1 & \tilde{i}_2 & \tilde{v}_o \end{bmatrix}^T \quad (6.13)$$

$$\mathbf{A}_{3 \times 3} = \begin{bmatrix} a_{11} & a_{12} & a_{13} \\ a_{21} & a_{22} & a_{23} \\ a_{31} & a_{32} & a_{33} \end{bmatrix} \quad \mathbf{B}_{3 \times 4} = \begin{bmatrix} b_{11} & b_{12} & b_{13} & b_{14} \\ b_{21} & b_{22} & b_{23} & b_{24} \\ b_{31} & b_{32} & b_{33} & b_{34} \end{bmatrix} \quad \mathbf{C}_{3 \times 3} = \begin{bmatrix} 1 & 0 & 0 \\ 0 & 1 & 0 \\ 0 & 0 & 1 \end{bmatrix} \quad (6.14)$$

The D matrix is a 0 matrix. The elements of the state, input and output matrices are given in Appendix A.2.

By the use of Eq. 6.15, the G[s] matrix transfer functions of the state-space model can be found. These are listed in Table 6.14. Mathematica software is used in order to obtain algebraic transfer functions. From the G[s] matrix inputs, it was found that the transfer functions for each of the converter phases are identical.

$$\mathbf{G}[s] = \mathbf{C}(s\mathbf{I} - \mathbf{A})^{-1}\mathbf{B} + \mathbf{D} \quad (6.15)$$

Table 6.14: G[s] Matrix, Transfer Functions of State-space Model

	\tilde{d}_1	\tilde{d}_2	\tilde{i}_z	\tilde{v}_{in}
\tilde{i}_1	$\mathbf{G}_{d1i1}(s) = \frac{\tilde{i}_1}{\tilde{d}_1}$	$\mathbf{G}_{d2i1}(s) = \frac{\tilde{i}_1}{\tilde{d}_2}$	$\mathbf{G}_{izi1}(s) = \frac{\tilde{i}_1}{\tilde{i}_z}$	$\mathbf{G}_{vini1}(s) = \frac{\tilde{i}_1}{\tilde{v}_{in}}$
\tilde{i}_2	$\mathbf{G}_{d1i2}(s) = \frac{\tilde{i}_2}{\tilde{d}_1}$	$\mathbf{G}_{d2i2}(s) = \frac{\tilde{i}_2}{\tilde{d}_2}$	$\mathbf{G}_{izi2}(s) = \frac{\tilde{i}_2}{\tilde{i}_z}$	$\mathbf{G}_{vini2}(s) = \frac{\tilde{i}_2}{\tilde{v}_{in}}$
\tilde{v}_o	$\mathbf{G}_{d1vo}(s) = \frac{\tilde{v}_o}{\tilde{d}_1}$	$\mathbf{G}_{d2vo}(s) = \frac{\tilde{v}_o}{\tilde{d}_2}$	$\mathbf{G}_{izvo}(s) = \frac{\tilde{v}_o}{\tilde{i}_z}$	$\mathbf{G}_{vinvo}(s) = \frac{\tilde{v}_o}{\tilde{v}_{in}}$

6.6.3 Validation of Averaged Model

A mathematical model of a dynamic system should have the same response both in a steady state and during transients when compared to the real system. Thus, a model can be verified by comparing its response to that of the real system. In order to validate the performance and the accuracy of the averaged model obtained in Section 6.6.2, a simulation in Plexim is performed with both switched model and averaged model. The steady-state and transient analyzes are done. Fig. 6.15 shows the waveforms of switched IWCI converter and averaged IWCI converter waveforms. As can be seen, the averaged network has the same response as the switched model which confirms the model and mathematical analyzes.

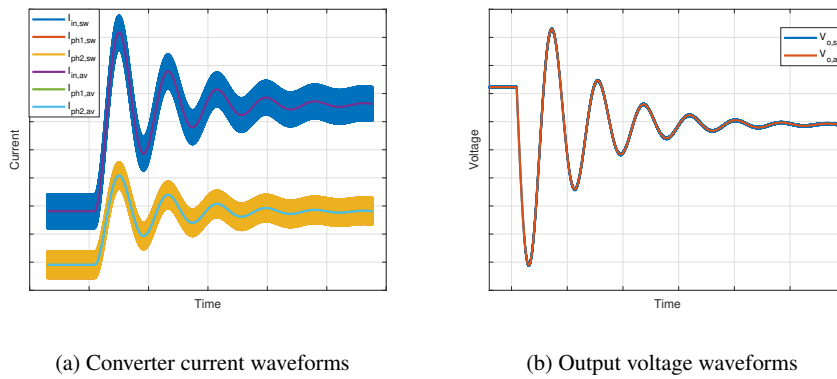


Figure 6.15: Steady-state and transient response of switched and averaged IWCI boost converter

6.6.4 Control Loop Parameters Calculation

In this section, the parameters of the control loop of the converter are calculated. The block diagram of closed-loop two-phase interleaved boost converter is given in Fig. 6.16. Where G_{cv} represents the controller of the voltage loop. $G_{ci,1}$ and $G_{ci,2}$ represent the controller of the current loops of phase 1 and phase 2, respectively. Firstly, the controller of the current loops is designed. The cut-off frequency is selected as one-tenth of the switching frequency as 5kHz. Bode plot of phase current to duty cycle, G_{di1} , bode plot of current loop controller, $G_{ci,1}$ and overall open loop bode plot

CHAPTER 7

EXPERIMENTAL RESULTS

This chapter presents the experimental results of the two-phase boost converters with various coupled inductor topologies and discrete inductors. A 2kW two-phase interleaved boost converter prototype having 150-250VDC input and 400VDC output voltage, and 50kHz switching frequency is implemented as shown in Fig. 7.1. Converters with different inductor topologies are achieved by connecting the implemented inductors to the inductor connection terminal of the board. The experimental setup is presented in Fig. 7.2.

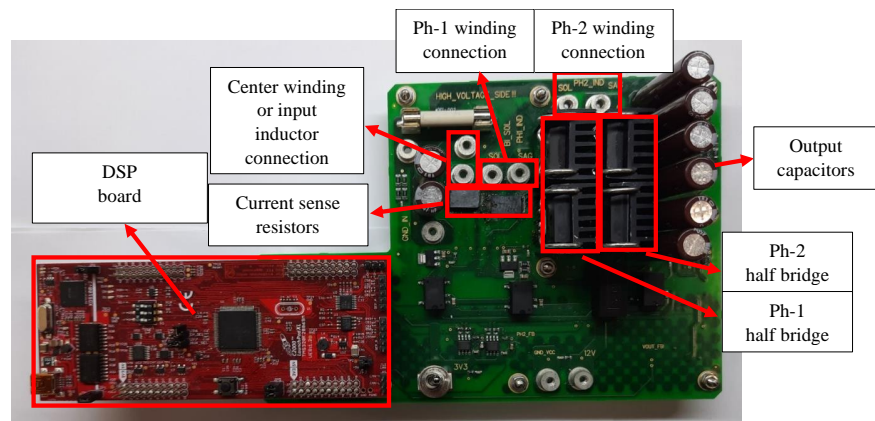


Figure 7.1: Two-phase interleaved boost converter board

7.1 Test Results of Converters

Firstly, voltage and current waveforms of the converter with different inductor topologies are measured. Fig. 7.3 shows the turn-on of the converter with IWCI. As can be seen, a digital soft-start is implemented. The turn on time of the converter is measured

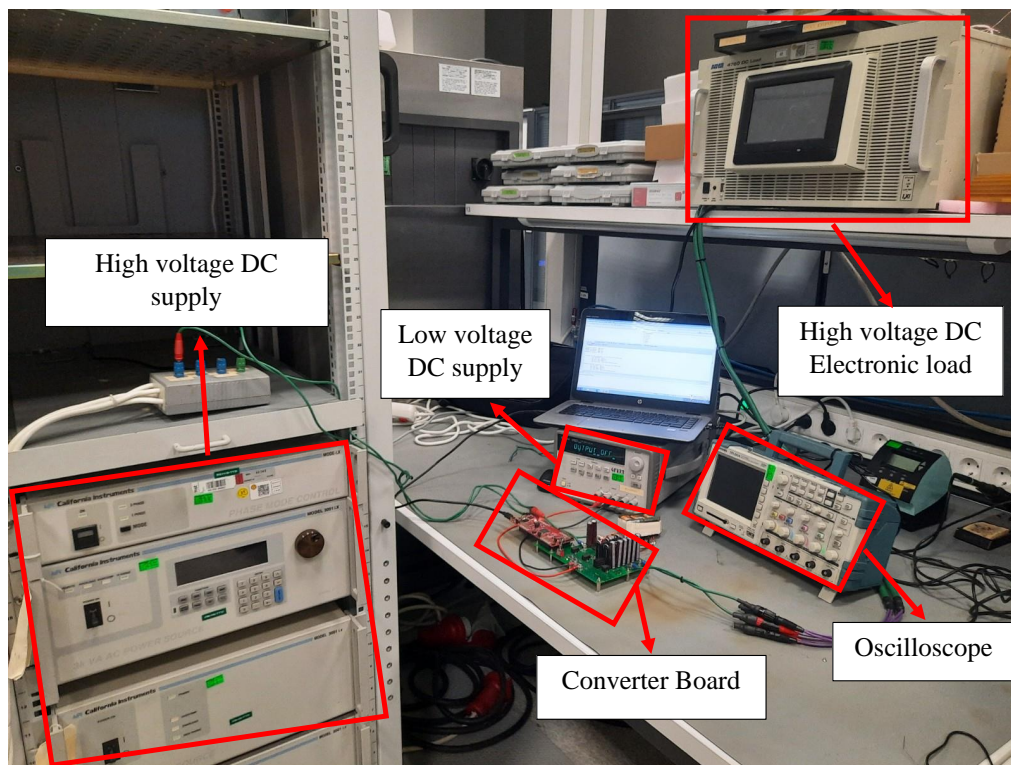


Figure 7.2: Experimental Setup

as 384ms.

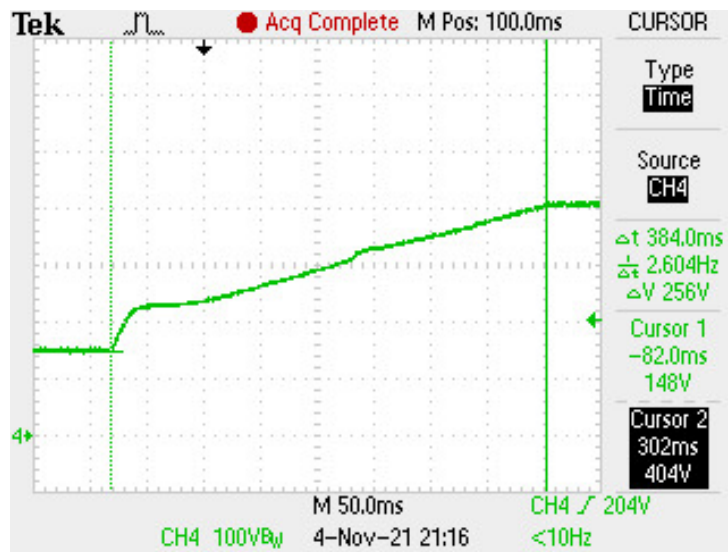
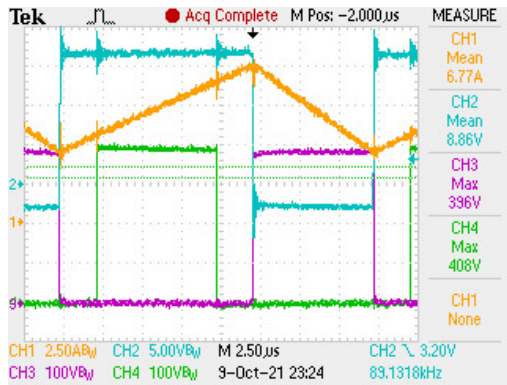


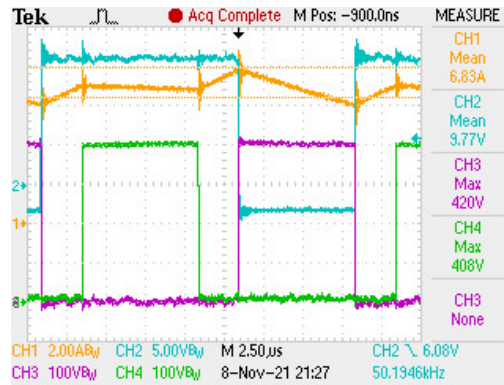
Figure 7.3: Output voltage start-up of the converter with IWCI

Fig. 7.4 shows the critical waveforms of an interleaved boost converter with different inductor topologies at full load conditions for the minimum input voltage. As can be seen, coupled inductor and interleaved operations are achieved. Phase1 inductor waveforms have seen different inductance values for entire switching period. Fig. 7.5 shows the current waveforms of an interleaved boost converter with different inductor topologies at full load conditions for the minimum input voltage. As can be seen, all converters have nearly the same input current ripple and inductor current ripple values. The only exception is that discrete inductors have larger inductor current ripples. As mentioned before, it is impossible to adjust input and inductor current ripple at the same time by using discrete inductors. Measured ripple values are summarized in Table 7.2.

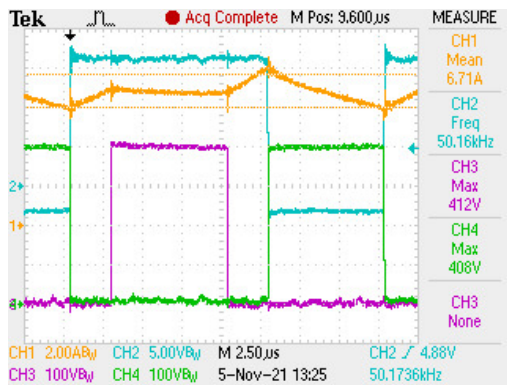
Fig. 7.6 shows the voltage ripple waveforms of an interleaved boost converter with different inductor topologies at full load conditions for the minimum input voltage. As can be seen, all converters nearly have the same output voltage ripple except discrete inductors. As mentioned before, in a boost converter most of the output voltage ripple magnitude comes from the product of capacitor ripple current and series resistance of output capacitor, ESR. Capacitor current ripple is the same as ripple inductor peak current. Since the discrete inductor design has a higher inductor current ripple,



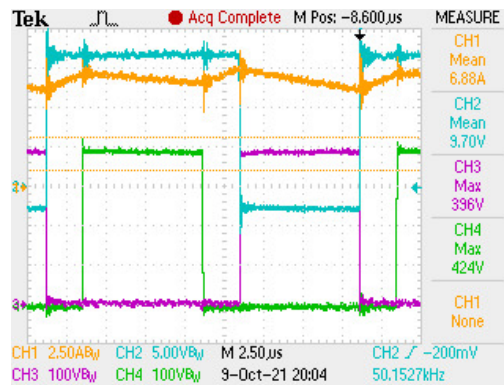
(a) DI



(b) LCI

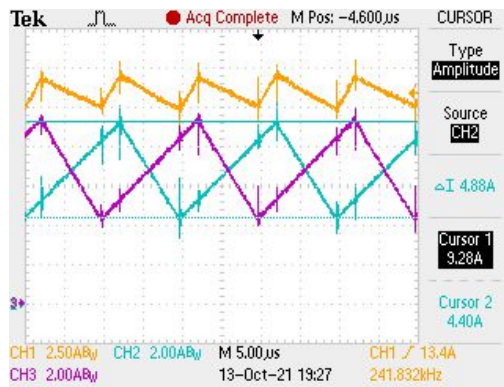


(c) IWCI

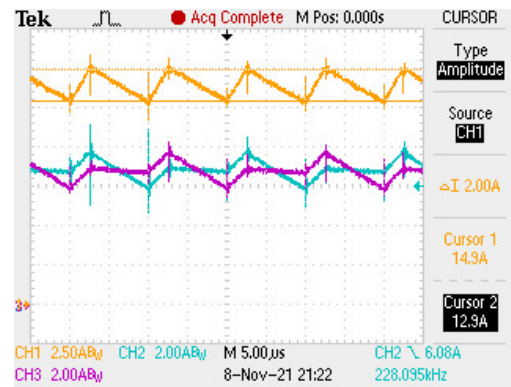


(d) CCI

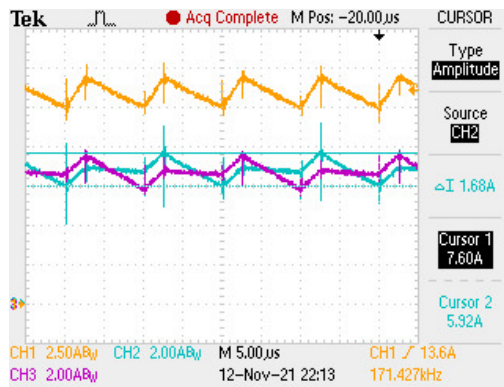
Figure 7.4: Critical waveforms through the module at critical load and minimum input voltage ($D=0.625$): CH1 (orange) = $I_{LP_{h1}}$, CH2 (blue) = V_{gs} of PH1 Mosfet, CH3 (purple) = V_{DS} of PH1 mosfet, CH4 (green) = V_{DS} of PH2 mosfet



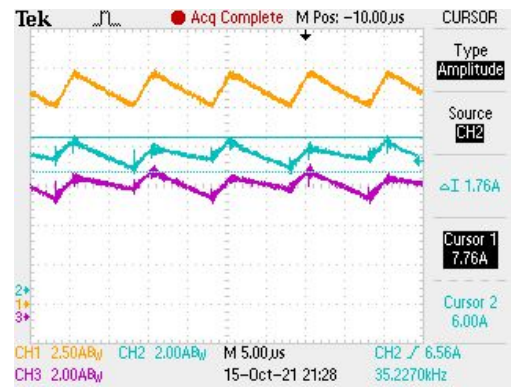
(a) DI



(b) LCI



(c) IWCI



(d) CCI

Figure 7.5: Current waveforms of the converter for minimum input voltage and full load operating point ($D=0.625$) : CH1 (orange) = I_{in} , CH2 (blue) = I_{LP1} , CH3 (purple) = I_{LP2} .

the output voltage ripple value is higher than the others. Measured ripple values are summarized in Table 7.2.

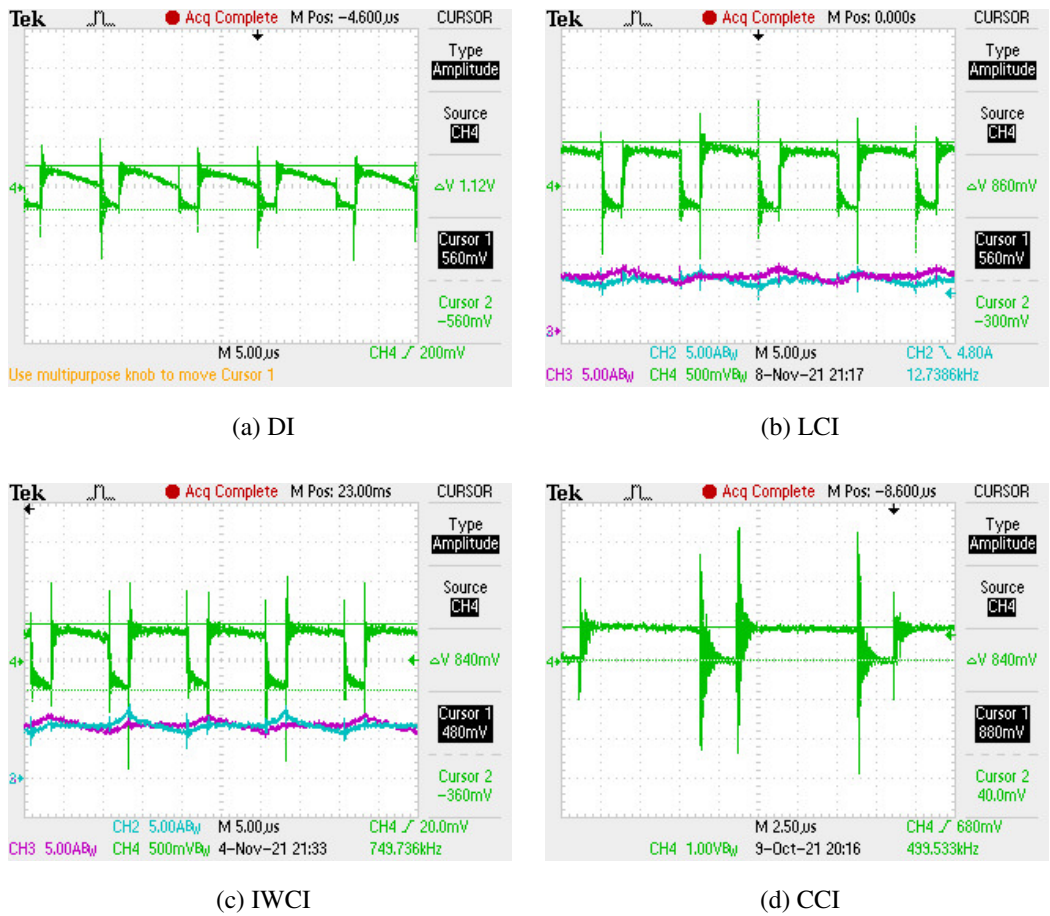


Figure 7.6: Output voltage ripple at minimum input voltage and full load, CH4 (green) = V_{out} (AC Coupled)

7.2 Transient Test Results

In this section, open loop and closed loop transient results of the converter with IWCI and LCI are presented. As it will be seen, all converters have the same transient response. Therefore, the results are provided for an only converter with IWCI and LCI. Open loop transient responses to the load changes of the converter with LCI are given in Fig. 7.7. As can be seen, there are large overshoots and undershoots on the current waveforms of the converter during load transients. Also, the error of current

sharing between the phases of the converter is high. Therefore, a closed loop control of the converter is necessary.

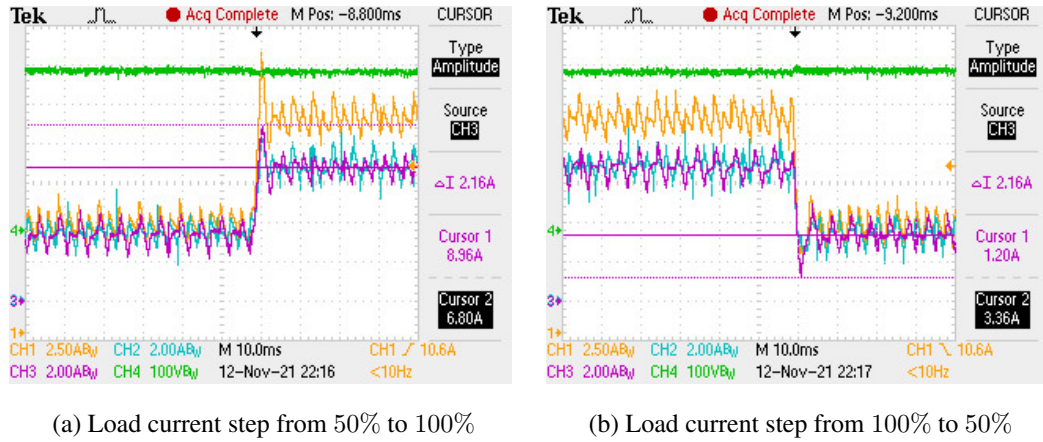


Figure 7.7: Load transient of the converter with LCI, CH1 (orange) = I_{in} , CH2 (blue) = I_{LP1} , CH3 (purple) = I_{LP2} , CH4 (green) = V_{out}

The digital control of the two-phase interleaved boost converter is done by using the average current mode control. In this method, there are 3 different control loops. One of them is the voltage loop that is common for both phases. The others are the current loops of both phases. For control circuits, output voltage and phase currents are sensed. Measured signals are read in the middle of the PWM signal by using ADC. In this way, the average value of the currents is read. The control algorithm timings are given in Fig. 7.8. CH2 represents the gate signal of phase 1 MOSFET. As stated before, the ADC starts to read sensed signals in the middle of CH1. When ADC conversion ends, CH1 is set as high. As can be seen, ADC conversion time is calculated as 1.6 μ s. ADC end of conversion, EOC triggers an interrupt. In this interrupt, an algorithm that is about no-load regulation is running at first. Whenever the calculation of this algorithm is finished, the CH3 signal is set as high. As can be seen, these calculations take 7.5 μ s. Finally, control loops are executed and new duty cycles are calculated and updated. Following that CH3 signal is set as low. As can be seen, these calculations take 2.5 μ s. The total time consumption of the closed loop control is about 11.6 μ s.

Closed loop transient responses of the converter with IWCI and LCI for step load

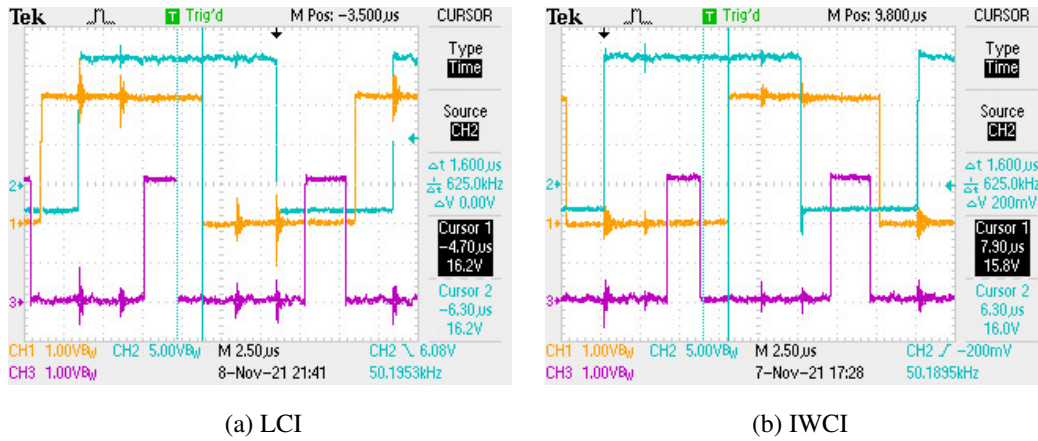


Figure 7.8: Timings of control algorithm, CH1 (orange) = ADC EOC, CH2 (blue) = VGS of Ph1 mosfet, CH3 (purple) = End of calculations in the ISR.

changes are given in Fig. 7.9 and Fig. 7.10. As can be seen, there are no overshoots or undershoots in the currents during load transients. Also, the current sharing error is reduced which is important for avoiding magnetic core saturation in the coupled inductors and to obtaining equal thermal stress for the phases of interleaved boost converter.

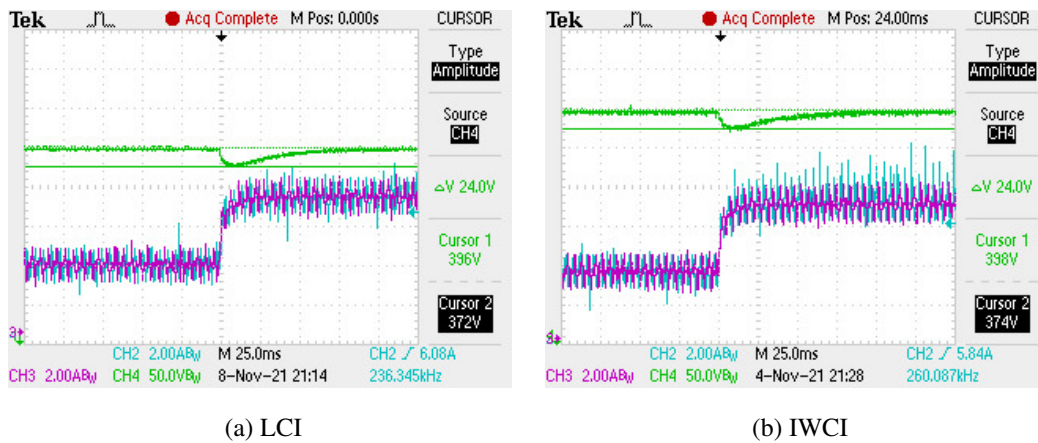
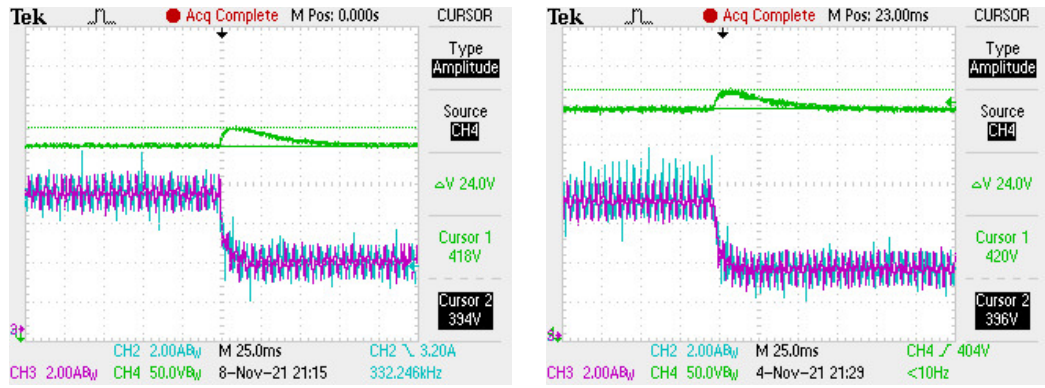


Figure 7.9: Load current step from 50% to 100%, CH1 (orange) = I_{in} , CH2 (blue) = I_{LPh1} , CH3 (purple) = I_{LPh2} , CH4 (green) = V_{out}

As stated before, an algorithm was developed in order to avoid over-voltage breakdown. For no-load operation, it limits the duty cycle of the boost converter otherwise

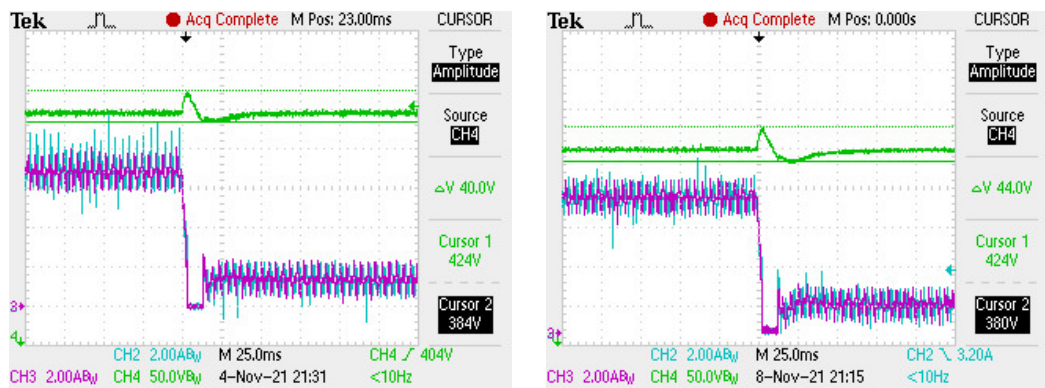


(a) LCI

(b) IWCI

Figure 7.10: Load current step from 100% to 50%, CH1 (orange) = I_{in} , CH2 (blue) = $I_{LP_{h1}}$, CH3 (purple) = $I_{LP_{h2}}$, CH4 (green) = V_{out}

even small change in duty cycle results in a sudden increase in the output voltage. Moreover, for large load step-down transients, due to the large energy stored in the output capacitor, the output voltage rises to high levels exceeding the limits. Therefore, the controller checks the output voltage during every control interrupt and whenever it exceeds the predefined limit converter stops switching. When the voltage goes back to the limit the converter starts switching again. Fig. 7.11 shows the large load step-down transients and the response of the converter to that.



(a) IWCI

(b) LCI

Figure 7.11: Load current step from 100% to 20%, CH1 (orange) = I_{in} , CH2 (blue) = $I_{LP_{h1}}$, CH3 (purple) = $I_{LP_{h2}}$, CH4 (green) = V_{out}

7.3 Volume Comparison

As can be seen from experimental results, all inductor topologies have the same desired input current ripple and output voltage ripple values which confirm theoretical expectations. After the validation of converters with all coupled inductor topologies and discrete inductors, a comparative analysis of inductors is done. In order to compare performances of inductors, a figure of merit (FoM) is proposed based on converters efficiency, volume and weight. The FoM is defined in below:

$$FoM = \frac{1}{Power\ Loss(W) \cdot Inductor\ Volume(m^3) \cdot Inductor\ Weight(g)} \quad (7.1)$$

Volumes of the inductors are measured by measuring the amount of overflowing alcohol after the inductor was removed from the alcohol-filled in a glass. A measurement setup for inductors volume is shown in Fig. 7.12. Volume and weight measurement results of inductors are summarized in Table 7.2. As can be seen, DI and CCI have the lowest volume, whereas LCI and IWCI have higher efficiencies than the others. In terms of weight, LCI and CCI have the best results.



Figure 7.12: Volume measurement of IWCI

7.4 Efficiency Comparison

In this section efficiency results of the converters are provided. Efficiency graphs are drawn for three different input voltages and for low load and high load conditions,

separately. The efficiency graphs are shown in Fig. 7.13, Fig. 7.14 and Fig. 7.15. The results show that all topologies with coupled inductors have a better efficiency compared to the converter with discrete inductors. IWCI and LCI topologies are found to have better efficiencies than the other inductors at all conditions. The results show that as the input voltage increases, the efficiencies of converters increase. This is as a result of a decrease in the conduction losses as current decreases.

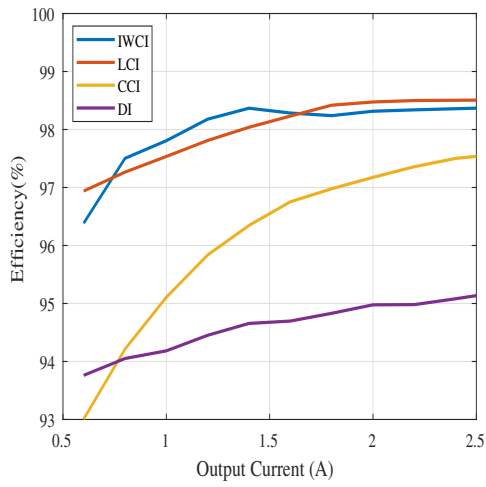
7.4.1 Measurement Uncertainty

As the measurement devices have accuracy deviations, measurement errors can be calculated from the accuracy specified in the datasheet of the measurement device. In this study, efficiencies are calculated by measuring output voltage across the output terminal, input voltage across the input terminal and phase currents across the sense resistors with the same multimeter Fluke 187 [56]. The measurement accuracy formula is given in the datasheet of Fluke 187 as below.

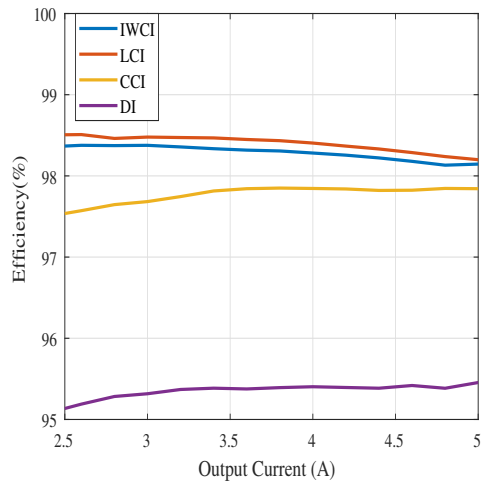
$$\text{Measurement Accuracy} = \pm(\% \text{ of reading} \pm \text{ number of digits}) \quad (7.2)$$

In this equation % of reading and number of digits are depended on the voltage range of the measured signal. For example, for input and output voltage levels these numbers are given as $0.1\% \pm 2$. While for the measurement of voltage drop on the sense resistors these numbers are given as $0.025\% \pm 10$. As can be seen from Table 7.2, the efficiencies of LCI and IWCI are close to each other. Therefore, measurement accuracy is calculated. The calculation is done as it will give the worst-case scenario of accuracy. For LCI, in order to find minimum efficiency with accuracy error, input voltage and current measurement results increased and output voltage measurement results decreased by the measurement accuracy calculated from Eq. 7.2. On the other hand, for IWCI, in order to find maximum efficiency result considering accuracy, input voltage and current measurement results of IWCI decreased and output voltage measurement result of IWCI increased by the measurement accuracy. After the accuracy correction calculated by mentioned method, the efficiency of the converter with LCI decreased from 98.199% to 97.941%. The efficiency of the converter with IWCI increased from 98.145% to 98.404%. Therefore, for measurement results that are close to each other LCI and IWCI topologies can not be accurately compared. A

calorimeter can be used to measure the efficiencies.

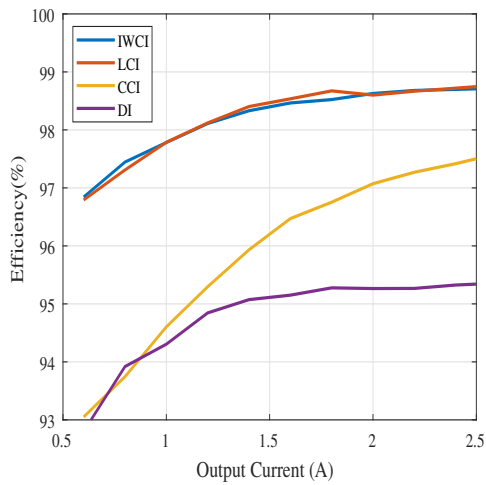


(a) Load current from 10% to 50%

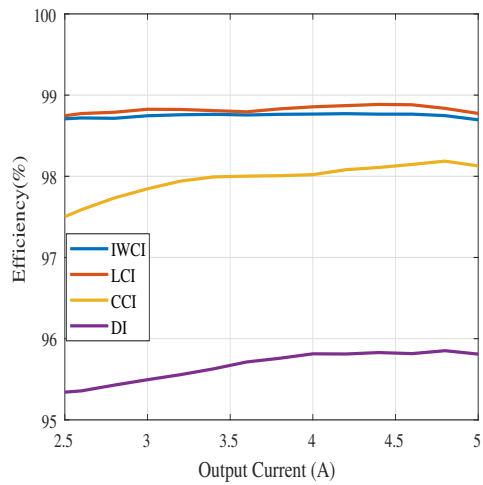


(b) Load current from 50% to 100%

Figure 7.13: Efficiency results for $V_{in} = 150V$



(a) Load current from 10% to 50%



(b) Load current from 50% to 100%

Figure 7.14: Efficiency results for $V_{in} = 200V$

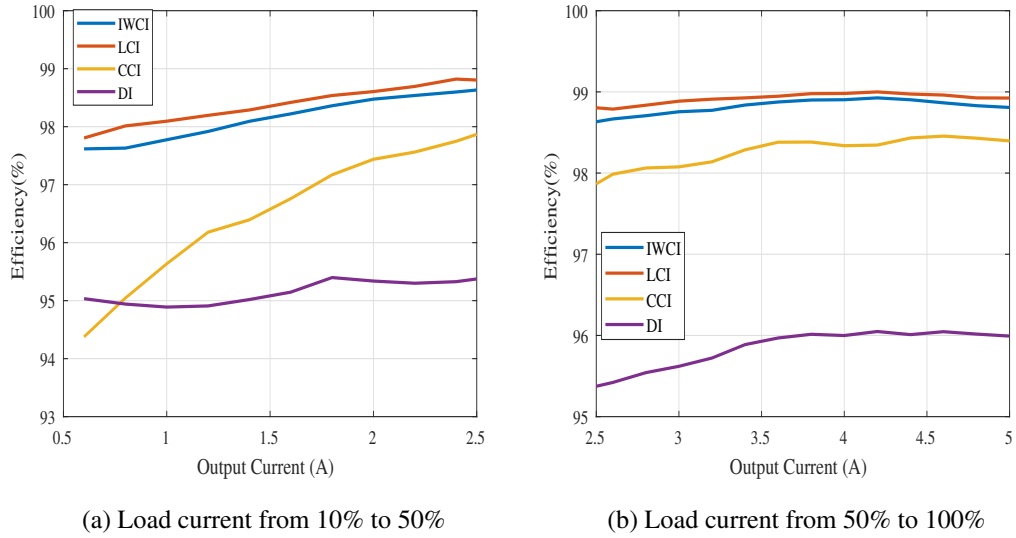


Figure 7.15: Efficiency results for $V_{in} = 250V$

Table 7.1: Performance Comparison for the Boost Converter Equipped with DI, LCI, IWCI and CCI

	DI	LCI	IWCI	CCI
Efficiency (@Max. load,min. V_{in})	95,455%	98,199%	98,145%	97,842%
Power Loss (@Max. load,min. V_{in})	95,23W	36,68W	37,8W	44,11W
Input current ripple	$2A_{pp}$	$1,94A_{pp}$	$1,95A_{pp}$	$2A_{pp}$
Output voltage ripple	$1,12V_{pp}$	$0,84V_{pp}$	$0,86V_{pp}$	$0,84V_{pp}$
Weight	336,9gr	323,3gr	330,7gr	134,1gr 189,2gr
Volume	$95cm^3$	$100cm^3$	$105cm^3$	$45cm^3$ $50cm^3$
FoM ($1/W.m^3.g$)	0,328	0,843	0,762	0,738

7.5 Discussions

The results show that converter with LCI has the best FOM among all converters. However, efficiency results of IWCI and LCI are close to each other. When the measurement accuracy is considered the difference between the efficiencies of the converters with these two inductors is less than the worst-case measurement error. Therefore, these measurements should be done by using a calorimeter. Even though the advantage of LCI in terms of efficiency is ignored, it has still the best perfor-

mances based on volume and weight. The main reason for the higher efficiencies of the converters with coupled inductors compared with the converter with discrete inductors is that the AC value of the phase current of the converter with discrete inductors is higher due to the higher inductor current ripple. This results in higher AC winding losses of the inductors and higher conduction losses of the MOSFETs. Therefore, other discrete inductors are designed theoretically to have the same inductor current ripple with the others. The following table summarizes the theoretical design parameters of discrete inductors which are designed for the same input current ripple and the same inductor current ripple.

Table 7.2: Comparison of the Two Different Discrete Inductor Desings

	DI with the same ΔI_{in}	DI with the same ΔI_L
ΔI_L	5A	1.7A
ΔI_{in}	2A	0.68A
I_{rms}	6.82A	6.68A
L	375 μH	1100 μH
N	52	80
$R_{winding}$	76m Ω	130m Ω
B_{peak}	0.31T	0.37T
Core type	ETD 49/25/16	ETD 54/28/19
Core volume	95 cm ³	140 cm ³

As can be seen, in order to obtain the same inductor current ripple with the converters with coupled inductors, discrete inductors need more number of turns which increases the winding resistance. The power loss comparison of discrete inductors designed for 2 different conditions is given in below.

Table 7.3: Power Loss Comparison of the Two Different Discrete Inductor Desings

	DI with the same ΔI_{in}	DI with the same ΔI_L
$P_{winding,dc}$	6.18W	11.53W
$P_{winding,ac}$	10.88W	2.51W
P_{core}	0.38W	0.21W
$P_{conduction}$	2.62W	2.51W
$P_{switching}$	6.5W	6W
P_{total}	34.35W	30.57W

As can be seen from Table. 7.3, even though winding resistance increases the winding loss of the discrete inductors with the same inductor current ripple is less than the winding loss of the discrete inductors with the same input current ripple. Because the RMS current flowing through the inductor is reduced results in fewer AC winding losses. In conclusion, discrete inductors designed to have the same ΔI_L with other coupled inductors have 47% higher volume and 12% lower power loss compared to discrete inductors designed to have the same ΔI_{in} with other coupled inductors. DI with the same ΔI_{in} has 31% higher FOM than the DI with the same ΔI_L .

CCI has a lower number of turns for phase windings which increases the AC magnetic flux density and hence core losses. Therefore, the efficiency of the CCI is lower than the other coupled inductor topologies. Also, the number of turns of LCI and IWCI is different which results in different winding losses for these inductors. In conclusion, for a two-phase interleaved boost converter with a 2kW output power rating, LCI has the best performance outputs, FoM, among all topologies proposed in the literature and discrete inductors for the condition where converter's input and output filter size kept constant.

CHAPTER 8

CONCLUSIONS

Interleaved boost converters are usually built with discrete or uncoupled inductors. Usage of coupled inductors instead of uncoupled inductors is proposed in the literature. Different coupled inductor interleaved boost converter topologies are designed and compared in this thesis. In order to compare the volumes of the converters by considering the effects of inductors only, the design condition was chosen as constant input current ripple and constant output voltage ripple. In this way, the volume of the rest of the converters is kept constant.

In Chapter 3, the impact of the number of phases on volume and efficiency of multi-level interleaved boost converters are investigated. For output power level of 2kW, different multi-phase boost converters with a different number of phases are designed theoretically. Only the converters with discrete (uncoupled) inductors are considered due to the easy analytical calculations. However, the results are expected to be similar for coupled inductor topologies. The selection of components of the converters including magnetic components is done according to operating condition. The designs are conducted under the condition that all converters have the same input current ripple. The performances of the converters with several phases are then compared. It is shown that for the same input current ripple condition and 2kW output power level, 2-phase converter has the best performance among all. The converters are also designed and compared under the condition where the inductance of phase inductors is kept constant. It is found that the condition where the same inductors are used for all design does not plausible since a higher number of phases comes with increased volume. Even, the higher number of phases have less efficiency than 2-phase and single-phase designs. As a result, for a two-phase interleaved boost converter with a

2kW output power level number of phases is selected as 2 to implement converters.

Electrical analyzes of two-phase interleaved boost converters with coupled inductor topologies LCI, IWCI, CCI and as well as discrete inductors, DI, are provided in Chapter 4. Magnetic analyzes of the inductor topologies are presented. Systematic inductor design methodologies are proposed for all inductor topologies. It is shown that the parameters of inductors such as self-inductance and maximum magnetic flux density might be changed after the implementation of inductors due to the fringing fluxes on the air-gaps. Therefore, in this study inductors are modeled with the help of FEA simulations using Ansys Maxwell 3D. The design parameters are then updated according to FEA results. The designed inductors are produced and the magnetic circuit analysis results are validated. The effect of fringing fluxes on the air-gap reluctances is considered analytically by using proposed methods in the literature. The effectiveness of these methods is investigated for the designed inductor topologies by comparing the results with the FEA results and measurements.

Moreover, transfer function derivations of a two-phase interleaved boost converter with IWCI by using the averaged switch model are provided. It was shown that all converters with different inductor topologies have the same closed loop responses. Therefore, the derivation of the transfer functions and the design of the controllers has been done only for a converter with IWCI. The implementation of the converter was studied in detail.

A 50kHz 2kW two-phase interleaved boost converter having 150-250VDC input to 400VDC output is built and is used to demonstrate the performances of designed inductors. It is shown that all inductors have the same input current ripple values. The output voltage ripples of the converter are measured to be in the same range with all inductor topologies except for discrete inductors. In this way, it was confirmed that the converter has the same performance when employed with the designed inductors. The efficiency of the converter is recorded for each inductor topology. The volume and weight of designed inductors are compared. Since the rest of the converter is the same, it means that the volume and weight of converters are compared. In order to evaluate the overall performances of the designed inductors, a figure of merit, FOM, is proposed based on the power losses, volume and weight of the converter. The results

show that all topologies with coupled inductors have a better efficiency compared to the converter with discrete inductors and LCI topology is found to have the best performance among all designs. The contributions of this study to the field can be summarized as below:

- The impact of the number of phases on the multi-phase converters performances is investigated.
- As discussed in Chapter 2, unlike the studies in the literature, coupled inductor topologies and discrete inductors are compared by keeping the rest of the converter the same. In this way, the effect of inductor topology is clearly investigated.
- For each inductor topology a design methodology is proposed. In the literature, the design methodology of the proposed coupled inductors starts with the selection of a magnetic core. In this study, a more systematic design procedure is suggested.
- Effect of fringing fluxes on the inductor parameters is considered during the design stage. Design parameters are updated according to the FEA simulations which give results with less than 1.5% error compared to measurements.
- The effect of the coupling coefficient on the inductor performances is investigated for LCI. It is expected to have the same effect for IWCI.
- Transient results are provided for a digitally controlled two-phase interleaved boost converter with each inductor topology. The results show that inductor topology does not change the response of the converter. This is expected because all inductors nearly have the same equivalent inductances.

8.1 Future Work

Following future works can be suggested.

- The designs conducted in Chapter 3 can be applied for also the coupled inductor topologies to comprehensively evaluate the effect of the phase number on the

converter performance. Different input current ripple values may be chosen to see the change in the performances of designs.

- For higher power ratings than 2kW, a converter with the number of phases of 3, 4 or more can be designed by using the proposed coupled inductor topologies which are suitable for a 2-phase converter or using a novel coupled inductor topology for the converter with the higher number of phases.
- The high-frequency losses of the inductor may be considered by using FEA simulations and numerical calculations. Similarly, the effect of DC bias on the core losses can be investigated experimentally.

REFERENCES

- [1] T. Schoenen, M. S. Kunter, M. D. Hennen, and R. W. De Doncker, “Advantages of a variable dc-link voltage by using a dc-dc converter in hybrid-electric vehicles,” pp. 1–5, 2010.
- [2] N. Elsayad, H. Moradisizkoochi, and O. A. Mohammed, “A study on a three-level flying capacitor boost converter with an integrated lc2d output network for universal input voltage applications,” in *2019 IEEE Applied Power Electronics Conference and Exposition (APEC)*, pp. 2128–2134, 2019.
- [3] G. Fontes, C. Turpin, S. Astier, and T. A. Meynard, “Interactions between fuel cells and power converters: Influence of current harmonics on a fuel cell stack,” *IEEE Transactions on Power Electronics*, vol. 22, no. 2, pp. 670–678, 2007.
- [4] C.-T. Pan, S.-K. Liang, and C.-M. Lai, “A zero input current ripple boost converter for fuel cell applications by using a mirror ripple circuit,” in *2009 IEEE 6th International Power Electronics and Motion Control Conference*, pp. 787–793, 2009.
- [5] S. Kimura, Y. Itoh, W. Martinez, M. Yamamoto, and J. Imaoka, “Downsizing effects of integrated magnetic components in high power density dc–dc converters for ev and hev applications,” *IEEE Transactions on Industry Applications*, vol. 52, no. 4, pp. 3294–3305, 2016.
- [6] P.-L. Wong, P. Xu, P. Yang, and F. Lee, “Performance improvements of interleaving vrms with coupling inductors,” *IEEE Transactions on Power Electronics*, vol. 16, no. 4, pp. 499–507, 2001.
- [7] M. Pavlovský, G. Guidi, and A. Kawamura, “Assessment of coupled and independent phase designs of interleaved multiphase buck/boost dc–dc converter for ev power train,” *IEEE Transactions on Power Electronics*, vol. 29, no. 6, pp. 2693–2704, 2014.

- [8] J. Imaoka, M. Yamamoto, K. Umetani, S. Arimura, and T. Hirano, “Characteristics analysis and performance evaluation for interleaved boost converter with integrated winding coupled inductor,” in *2013 IEEE Energy Conversion Congress and Exposition*, pp. 3711–3718, 2013.
- [9] W. Martinez, S. Kimura, J. Imaoka, M. Yamamoto, and C. A. Cortes, “Volume comparison of dc-dc converters for electric vehicles,” in *2015 IEEE Workshop on Power Electronics and Power Quality Applications (PEPQA)*, pp. 1–6, 2015.
- [10] H. Kosai, S. McNeal, B. Jordan, J. Scofield, B. Ray, and Z. Turgut, “Coupled inductor characterization for a high performance interleaved boost converter,” *IEEE Transactions on Magnetics*, vol. 45, no. 10, pp. 4812–4815, 2009.
- [11] D. Perreault and J. Kassakian, “Distributed interleaving of paralleled power converters,” *IEEE Transactions on Circuits and Systems I: Fundamental Theory and Applications*, vol. 44, no. 8, pp. 728–734, 1997.
- [12] M. Shi, “Design and analysis of multiphase dc-dc converters with coupled inductors,” *Master’s thesis, Texas AM University*, 2003.
- [13] G. Dotelli, R. Ferrero, P. G. Stampino, S. Latorrata, and S. Toscani, “Pem fuel cell drying and flooding diagnosis with signals injected by a power converter,” *IEEE Transactions on Instrumentation and Measurement*, vol. 64, no. 8, pp. 2064–2071, 2015.
- [14] R. Ferrero, M. Marracci, and B. Tellini, “Single pem fuel cell analysis for the evaluation of current ripple effects,” *IEEE Transactions on Instrumentation and Measurement*, vol. 62, no. 5, pp. 1058–1064, 2013.
- [15] Texas Instruments, Texas, USA, *Benefits of a multiphase buck converter*, 2012.
- [16] D. Liang and H.-B. Shin, “Coupled inductor design method for 2-phase interleaved boost converters,” *Journal of Power Electronics*, vol. 19, pp. 344–352, 2019.
- [17] H. G. M. Al Sakka, J. Van Mierlo and U. Brussel, “Dc/dc converters for electric vehicles,” *Electric Vehicles-Modelling and Simulations*, vol. 100, no. 466, 2011.

- [18] S. Chakraborty, H.-N. Vu, M. M. Hasan, D.-D. Tran, M. E. Baghdadi, and O. Hegazy, “Dc-dc converter topologies for electric vehicles, plug-in hybrid electric vehicles and fast charging stations: State of the art and future trends,” *Energies*, vol. 12, no. 8, 2019.
- [19] K. Jyotheeswara Reddy and N. Sudhakar, “High voltage gain interleaved boost converter with neural network based mppt controller for fuel cell based electric vehicle applications,” *IEEE Access*, vol. 6, pp. 3899–3908, 2018.
- [20] F. Sobrino-Manzanares and A. Garrigós, “An interleaved, fpga-controlled, multi-phase and multi-switch synchronous boost converter for fuel cell applications,” *International Journal of Hydrogen Energy*, vol. 40, no. 36, pp. 12447–12456, 2015.
- [21] C. Wang, “Investigation on interleaved boost converters and applications,” in *Defense*, vol. 8, no. 1-65, 2009.
- [22] M. Frivaldsky, J. Morgos, B. Hanko, and M. Prazenica, “The study of the operational characteristic of interleaved boost converter with modified coupled inductor,” *Electronics*, vol. 8, no. 9, 2019.
- [23] P. Magne, P. Liu, B. Bilgin, and A. Emadi, “Investigation of impact of number of phases in interleaved dc-dc boost converter,” in *2015 IEEE Transportation Electrification Conference and Expo (ITEC)*, pp. 1–6, 2015.
- [24] M. Gerber, J. Ferreira, I. Hofsjager, and N. Seliger, “Interleaving optimization in synchronous rectified dc/dc converters,” in *2004 IEEE 35th Annual Power Electronics Specialists Conference (IEEE Cat. No.04CH37551)*, vol. 6, pp. 4655–4661 Vol.6, 2004.
- [25] V. Samavatian and A. Radan, “A high efficiency input/output magnetically coupled interleaved buck–boost converter with low internal oscillation for fuel-cell applications: Ccm steady-state analysis,” *IEEE Transactions on Industrial Electronics*, vol. 62, no. 9, pp. 5560–5568, 2015.
- [26] F. Yang, X. Ruan, Q. Ji, and Z. Ye, “Input dm emi filter design of interleaved crm boost pfc converter with coupled inductor,” in *2011 IEEE Energy Conversion Congress and Exposition*, pp. 2614–2621, 2011.

- [27] P.-L. Wong, Q. Wu, P. Xu, B. Yang, and F. Lee, "Investigating coupling inductors in the interleaving qsw vrm," in *APEC 2000. Fifteenth Annual IEEE Applied Power Electronics Conference and Exposition (Cat. No.00CH37058)*, vol. 2, pp. 973–978 vol.2, 2000.
- [28] L.-P. Wong, Y.-S. Lee, D. Ki-Wai Cheng, and M. Chow, "Two-phase forward converter using an integrated magnetic component," *IEEE Transactions on Aerospace and Electronic Systems*, vol. 40, no. 4, pp. 1294–1310, 2004.
- [29] Y. Itoh, F. Hattori, S. Kimura, J. Imaoka, and M. Yamamoto, "Design method considering magnetic saturation issue of coupled inductor in interleaved ccm boost pfc converter," in *2015 IEEE Energy Conversion Congress and Exposition (ECCE)*, pp. 2616–2621, 2015.
- [30] K. Martín, A. Rujas, I. Villar, I. Perez-de Arenaza, and I. Etxeberria-Otadui, "Design of a 2.5kw pfc boost full-sic converter based on close-coupled inductors," in *2014 IEEE 15th Workshop on Control and Modeling for Power Electronics (COMPEL)*, pp. 1–7, 2014.
- [31] S. Al-Zubaidi, M. Z. Ahmed, and P. Davey, "A novel buck-boost dc-dc converter using close-coupled inductors," in *2015 IEEE 6th International Symposium on Power Electronics for Distributed Generation Systems (PEDG)*, pp. 1–8, 2015.
- [32] J. Imaoka, K. Umetani, S. Kimura, W. Martinez, M. Yamamoto, S. Arimura, and T. Hirano, "Magnetic analysis, design, and experimental evaluations of integrated winding coupled inductors in interleaved converters," *IEEJ Journal of Industry Applications*, vol. 5, no. 3, pp. 276–288, 2016.
- [33] K. J. Hartnett, J. G. Hayes, M. G. Egan, and M. S. Rylko, "Cctt-core split-winding integrated magnetic for high-power dc-dc converters," *IEEE Transactions on Power Electronics*, vol. 28, no. 11, pp. 4970–4984, 2013.
- [34] M. Hirakawa, Y. Watanabe, M. Nagano, K. Andoh, S. Nakatomi, S. Hashino, and T. Shimizu, "High power dc/dc converter using extreme close-coupled inductors aimed for electric vehicles," in *The 2010 International Power Electronics Conference - ECCE ASIA -*, pp. 2941–2948, 2010.

- [35] P. L. Dowell, “Effects of eddy currents in transformer windings,” in *Proceedings IEE (UK)*, vol. 113, pp. 1387–1394, August 1966.
- [36] H. Kosai, Z. Turgut, and J. Scofield, “Experimental investigation of dc-bias related core losses in a boost inductor,” *IEEE Transactions on Magnetics*, vol. 49, no. 7, pp. 4168–4171, 2013.
- [37] TDK, *Ferrites and accessories ETD 49/25/16 Core and accessories*, 09/2017. Rev. 10/2018.
- [38] TDK, *Ferrites and accessories E 55/28/21 Core*, 09/2017. Rev. 10/2018.
- [39] Z. Yang, H. Suryanarayana, and F. Wang, “An improved design method for gapped inductors considering fringing effect,” in *2019 IEEE Applied Power Electronics Conference and Exposition (APEC)*, pp. 1250–1256, 2019.
- [40] A. Balakrishnan, W. Joines, and T. Wilson, “Air-gap reluctance and inductance calculations for magnetic circuits using a schwarz-christoffel transformation,” *IEEE Transactions on Power Electronics*, vol. 12, no. 4, pp. 654–663, 1997.
- [41] TDK, *Ferrites and accessories ETD 44/22/15 Core and accessories*, 09/2017. Rev. 10/2018.
- [42] A. Van den Bossche, V. Valchev, and T. Filchev, “Improved approximation for fringing permeances in gapped inductors,” in *Conference Record of the 2002 IEEE Industry Applications Conference. 37th IAS Annual Meeting (Cat. No.02CH37344)*, vol. 2, pp. 932–938 vol.2, 2002.
- [43] Wolfspeed, *C3M0045065K Silicon Carbide Power MOSFET C3M TM MOS-FET Technology*, 2020. Rev. 12-2020.
- [44] Wolfspeed, *C3D20065D Silicon Carbide Schottky Diode Z-Rec® Rectifier*, 2016. Rev B. 08-2016.
- [45] Nippon Chemi-con, *MINIATURE ALUMINUM ELECTROLYTIC CAPACITORS, KWASeries*, 2021. Rev. 2021.
- [46] Texas Instruments, *UCC21520 4-A, 6-A, 5.7-kVRMS Isolated Dual-Channel Gate Driver*, 2016. Rev. December 2021.

- [47] Recom, *2 Watt SIP7 for SiC and IGBT Applications*, 2020. Rev. 06/2020.
- [48] Texas Instruments, *TMS320F2806x Real-Time Microcontrollers*, 2010. Rev. 09/2021.
- [49] L.Dixon, *BEddy Current Losses in Transformer Windings and Circuit Wiring*. Texas Instrument Application Note.
- [50] J. Ferreira, "Improved analytical modeling of conductive losses in magnetic components," *IEEE Transactions on Power Electronics*, vol. 9, no. 1, pp. 127–131, 1994.
- [51] Omicron Lab, *Bode 100 Revision 2 Vector Network Analyzer*, 07/2017.
- [52] M. Mu and F. C. Lee, "A new core loss model for rectangular ac voltages," in *2014 IEEE Energy Conversion Congress and Exposition (ECCE)*, pp. 5214–5220, 2014.
- [53] TDK, *Ferrites and accessories SIFERRIT material N87*, 09/2017. Rev. 10/2018.
- [54] A. Villarruel-Parra, "Digital average-current control for the dual interleaved boost converter," 2015.
- [55] R. W. Erickson and D. Maksimovic, *Fundamentals of Power Electronics*. California, USA: USA: Kluwer Academic Publishers,, 2003.
- [56] Fluke, *Model 187 189 True RMS Multimeter*, 08/2000.

APPENDIX A

SUPPLEMENTARY DOCUMENTS

A.1 Input Current Ripple Equations

Input current ripple equations of a 6-phase interleaved boost converters as a function of duty cycle is given in Eq. A.1.

$$\Delta I_{in-6phase} = \begin{cases} \frac{V_o(1-6D)DT_s}{L}; & 0 \leq D \leq \frac{1}{6} \\ \frac{V_o(2-6D)(D-1/6)T_s}{L}; & \frac{1}{6} \leq D \leq \frac{2}{6} \\ \frac{V_o(3-6D)(D-2/6)T_s}{L}; & \frac{2}{6} \leq D \leq 0.5 \\ \frac{V_o(4-6D)(D-3/6)T_s}{L}; & 0.5 \leq D \leq \frac{4}{6} \\ \frac{V_o(5-6D)(D-4/6)T_s}{L}; & \frac{4}{6} \leq D \leq \frac{5}{6} \\ \frac{V_o(6-6D)(D-5/6)T_s}{L}; & \frac{5}{6} \leq D \leq 1 \end{cases} \quad (\text{A.1})$$

A.2 Controller Design

Fig. A.1 shows the PWM switch and corresponding averaged CCM model of a single switch Boost converter. The model consists of one switch and one diode and instantaneous voltages and currents of the averaged switch network are denoted as $v_1(t)$, $v_2(t)$, $i_1(t)$, and $i_2(t)$.

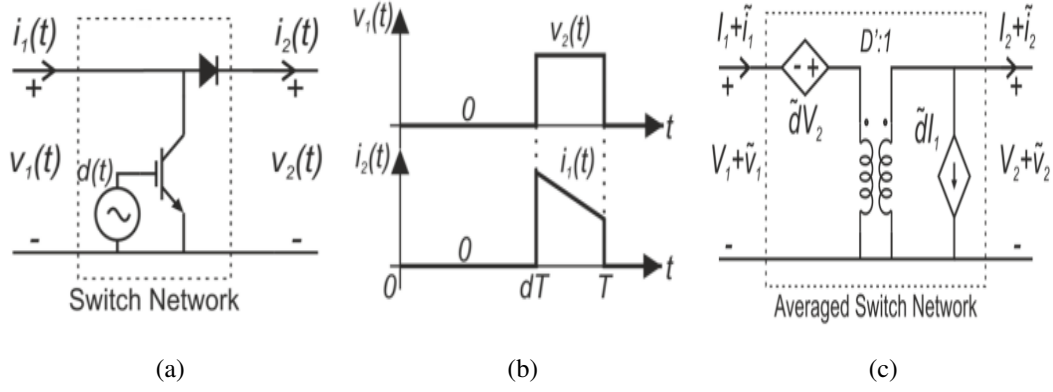


Figure A.1: (a) Single-phase boost converter switch network. (b) Switch network waveforms. (c) Equivalent dc and ac small-signal averaged switch network model. [54]

For one switching period, as a function of duty cycle, D , $v_1(t)$ and $i_2(t)$ can be written as.

$$v_1(t) = \begin{cases} 0; & 0 \leq t \leq DT_s \\ v_2(t); & DT_s \leq t \leq T_s \end{cases} \quad (\text{A.2})$$

$$i_2(t) = \begin{cases} 0; & 0 \leq t \leq DT_s \\ i_1(t); & DT_s \leq t \leq T_s \end{cases} \quad (\text{A.3})$$

Under the assumption that the switching ripples of $v_1(t)$ and $i_2(t)$ are small or at least linear functions of time and can be averaged over a switching period, T_s , yielding:

$$\begin{aligned} \langle v_1(t) \rangle_{T_s} &= (1 - d(t)) \langle v_2(t) \rangle_{T_s} \\ \langle i_2(t) \rangle_{T_s} &= (1 - d(t)) \langle i_1(t) \rangle_{T_s} \end{aligned} \quad (\text{A.4})$$

Eq. A.4 may then be perturbed and linearized about a quiescent point of operation yielding:

$$\begin{aligned} V_1 + \tilde{v}_1 &= (1 - D)(V_2 + \tilde{v}_2) - \tilde{d}V_2 - \tilde{d}v_2 \\ I_2 + \tilde{i}_2 &= (1 - D)(I_1 + \tilde{i}_1) - \tilde{d}I_1 - \tilde{d}i_1 \end{aligned} \quad (\text{A.5})$$

where the voltage and currents at the input and output ports and the duty-ratio are expressed as the sum of the quiescent value plus a small ac variation: $V_1 + \tilde{v}_1, V_2 +$

$\tilde{v}_2, I_1 + \tilde{i}_1, I_2 + \tilde{i}_2, D + \tilde{d}$. The equivalent averaged switch model of IWCI interleaved boost converter shown in Fig. 6.14, can be obtained from Eq. A.5 by neglecting the nonlinear terms $\tilde{d}v_2$ and $\tilde{d}i_1$. Two-phase interleaved boost converter with IWCI is shown in Fig. 6.14, where the transistors of each boost cell are controlled by the independent sources $d_1(t)$ and $d_2(t)$. Also additional elements are included: the series resistance of the center winding R_{in} , the series resistances of the outer windings and a small-signal current source, $iz(t)$, connected in parallel with the load resistor. $iz(t)$ is also known as a perturbation current and can be used to represent load changes in the circuit.

The input port currents of switch networks are as the perturbed local average phase currents $I_1 + \tilde{i}_1$ and $I_2 + \tilde{i}_2$. Similarly, the output currents at each network are denoted $I_{o1} + \tilde{i}_{o1}$ and $I_{o2} + \tilde{i}_{o2}$ are sum of these two current equal to the total output current, $I_{o12} + \tilde{i}_{o12}$ delivered to C_o and R_{load} . Finally, the current flowing through C_o is denoted as \tilde{i}_c and the current delivered to the load resistance as $I_o + \tilde{i}_o$. By using Eq. A.5 and Fig. 6.14, the current at the output ports of the switch networks 1 and 2 can be written as:

$$\begin{aligned} I_{o1} + \tilde{i}_{o1} &= (1 - D_1)(I_1 + \tilde{i}_1) - \tilde{d}_1 I_1 \\ I_{o2} + \tilde{i}_{o2} &= (1 - D_2)(I_2 + \tilde{i}_2) - \tilde{d}_2 I_2 \end{aligned} \quad (\text{A.6})$$

The total converter output current, can be written as:

$$I_o + \tilde{i}_o + \tilde{i}_c + \tilde{i}_z = (1 - D_1)(I_1 + \tilde{i}_1) - \tilde{d}_1 I_1 + (1 - D_2)(I_2 + \tilde{i}_2) - \tilde{d}_2 I_2 \quad (\text{A.7})$$

Eq. A.7 may be split by grouping the steady-state and the small-signal terms from both sides of the equation into two separate equations:

$$\begin{aligned} I_o &= (1 - D_1)I_1 + (1 - D_2)I_2 \\ \tilde{i}_o + \tilde{i}_c + \tilde{i}_z &= (1 - D_1)\tilde{i}_1 - \tilde{d}_1 I_1 + (1 - D_2)\tilde{i}_2 - \tilde{d}_2 I_2 \end{aligned} \quad (\text{A.8})$$

Under steady-state conditions, the duty-ratios D_1 and D_2 can be assumed identical. Furthermore as I_{in} divides equally between the IWCI phase windings, the quiescent value of the phase currents I_1 and I_2 is equal to $I_{in}/2$. Under these assumptions, Eq. A.8 can be rearranged as shown in Eq. A.9.

$$\begin{aligned} I_o &= (1 - D)I_{in} \\ c \frac{v_o}{dt} &= \tilde{i}_o + \tilde{i}_c + \tilde{i}_z = (1 - D_1)\tilde{i}_1 - \tilde{d}_1 I_1 + (1 - D_2)\tilde{i}_2 - \tilde{d}_2 I_2 \end{aligned} \quad (\text{A.9})$$

Eq. A.9 represents differential equation for converter output voltage. In order to obtain differential equations for phase currents, voltage equation for circuit loop for each phase may be written. After rearranging these voltage equations differential equations for phase currents can be written as:

$$\begin{aligned} \frac{d\tilde{i}_1}{dt} = & -\tilde{i}_1 \frac{(L_1 + 2L_{m1} + L_2)R_2 + (L_2 + L_{m2})R_{in}}{L_{tot}} - \tilde{d}_1 \frac{(L_1 + 2L_{m1} + L_2)V_o}{L_{tot}} \\ & -\tilde{i}_2 \frac{(-L_1 - 2L_{m1} + L_{m2})R_2 + (L_2 + L_{m2})R_{in}}{L_{tot}} - \tilde{d}_2 \frac{(L_2 + 2L_{m1} - 2L_{m2})V_o}{L_{tot}} \\ & -\tilde{v}_{in} \frac{L_2 + 2L_{m2}}{L_{tot}} - \tilde{v}_o \frac{(L_2 + 2L_{m2})(1 - D)}{L_{tot}} \end{aligned} \quad (\text{A.10})$$

$$\begin{aligned} \frac{d\tilde{i}_2}{dt} = & -\tilde{i}_2 \frac{(L_1 + 2L_{m1} + L_2)R_2 + (L_2 + L_{m2})R_{in}}{L_{tot}} - \tilde{d}_2 \frac{(L_1 + 2L_{m1} + L_2)V_o}{L_{tot}} \\ & -\tilde{i}_1 \frac{(-L_1 - 2L_{m1} + L_{m2})R_2 + (L_2 + L_{m2})R_{in}}{L_{tot}} - \tilde{d}_1 \frac{(L_2 + 2L_{m1} - 2L_{m2})V_o}{L_{tot}} \\ & -\tilde{v}_{in} \frac{L_2 + 2L_{m2}}{L_{tot}} - \tilde{v}_o \frac{(L_2 + 2L_{m2})(1 - D)}{L_{tot}} \end{aligned} \quad (\text{A.11})$$

where,

$$L_{tot} = (L_2 + 2L_1 + 4L_{m1} - L_{m2})(L_2 + L_{m2}) \quad (\text{A.12})$$

The elements of the state, input and output matrices are given in below.

$$a_{11} = a_{22} = -\frac{(L_1 + 2L_{m1} + L_2)R_2 + (L_2 + L_{m2})R_{in}}{L_{tot}} \quad (\text{A.13})$$

$$a_{12} = a_{21} = -\frac{(-L_1 - 2L_{m1} + L_{m2})R_2 + (L_2 + L_{m2})R_{in}}{L_{tot}} \quad (\text{A.14})$$

$$a_{13} = a_{23} = -\frac{(L_2 + L_{m2})(1 - D)}{L_{tot}} \quad (\text{A.15})$$

$$a_{31} = a_{32} = \frac{(1 - D)}{C_o} \quad a_{33} = -\frac{1}{C_o R_{load}} \quad (\text{A.16})$$

$$b_{11} = b_{22} = -\frac{(L_1 + 2L_{m1} + L_2)V_{in}}{(1 - D)L_{tot}} \quad b_{12} = b_{21} = -\frac{(L_1 + 2L_{m1} - L_{m2})V_{in}}{(1 - D)L_{tot}} \quad (\text{A.17})$$

$$b_{14} = b_{24} = -\frac{L_2 + L_{m2}}{L_{tot}} \quad b_{31} = b_{32} = -\frac{V_{in}}{2C_o(1-D)^2 R_{load}} \quad (\text{A.18})$$

$$b_{33} = -\frac{1}{C_o} \quad b_{13} = b_{23} = b_{34} = 0 \quad (\text{A.19})$$